Shock Compression of Body-Centered Cubic Metals from the Atomistic to Continuum Scale: Iron and Molybdenum

Thesis by
Vatsa Gandhi

In Partial Fulfillment of the Requirements for the
Degree of
Doctor of Philosophy

CALIFORNIA INSTITUTE OF TECHNOLOGY
Pasadena, California

2023
Defended April 24, 2023

Vatsa Gandhi
ORCID: 0000-0002-6752-113X

ACKNOWLEDGEMENTS

First, I would like to express my sincere gratitude to my advisor and my role model Prof. Guruswami Ravichandran who has been very encouraging and supportive throughout my Ph.D. Ravi has been an excellent mentor. I truly appreciate all the freedom he has given me in the lab and shaping me to be an independent researcher. Ravi has always been patient, kind, and positive, and I appreciate all our valuable research discussions. Although he has been halfway across the world this past year, he has always made himself available to discuss confusing results or give career and general advice. I am very honored to have been mentored by Ravi.

I would like to acknowledge my committee members. I would like to thank Prof. Kaushik Bhattacharya for his guidance and insightful discussions. I appreciate that he is always available to meet and willing to help me understand my experimental results. I have learned a lot from him both through our personal interactions and from his insights on mechanics during the Kaushik-Ravi group meetings. I would further like to thank Professor Michael Mello for all the fruitful discussions regarding optics and window experiments. I also enjoyed the stories from his time at Brown University and about previous students as they encouraged me to continue enjoying my research. I genuinely appreciate his shared excitement for my experiments. I would like to thank Professor Ares Rosakis for his guidance this past year with both my research and my future career.

I would not be here without the help of my dear friend Suraj Ravindran. He has been a mentor to me both in the lab and life, and it is safe to say that he has taught me everything I know about experiments. He is always available for late night discussions on research and even though he is now halfway across the country, he is still always there to comfort me when experiments don't go as planned. I will always remember our countless hours spent together in the lab preparing for and running experiments. Thank you once again for all of your guidance and support.

I would like to thank my good friends and lab-mates Barry Lawlor and Jack Weeks for their insightful research discussions and their advice on experiments. We've shared some great moments in the lab that I will never forget, including

our first successful pore-collapse and lattice plate impact experiments. I will also always remember our first conference together where despite all the flight delays/cancellations, we made the last-minute decision to drive for 8 hours just so I could make it to my presentation on time.

I would also like to thank my good friend Andrew Akerson for constantly pushing me to be the best researcher I can be. I really appreciate all of his advice and his help running experiments. I can always go to him for mechanics help and my discussions with him are worthwhile because he gets me to think critically about my experiments. I've also enjoyed our time outside of the office building new PCs and exploring LA. I would like to thank my close friend Adeline Wihardja for her support of my late-night experiments and for keeping me motivated. I'm glad we share the same hobbies and I will definitely miss the late-night boba runs. To both Andy and Adeline, I will always appreciate our friendship.

The Kaushik-Ravi group has been incredibly supportive and kept me motivated throughout the years. I would like to thank Eric Ocegueda, Aakila Rajan, Sathvik Sanagala, and Amanda Toledo Barrios for all their feedback. I also appreciate all the time we have spent outside of the office watching movies and getting food. I would also like to thank the friends I made along the way: my piano partner Shengduo Liu, my support system since 1^{st} year Padmanabha Simha, Omar Kamal, Liam Heidt, my Quals partner in crime Salvador Gomez, and my roommate Jagannadh Bodapati.

My experiments could not have been conducted without the help of Ali Kiani always machining my parts on time and with precision, Donna Mojahedi ensuring my items were always delivered on time, Brandon Niles, and Petros Arakalian. I am also sincerely grateful to the staff in both GALCIT and MCE departments: Christine Ramirez, Jamie Sei, Lynn Seymour, Jenni Campbell, and Stacie Takase.

I would also like to gratefully acknowledge the financial support of DOE/NNSA award no. DE-NA0003957.

Finally, I am most grateful to my parents Bhupesh and Sheetal, my sister Nandani, and my fiancé Mili who have supported me unconditionally throughout my journey and constantly motivated me, especially during the tough times.

ABSTRACT

Fundamental understanding of material behavior under extreme conditions is crucial for designing high strength, light weight, and high temperature resistance materials, and for modeling planetary physics problems such as behavior of the core and impact phenomena. Under extreme conditions, materials not only exhibit a different mechanical, thermal, and failure response but can also undergo structural changes, such as phase transformations, which significantly alters their material properties. This motivates studying their dynamic response and developing constitutive models for applications such as hypersonics, high speed manufacturing, impact and blast of structures, aircraft and spacecraft shielding, meteorite impact, and collision of planets. Despite the importance, experimental investigations of shock induced phase transitions, inelastic material behavior, and elastic-plastic anisotropy under multi-axial stress states and at microscopic length scales of metals still remains largely unexplored. Thus, the focus of this thesis is on the shock compression behavior of body-centered cubic (BCC) metals, specifically iron and molybdenum, under compression-shear loading and at the atomistic-continuum spatial scales. In particular, the role of solid-solid phase transformation of body-centered cubic (BCC) iron on material strength and the orientation dependence of single crystal molybdenum on its elastic-plastic transition is investigated.

Iron in its high pressure hexagonal close-packed (HCP) ϵ-phase is critical in geological and planetary applications such as inner cores of rocky planets and hypervelocity impacts of asteroids, and meteorites. Thus, understanding plasticity behavior of iron under these condensed matter states is important to develop more accurate models for such applications and to understand deformation mechanisms of inner planetary cores. Because the ϵ-phase is unstable, iron reverts to its ambient α-phase (BCC) upon release making it difficult to probe the strength behavior using conventional methods. Additionally, solid-solid phase transformations provide a unique opportunity to study material strength as they are crucial for expanding the design space for various load-bearing applications. In the first part of the thesis, the pressure dependent dynamic strength behavior of both the ambient BCC α-phase and high-pressure HCP ϵ-phase of iron at strain rates on the order of 1×10^5 s^{-1} and pressures up to 42 GPa is investigated. Pressure shear plate impact experiments are

conducted using a sandwich configuration to decouple the effect of pressure and shear thereby allowing to probe shear strength once the sample reaches an equilibrated state of pressure but prior to release. The strength of the ϵ-phase is observed to be more than double the strength of α-phase possibly due to microstructural evolution during phase transformation. Additionally, the evolution of yield properties with pressure, temperature, and strain is presented for the first time, enabling more accurate modeling of extreme deformation phenomena associated with iron-rich celestial bodies such as planetary collisions.

Molybdenum, its alloys, and other body-centered cubic (BCC) refractory metals are critical in geological and planetary applications such as structural properties of terrestrial planetary composition, formation of the earth-moon system, and hypervelocity impacts of rocky planets. Additionally, the high temperature specific strength, creep resistance, and ductility of BCC refractory metals make them ideal for aerospace and armor/anti-armor applications. Under high strain-rate inelastic loadings, the macroscopic response of these metals is often influenced by the atomistic mechanisms including dislocation motion and deformation twinning. Current material models rely on investigations that involve continuum measurements followed by postmortem microstructural analysis of recovered samples. However, these may not reflect the material behavior during the passage of the shock wave and, thus, requires real-time in-situ atomistic characterization to link the microstructure to macroscopic response. In the second part of the thesis, plate impact experiments coupled with both laser interferometry continuum measurements and *in-situ* dynamic Laue x-ray diffraction (XRD), at the Advanced Photon Source (APS), are conducted on single crystal molybdenum. Here, the role of crystal orientation, either $[1\,0\,0]$ or $[1\,1\,1]$, on deformation mechanisms during the elastic-plastic transition and the steady state response is explored at pressures ranging from $9 - 19$ GPa. Complementary simulation methodology is developed to analyze the evolution of the Laue diffraction spots captured during impact. By extracting the lattice strain and stresses from XRD images, dislocation slip along $\{1\,1\,0\}\langle 1\,1\,1\rangle$ and $\{1\,1\,2\}\langle 1\,1\,1\rangle$ is found to be the probable deformation mechanism during compression with negligible anisotropy observed at the Hugoniot state. For the first time, real-time evidence of molybdenum undergoing deformation twinning along $\{1\,1\,\overline{2}\}\langle 1\,1\,1\rangle$ during shock release beyond a critical pressure of 16 GPa irrespective of the loading orientation is presented.

PUBLISHED CONTENT AND CONTRIBUTIONS

[1] V. Gandhi, S. Ravindran, A. Joshi, and G. Ravichandran, "Real-time characterization of dislocation slip and twinning of shock compressed molybdenum single crystals," (Under Review) (2023),
V.G. performed the experiments, prepared the experimental data, developed the simulation methodology, and wrote the manuscript.

[2] V. Gandhi, S. Ravindran, and G. Ravichandran, "Dynamic strength of iron at high pressures and strain rates," Physical Review Letters **128**, 015705 (2022),
V.G. performed the experiments, prepared the experimental data, performed the numerical simulations, and wrote the manuscript.

CONTENTS

Acknowledgements . . . iii
Abstract . . . v
Published Content and Contributions . . . vii
Contents . . . vii
List of Figures . . . ix
List of Tables . . . xiii
Chapter I: Introduction . . . 1
1.1 Motivation . . . 1
1.2 Shock compression theory . . . 2
1.3 Shock compression of BCC metals . . . 5
1.4 Experimental methods for characterizing dynamic behavior of materials . . . 8
1.5 Scope of the thesis . . . 14
Chapter II: Dynamic Strength and Plasticity of Iron . . . 21
2.1 Introduction . . . 21
2.2 Materials and methods . . . 23
2.3 Experimental results . . . 28
2.4 Simulation methodology . . . 31
2.5 Discussion . . . 44
2.6 Conclusion . . . 49
Chapter III: Real-Time Characterization of Dislocation Slip and Twinning of Shock Compressed Molybdenum Single Crystals . . . 54
3.1 Introduction . . . 54
3.2 Experimental methods . . . 56
3.3 Simulation . . . 60
3.4 Results and discussions . . . 77
3.5 Conclusion . . . 82
Chapter IV: Conclusions . . . 87
4.1 Summary . . . 87
4.2 Future work . . . 88

LIST OF FIGURES

Number *Page*

1.1 Overview of the applications, experimental facilities, and measurement techniques for full spatio-temporal characterization of materials. 3

1.2 Schematic of a propagating shock wave. (a) Illustration of the state variables ahead (+) and behind (−) the propagating shock wave and (b) stress–specific volume Hugoniot where $V = 1/\rho$. Note $V/V_0 = 1 - \epsilon$ where ϵ is the uniaxial strain. 4

1.3 A schematic of the split-Hopkinson (Kolsky) pressure bar experimental setup. The overall setup can be modified to test alternative loading conditions such as tensile and/or torsional behavior. 8

1.4 Schematic of the experimental configuration for (a) Z pulsed power facility and (b) laser ablation. Additionally, a typical profile of the time varying current and laser power is illustrated for the Z pinch and laser ablation setups, respectively. 9

1.5 Experimental schematic for (a) normal and (b) pressure-shear plate impact (PSPI) experimental configurations. Note the projectile's direction of travel is indicated by the vector V_0 but the normal of the projectile in the PSPI configuration is along u_0. . 11

2.1 Experimental configuration used to characterize the dynamic strength of iron. (a) Schematic of the pressure shear plate impact setup in sandwich configuration. (b) Distance-time ($x - t$) diagram for tungsten carbide-iron sandwich assuming elastic wave propagation. 24

2.2 Microstructure of Armco Iron obtained using (a) optical microscope (OM) and (b) scanning electron microscope (SEM). . . . 25

2.3 Surface roughness of iron probed along a line from AFM data. The average roughness across the entire area was measured to be $Rq = 150$ nm. 26

2.4 Experimental (a) normal and (b) transverse free surface velocities. The profiles are shifted in time for visual purposes. 29

2.5 Transverse velocity from the sensitivity study for 15.8 GPa experiment for varying (a) Y_0, (b) B, (c) n, and (d) m. The shading within the experimental curve corresponds to the 5% uncertainty envelope. 39
2.6 Transverse velocity from the sensitivity study for 21.5 GPa experiment for varying (a) Y_0, (b) B, (c) n, and (d) m. The shading within the experimental curve corresponds to the 5% uncertainty envelope. 40
2.7 Transverse velocity from the sensitivity study for 30.2 GPa experiment for varying (a) Y_0, (b) B, (c) n, and (d) m. The shading within the experimental curve corresponds to the 5% uncertainty envelope. 41
2.8 Transverse velocity from the sensitivity study for 42 GPa experiment for varying (a) Y_0, (b) B, (c) n, and (d) m. The shading within the experimental curve corresponds to the 5% uncertainty envelope. 42
2.9 Comparison of peak transverse velocities and their sensitivities to (a) Y_0, (b) B, (c) n, and (d) m. The error bars on the experimental data corresponds to the 5% uncertainty envelope. . . . 43
2.10 Final experimental and simulated peak transverse velocities plotted against pressure. The error bars correspond to the 5% uncertainty envelope. 44
2.11 Plot of (a) normal and (b) transverse free surface velocity profiles at varying pressures for pure iron. The solid lines correspond to experimental records and the dashed curves correspond to simulated profiles. Both the normal and transverse velocity profiles (except for the 15 GPa curves) have been shifted for clarity in visualizing the results. 45

2.12 Plots of (a) shear stress vs shear strain of ϵ-iron for varying pressures and (b) comparison of von Mises yield strength at 10% shear strain with data from literature. The best fit curve (black dashed line) follows a power law relation ($Y \propto P^{0.35}$) compared to the linear relation obtained from static experiments by Gleason and Mao [8]. The main plot compares our data with other static experiments and the inset contains data from other dynamic experimental studies alongside our best fit curve. The dashed red curve corresponds to the theoretical yield strength ($G/2\pi$) obtained from shear modulus data from [8]. 47

3.1 Experimental configuration at the Dynamic Compression Sector. (a) Schematic of the front surface plate impact and reflection geometry XRD configuration and (b) distance-time ($x-t$) diagram indicating the designed XRD frame capture times. Here, time $t = 0$ corresponds to the impact time and the first XRD frame, not illustrated, is designed to be obtained prior to impact at $t = -100$ ns. 58

3.2 X-ray spectral scan for the 24-Bunch mode for various runs at APS. 59

3.3 Definition of the global ($\boldsymbol{x}_i$) and sample coordinates ($\hat{\boldsymbol{x}}_i$) 61

3.4 Geometry of the detector screen. 61

3.5 Range of diffraction angles. 62

3.6 Silicon calibration for Shot 21–05–56 used to determine the geometrical detector parameters for the experiment. (a) Azimuthally integrated silicon pattern and (b) overlay of the simulated pattern on the experimental data. Here, the obtained parameters were as follows: *Detector Distance:* 101.70 mm, *Detector Center:* (998 px, 1053 px), *Beam Center:* (1884 px, 1020 px). 63

3.7 Atoms arranged within the single crystal sample. 64

3.8 Misorientation of the atomic orientation to the sample axis. . . 65

3.9 The centroid of the diffraction spots along the (a) x-pixel direction and (b) the y-pixel direction are determined using the Lorentzian function fits. (c) These centers are plotted on a representative XRD image from an experiment. 71

3.10 Inverse mapping of the unit diffracted wave vectors from the detector images used for the optimization procedure for determining the deformation gradient. 72
3.11 Simulated diffraction spots for the 9-spot case. 73
3.12 Simulated diffraction spots for the 6-spot case. 74
3.13 Simulated diffraction spots for the 3-spot case. 75
3.14 Corrected particle velocity measurements conducted using photonic Doppler velocimetry (PDV) for molybdenum (Mo) along (a) [1 0 0] and (b) [1 1 1] orientations. 78
3.15 Summary of experimental results. (a)-(d) Experimentally obtained XRD frames which show both spots shifting due to compression and deformation twinning at higher pressure during the unloading. The diffraction spots are labeled using (e)-(h) for the respective XRD simulations incorporating both compression and twinning behavior. (i)-(j) The interferometry data is also shown indicating the time instances of XRD frame captures. 79
3.16 Resolved shear stress (τ_{rss}) along the 12 different $\{1\,1\,0\}\langle 1\,1\,1\rangle$ and $\{1\,1\,2\}\langle 1\,1\,1\rangle$ slip systems of BCC single crystal for orientations, [1 0 0] and [1 1 1] molybdenum crystals at pressures ranging from $10-20$ GPa. Only the data above the critical resolved shear stresses (dashed lines) are shown. 80

LIST OF TABLES

Number *Page*

2.1 Composition of Armco iron [25] 25
2.2 Material properties 28
2.3 Dimensions of flyer, anvils, and sample 29
2.4 Summary of performed experiments. 29
2.5 Parameters for the free energy of the two different phases (α, ϵ) of iron. 35
3.1 Material properties of single crystal molybdenum [32] 57
3.2 Details of the x-ray diffraction experimental configuration. . . . 59
3.3 Summary of the validation tests for the optimization scheme. . 72
3.4 Summary of experimental results for Mo single crystals using both continuum and XRD analysis. 77

Chapter 1

INTRODUCTION

1.1 Motivation

Characterizing the dynamic behavior of materials, specifically dynamic strength, damage, failure processes, and the fundamental mechanisms governing high-rate plasticity, is critical for developing and designing new materials for impact-based applications. Specifically, the incentive to study dynamic material behavior is important for but not limited to applications including automobiles [1], armor and anti-armor [2, 3], aircraft and spacecraft shielding [4, 5], and hyper-velocity impacts of micrometeorites and planets [6]. In these applications, materials undergo extreme loading conditions involving high pressures, high temperatures, large strains, and high strain rate deformation thereby requiring complete characterization of their mechanics and thermodynamics prior to their usage. While the macroscopic or continuum material response is observed in practice, this problem is highly coupled with the microstructure and atomistic behavior such as role of dislocations, stacking faults, and twinning thus demanding a complete spatio-temporal characterization as illustrated in Figure 1.1.

Due to their high strain rate sensitivity and their superior ambient properties such as high hardness, body-centered cubic (BCC) metals and their alloys are of importance in applications involving dynamic loading such as impact and blast [7, 8]. A fundamental example is iron—one of the most technologically important and abundant elements. When alloyed with carbon and other metals such as manganese and nickel, one forms different variants of steel which is the most commonly used structural metal for a variety of applications. Iron in its ambient α-phase has the BCC crystal structure but undergoes both temperature-induced and pressure-induced solid-to-solid phase transitions changing its crystal structure but drastically altering its material properties which is critical for expanding the material design space. For example, steel is often heated to high temperatures and rapidly quenched to increase the hardness of the material [9]. Additionally, transformation-induced plastic (TRIP) steels, which transform from austinite to martensite phase upon de-

formation, exploit their thermodynamically unstable composition to leverage the high ductility austinite and the high strength from the martensite [10]. On a more geological and planetary applications point of view, iron, in its various phases, forms the inner core of rocky planets, such as earth, and is abundant in meteorites motivating not only studying its dynamic response and phase transitions, but also its equation of state (EOS) at these high condensed matter states [11, 12].

In addition to iron, a subclass of BCC metals are the refractory metals which include tantalum (Ta), molybdenum (Mo), and tungsten (W). Due to their ability to retain strength at high temperatures, that exceeds the capabilities of steel, these metals are important for a wide range of applications involving high operating temperatures including aerospace, chemical, and electronic industries [13]. Specifically, molybdenum and its alloys are advantageous compared to other refractory metals due to its availability as high purity crystals, high temperature specific strength, and oxidization resistance [13]. For this reason, molybdenum has been crucial for spacecraft propulsion systems, and even applications for heat sinks in electronics, furnace fixtures for heat-treating applications, and advanced circuitry [14, 15].

As discussed above, the applications of BCC metals in dynamic conditions is of high importance and many scientific studies have probed important characteristics such as dynamic strength, EOS, role of phase transition on dynamic properties, and etc., and is discussed next.

1.2 Shock compression theory

Prior to discussing the dynamic behavior of various BCC crystals, an overview of shock-induced phase transition and longitudinal shock waves traveling in solid material is presented in a Lagrangian framework. A shock is defined as a propagating discontinuity, traveling at the shock speed U_s, resulting in an abrupt and irreversible change in state variables such as normal stress σ, temperature T, density ρ, and particle velocity u_p. The state variables on either side of the wave can be related using the conservation laws and are known as the Rankine-Hugoniot jump conditions. These relations are as follows:

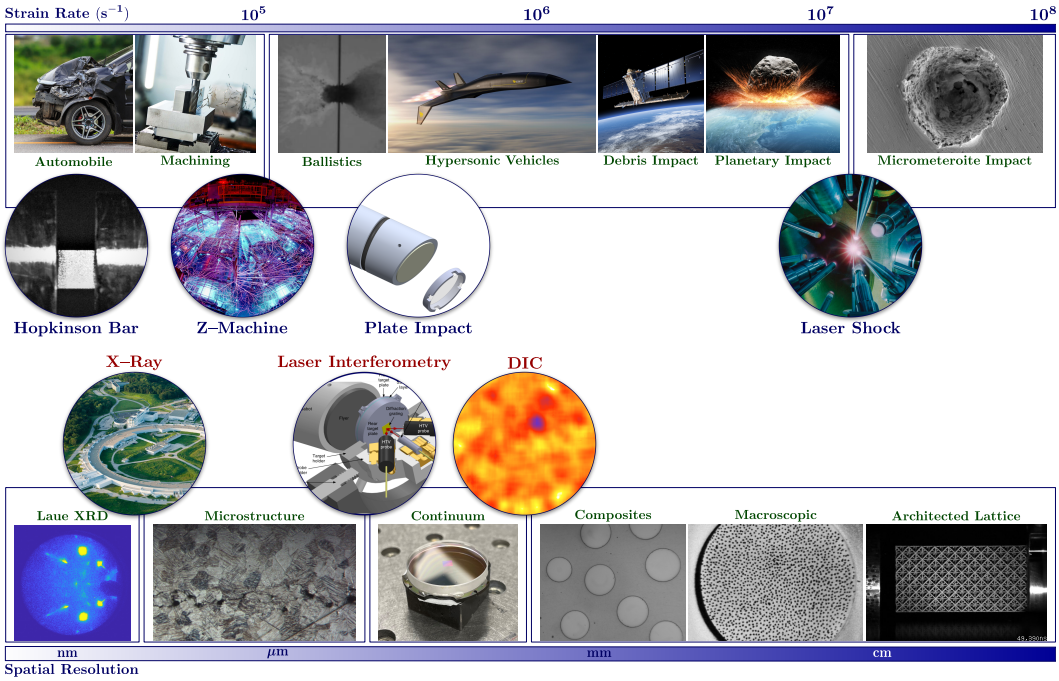

Figure 1.1: Overview of the applications, experimental facilities, and measurement techniques for full spatio-temporal characterization of materials.

$$\text{Mass:} \qquad \rho_0 U_s \left(\frac{1}{\rho^+} - \frac{1}{\rho^-} \right) = \left(u_p^- - u_p^+ \right) \tag{1.1}$$

$$\text{Momentum:} \qquad \rho_0 U_s \left(u_p^- - u_p^+ \right) = \left(\sigma^- - \sigma^+ \right) \tag{1.2}$$

$$\text{Energy:} \qquad \rho_0 U_s \left(\left(E + \frac{1}{2} u_p^2 \right)^- - \left(E + \frac{1}{2} u_p^2 \right)^+ \right) = \left((\sigma u_p)^- - (\sigma u_p)^+ \right). \tag{1.3}$$

In addition to the conservation laws, the constitutive relation known as the equation of state (EOS) of a material is required. Typically, this is expressed as a relationship between the shock and particle velocity and termed the Mie-Grüneisen EOS. For most metals a linear relation accurately represents the equation of state and is of the form

$$U_s = C_0 + S \left(u_p - u_p^{HEL} \right). \tag{1.4}$$

Here, u_p^{HEL} is the particle velocity of the material at its Hugoniot elastic limit (HEL), the elastic limit of a material under uniaxial strain conditions. Additionally, $C_0 = \sqrt{\frac{K}{\rho_0}}$ is the bulk wave speed of the material with K representing the bulk modulus, and S is the experimentally determined linear slope that typically ranges from $1 - 2$ for most materials [8].

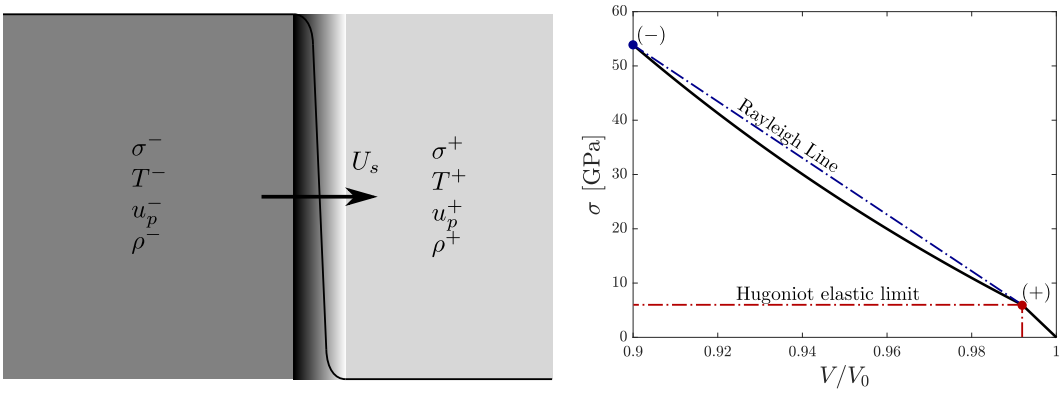

(a) (b)

Figure 1.2: Schematic of a propagating shock wave. (a) Illustration of the state variables ahead (+) and behind (−) the propagating shock wave and (b) stress–specific volume Hugoniot where $V = 1/\rho$. Note $V/V_0 = 1 - \epsilon$ where ϵ is the uniaxial strain.

Assuming that the state ahead of the shock is known, there are a total of 5 unknowns in this system of equations: σ^-, E^-, ρ^-, u_p^-, and U_s, but only 4 equations (Eqs. 1.1, 1.2, 1.3, 1.4). To close the system of equations, a variable must be determined experimentally. Generally, the particle velocity or the free surface velocity ($u_{fs} = 2u_p$) is measured using laser interferometry techniques. The locus of all achievable states behind the shock wave plotted in a two variable space is regarded as a shock Hugoniot. It is important to mention that the material does not traverse the Hugoniot but rather jump from one state to the next across the Rayleigh line. An example of the $\sigma - \rho$ Hugoniot is depicted in Figure 1.2b.

In certain scenarios during shock compression, the primary plastic wave decomposes into two different waves where the first wave is the plastic wave and the second wave corresponds to a propagating phase boundary that initiates a solid-solid phase transformation in the material. The most fundamental example of this is iron which undergoes a martensitic phase transition at 13 GPa of pressure from its ambient BCC α-phase to its high pressure HCP ϵ-phase [16]. Since the time duration of shock compression is on the order of only a few microseconds, these phase transformations are typically diffusionless. The initiation and nucleation of the phase boundary is governed by thermodynamics and kinetics while the stability is governed by external variables such as pressure p and temperature T through the Gibbs free energy [8].

$$G = G(p,T), \qquad dG = \underbrace{\left(\frac{\partial G}{\partial p}\right)_T}_{V} dp + \underbrace{\left(\frac{\partial G}{\partial T}\right)_p}_{-S} dT \tag{1.5}$$

where G is the Gibbs free energy, V is the specific volume, and S is the entropy.

Phase transformations can be classified as either first order where $\partial G/\partial P$ is discontinuous at the transformation pressure or second order where $\partial^2 G/\partial P^2$ is discontinuous. For the first order transition, since $V = \partial G/\partial P$, there is an associated volume change due to the transformation [8] such as for iron which undergoes a 6.5% volume collapse during its transition from ambient BCC phase to its high pressure HCP phase [16, 17].

With the fundamentals established, the shock compression behavior of key BCC metals is discussed in detail.

1.3 Shock compression of BCC metals

1.3.1 Iron

Studies on iron (Fe) have primarily revolved on the body-centered cubic (BCC) to hexagonal closed-pack (HCP) phase transformation at 13 GPa of pressure, discovered by Bancroft et al. [16], as it serves as a representative material to understanding shock-induced phase transformations. The classic paper by Barker and Hollenbach [17] explored the phase transformation in great detail including determining the shock Hugoniot during the forward and reverse phase transformation and its hysteresis, elastic release wave speeds, and phase transition times at various normal stresses. When the phase transformation was first discovered, Bancroft et al. [16] assumed iron had transformed from its BCC phase to its γ-phase, similar to the high temperature phase, which has a face-centered cubic crystal structure. However, it wasn't until a few years later when Jamieson et al. [18] conducted XRD measurements on quasi-statically compressed iron in a diamond anvil cell (DAC) to report the transition was actually to the ϵ-phase with an HCP crystal structure. Since then, numerous works have focused on the extreme high pressure behavior of ϵ-iron in addition to understanding the shock regime near the initiation pressure and characterize the transformation kinetics. For example, Jensen et al. [19] conducted plate impact experiments (described in the next section) on polycrystalline and single crystal iron oriented along the [1 0 0] direction. They observed the

initiation pressures to be higher for single crystals than for polycrystalline samples suggesting that shear stresses from the isotropically oriented grains may have contributed to this observation. The role of shear on the phase transformation has been an open-ended topic of research and still not has been fully understood to this date. Caspersen et al. [20] and Lew et al. [21] conducted extensive DFT calculations to understand the role of shear on the initiation of the phase boundary claiming even a modest amount of shear is sufficient to reduce the transformation pressure. However, experimentally characterizing the kinetics of this transformation and characterizing the mechanical properties of ϵ-iron is extremely difficult and is still a topic of active research.

1.3.2 Molybdenum

Molybdenum (Mo) has been studied to high pressures both quasi-statically and dynamically mostly to understand EOS, sound velocities [22], and spall strength [23]. One of the most extensive studies is the work on Mo single crystals at moderate pressures by Mandal et al. [24, 25]. The authors explored crystal orientation dependence, time dependence, and propagation distance on the elastic precursor wave prior to the shock arrival time. They showed the crystal oriented along [1 1 1] direction exhibited a much larger elastic wave amplitude compared to the [1 0 0] and [1 1 0] orientations and a decay in the elastic precursor was observed as a function of time similar to BCC iron [17] and tantalum [26]. In addition, the authors conducted crystal plasticity simulations to understand the role of micro mechanisms on the observed macroscopic behavior. Unfortunately, experimental determination of this atomistic deformation is required to better explain the wave profiles and calibrate their models. Oniyama et al. [27] explored the orientation dependence to much higher stresses ($\sim$ 100 GPa) validating the increased elastic limit of the [1 1 1] orientation. Additionally, the authors showed the elastic precursor amplitude scaled with impact stress but simultaneously observed the $U_s - u_p$ shock EOS was almost the same across the three orientations [28]. This indicates only the elastic limit is affected by the anisotropy but not the plastic shock Hugoniot (steady state) behavior.

1.3.3 Tantalum

Tantalum has gained significant interest recently as a representative material to characterize the strength of metals to extreme pressures, temperatures, and strain rate regimes and across various loading conditions [29, 30]. Ramp compression experiments, which probe the isentropic behavior of the material, by Brown et al. [31], explored the role of material processing on the observed shear strength of the material up to 250 GPa of pressure using wave profile analysis. The authors showed that work hardened samples were capable of supporting 30% more shear stress than annealed material. At much higher strain rates (10^7 s^{-1}) and pressures, Prime et al. [32] concluded the role of pressure was more significant on the observed strength of the material. The fundamental reason for this was speculated to be the role of the pressure dependent shear modulus and its scaling on the work required to move dislocations generated from the propagating shock wave [33] in addition to analysis on the role of twinning, and phase transformation.

1.3.4 Tungsten

Several studies have been conducted to characterize the shock compression behavior of tungsten. Hixon and Fritz [34] have explored the high pressure EOS models and isotherms of high purity polycrystalline tungsten. They tabulated the $U_s - u_p$ data for the shock Hugoniot of tungsten to 680 GPa in addition to developing an EOS model that mapped the hugoniot to isotherms. Based on their results, the authors note that no phase transformation (both solid or melt curve) was observed to these pressures based on the Hugoniot on contrary to previous studies that probed wave velocities to determine possible phase transitions. At much lower pressures, work by Dandekar [35] and Asay et. al [36] explored the shear strength of tungsten under shock compression. They observed the material experiences a loss in strength and attributed the softening potentially to the formation, multiplication, and motion of dislocations after the passage of the shock wave. However, real-time atomistic experiments (XRD) need to be conducted to accurately determine the microscopic deformation mechanisms responsible for this behavior.

1.4 Experimental methods for characterizing dynamic behavior of materials

Having established the importance of material characterization in the dynamic regime and the fundamental studies undertaken to characterize the high pressure and strain rate behavior of representative BCC metals, an overview on the common experimental techniques is presented.

1.4.1 Split-Hopkinson (Kolsky) pressure bar

When characterizing the dynamic behavior of materials, the most common experimental technique is the split-Hopkinson pressure bar (SHPB), also known as the Kolsky bar, due to its simplicity and high throughput. Here, the sample of interest is sandwiched between two long slender bars, the incident and the transmitted. A striker impacts the incident bar generating an elastic stress wave that travels down the bar towards the sample. Once the wave reaches the sample-bar interface, it partially reflects back to the incident bar and partly transmits into the transmitted bar. These reflected, transmitted, and incident pulses are recorded using strain gages from which the stress-strain behavior of the sample is derived [8, 37]. A schematic of the experimental setup is depicted in Figure 1.3.

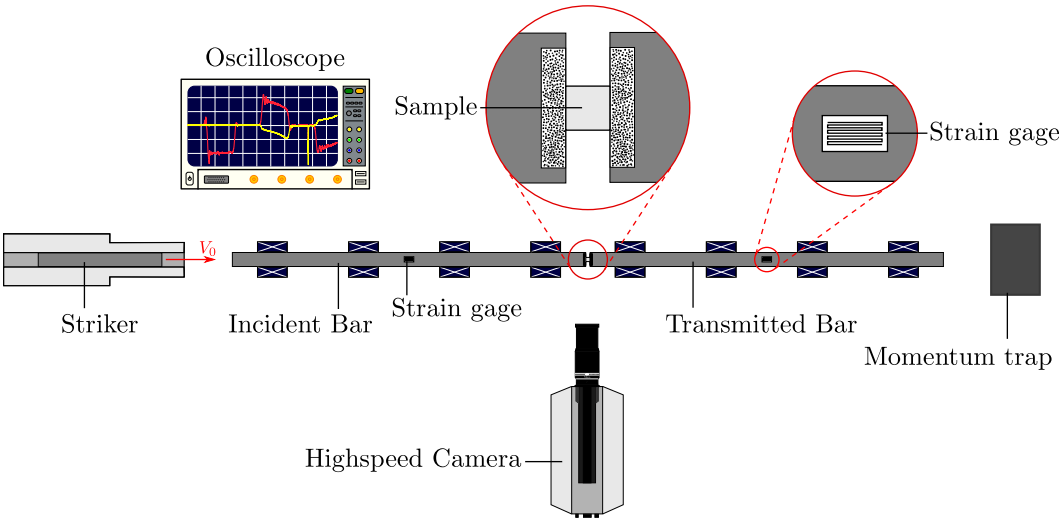

Figure 1.3: A schematic of the split-Hopkinson (Kolsky) pressure bar experimental setup. The overall setup can be modified to test alternative loading conditions such as tensile and/or torsional behavior.

In Hopkinson experiments, the material is under a uniaxial stress state where

the achievable strain rates range from $10^2 - 10^4$ s^{-1} depending on the length of the sample or impactor velocity. Additionally, since the setup requires elastic wave propagation in the incident and transmitted bars, the achievable pressures in the sample are limited to < 1 GPa [37]. Thus, one turns to alternate experimental techniques for characterizing the high pressure and high strain rate behavior of materials. While Figure 1.3 illustrates a compression split-Hopkinson bar, much research has also been conducted to understand tensile behavior [38], torsional behavior [39], dynamic fracture toughness [40], deformation mechanisms of architected meta-materials [41], and shear compression [42] using the Kolsky bar. These require modification of the setup and also an alternative to strain gages to characterize the forces and displacements in the sample such as digital image correlation (DIC) and load cells.

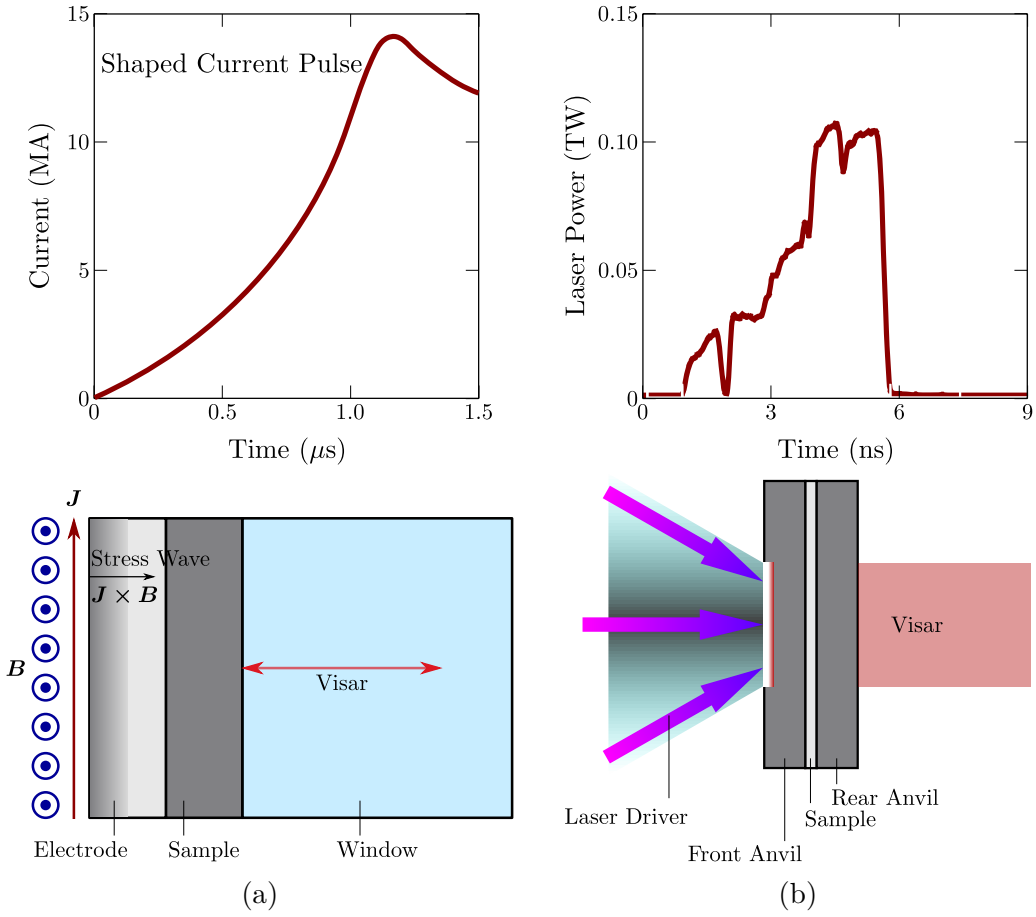

Figure 1.4: Schematic of the experimental configuration for (a) Z pulsed power facility and (b) laser ablation. Additionally, a typical profile of the time varying current and laser power is illustrated for the Z pinch and laser ablation setups, respectively.

1.4.2 Z-machine

The Z pulsed power facility at Sandia National Laboratories is important for characterizing isentropic compression of materials at high pressure (up to TPa), high strain rates, and condensed matter states [31]. In the Z-machine, a time varying current passes through a circuit generating a magnetic field in the gap between the anode and cathode as shown in Figure 1.4a. The current and magnetic field generate a Lorentz force perpendicular to the electrode and drive a stress wave to ramp compress the sample [31]. Here, laser interferometry via velocity interferometer system for any reflector (VISAR) [43] is used to measure the free surface or particle velocity in the sample to characterize its high pressure behavior. These experiments are important to decouple effects of pressure and strain rate on the strength behavior of materials [33] since strain rates are limited to approximately 10^5 s^{-1}.

1.4.3 Laser shock

Laser shock compression has gained significant interest for characterizing material behavior at extreme pressures (GPa – TPa) and strain rates ($10^5 - 10^9$ s^{-1}). In a laser ablation experiment illustrated in Figure 1.4b, an ablator is heated using lasers which expands and ejects plasma away from the target. Through conservation of momentum, this generates a loading wave, where the magnitude is proportional to the intensity of the laser [44], that propagates into the sample and a VISAR probe is used to conduct free surface velocity measurements. Both shock or isentropic compression can be imparted by varying the rise time and shape of the laser power shown in Figure 1.4b. Due to the capability of reaching extreme conditions, these experiments are critical for characterizing material behavior under planetary core conditions and understanding phenomena such as EOS melt lines [45, 46], hyper velocity planetary impacts, and material strength using hydrodynamic instabilities [6, 44].

1.4.4 Normal and pressure-shear plate impact experiments

Plate impact experiments are a conventional and robust method to generate shock compression in materials and probe their high pressure and high strain-rate behavior. Here, a flyer plate is accelerated to velocities ranging from $0.1 - 7$ km/s and impacts a stationary target generating shock waves propagating in the flyer-target assembly. Unlike the Hopkinson bar experiment, the

material is under a state of uniaxial strain and the material behavior can be probed to pressures up to 700 GPa, and strain rates ranging from $10^5 - 10^7$ s^{-1}. For a normal plate impact experiment, the flyer normal is aligned to the travel direction of the projectile, whereas, in a pressure-shear plate impact (PSPI) experiment [47], the flyer normal is angled. This implies that in a PSPI experiment, the impact not only generates compressive waves in the materials but also transverse shear waves. A schematic of the two experimental setups is depicted in Figure 1.5.

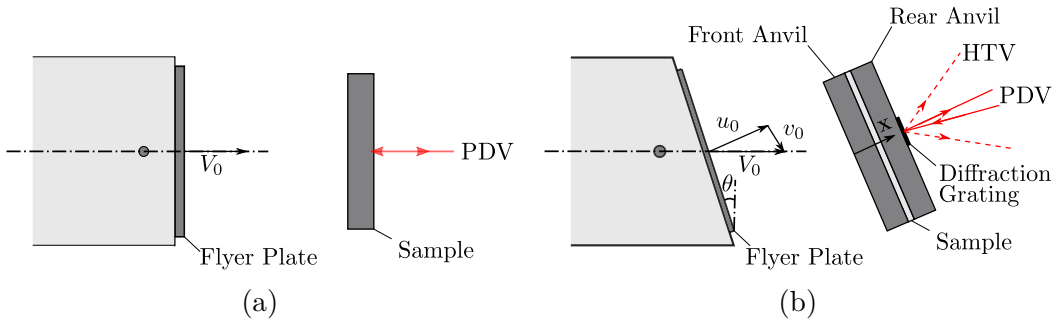

Figure 1.5: Experimental schematic for (a) normal and (b) pressure-shear plate impact (PSPI) experimental configurations. Note the projectile's direction of travel is indicated by the vector V_0 but the normal of the projectile in the PSPI configuration is along u_0.

As mentioned earlier, a normal impact generates longitudinal waves in the material upon impact but simultaneously, a boundary wave traveling at the elastic longitudinal wave speed is generated at the circular boundary of the sample due to the traction free conditions. This means the sample remains inertially confined only prior to the arrival of the boundary wave. For this reason, typically, the free surface velocities are measured at the center of the sample using laser interferometry such VISAR [43] or photonic Doppler velocimetry (PDV) [48] where the material is under uniaxial strain conditions the longest. The idea is to interfere reflected light from the sample free surface with a delayed version of itself (velocity interferometer such as VISAR) or a reference laser (displacement interferometer such as PDV) and phase difference of these superposed beams is proportional to the normal velocity. Similarly, for transverse velocity in a PSPI experiment, when the incident beam encounters the diffraction grating, the beam splits into a 0^{th} (the normal) and $\pm 1^{st}$ order beams where the latter ($\pm 1^{st}$) are interfered with each other to determine the transverse motion. The expressions relating normal ($u(t)$) and transverse

$(v(t))$ velocity to the frequencies $(f(t))$ associated with the phase difference are

$$u(t) = \frac{\lambda}{2}\left(f(t) - f_c\right) \tag{1.6}$$

$$v(t) = \frac{d}{2}\left(f(t) - f_c\right) \tag{1.7}$$

where, f_c is the carrier frequency, λ is the wavelength of light, and d is the grating pitch. More information on the transverse interferometry will be discussed later.

The measured free surface velocities can be used to extract fundamental material behavior such as characterizing the equation of state of the material ($U_s - u_p$ [27], phase transformations [16]), strength [49], spall strengths of materials [50, 51], and even pressure-dependent wave speeds [52]. The last application relies on holding the state of stress constant which can be done by placing a transparent window behind the target and probing the interface, known as window interferometry [53].

While laser interferometry are point-wise continuum-scale measurements, this restricts measurements to characterize only homogeneous materials. Thus, new advancements in velocity measurements have been developed to improve the spatial resolution such as line-ORVIS [54] which uses streak cameras and recently, 3D digital image correlation [55] using two high speed cameras. This enables characterizing the mesoscale–macroscale behavior of homogeneous, heterogeneous, and even architected materials.

It is understood that the macroscopic response of materials is strongly coupled with its micromechanical behavior. However, as described here, the plate impact experiments primarily probe the continuum scale response and typically, molecular dynamic (MD) simulations are performed to explain the observed macroscopic behavior. Thus, recent developments at the Dynamic Compression Sector (DCS) [56] at the Advanced Photon Source (APS) utilize *in-situ* x-rays to probe the fundamental deformation behavior under shock compression. This has enabled real-time characterization of evolution of lattice dynamics during phase transformation [57–59] and characterizing the atomistic deformation mechanisms during elastic-plastic compression. Here, during plate impact, polychromatic x-ray bunches, with 153.4 ns interspacing, are directed

towards the sample angled at some θ_g and the diffracted patterns are collected on a scintillation screen which converts x-rays to visible light. These x-ray measurements can be triggered to probe important features such as phase transformation, shock compression, and even shock release during an impact event. At DCS, two different configurations can be employed where the incident x-ray bunch is allowed to fully penetrate through a very thin sample ($\mathcal{O}(\mu\text{m})$) known as transmission geometry and reflection geometry where the incident x-rays are reflected off a surface of the sample prior to being collected on a detector. From the shift, mosaic spread, and the appearance or disappearance of diffraction rings for polycrystalline sample or diffraction spots for a single crystal sample, the lattice strains, and information on crystalline phases can be determined.

As discussed above, normal plate impact experiments are advantageous to study the shock compression behavior of materials. However, their main disadvantage is the material behavior is not probed under a multiaxial state of stress limiting characterizing the pressure dependent strength of materials and even shear-induced phase transformation behavior. For this reason, PSPI experiments are critical. While there are various different configurations of PSPI experiments to probe material strength [60], the focus of this thesis is on the sandwich configuration depicted in Figure 1.5b used to probe material strength at a constant pressure [61]. Here, the material of interest is sandwiched between two high impedance, high strength anvils such that after impact, the faster longitudinal wave arrives at the anvil-sample interface first compressing it to an equilibrated state of pressure through a series of reverberations. The slower transverse wave arrives at a later time to shear the sample at a constant pressure to probe its stress vs. strain behavior. Due to the transverse motion, both normal and transverse free surface velocity measurements are conducted at the rear free surface using PDV and heterodyne transverse velocimetry (HTV) [62], respectively. Additional details regarding the experimental methodology will be discussed in Chapter 2. Overall, this is a convenient setup for probing strength of materials such as iron where a constant state of stress is required in the material to prevent reverse phase transformation during the shearing window.

Conventionally, the anvils are chosen such that they remain elastic during the experiment [60, 61]. For this, there exist analytical solutions to the decoupled

normal and transverse wave equations

$$\frac{\partial^2 U}{\partial t^2} = C_L^2 \frac{\partial^2 U}{\partial x_1^2} \qquad \frac{\partial^2 V}{\partial t^2} = C_s^2 \frac{\partial^2 V}{\partial x_1^2} \tag{1.8}$$

where, U and V are normal and transverse displacements, respectively, C_L and C_s are the characteristic longitudinal and shear wave velocities, t is time, and x_1 is the Lagrangian spatial coordinate. Using the initial and boundary conditions, the solutions to the wave equations yield the expressions for the normal stress σ_{11}^s, shear stress σ_{12}^s, shear strain rate $\dot{\gamma}$ and shear strain γ in the sample as [60]

$$\sigma_{11}^s = -\frac{(\rho C_L)_a \, u_0}{2} \tag{1.9a}$$

$$\sigma_{12}^s = -\frac{(\rho C_s)_a v_{fs}}{2} \tag{1.9b}$$

$$\dot{\gamma} = \frac{v_0 - v_{fs}}{h} \tag{1.9c}$$

$$\gamma = \int \dot{\gamma} dt. \tag{1.9d}$$

Here, $(\rho C_L)_a$ and $(\rho C_s)_a$ corresponds to the mechanical and shear impedance of the anvil material, respectively, u_0 and v_0 are the normal and transverse component of the impact velocity depicted in Figure 1.5b, h is the thickness of the sample, and v_{fs} is the measured transverse free surface velocity. It is important to point out that generally, the Hugoniot elastic limits of anvils limit the pressures in the sample to below 6 GPa to avail the elastic analysis (Eqs. 1.9). To characterize materials at even higher normal stresses, the plasticity in the anvils must be accounted through a hybrid experimental-simulation methodology as described in [49, 63].

1.5 Scope of the thesis

This thesis explores the continuum response, strength and deformation mechanisms of BCC metals, specifically iron and molybdenum, under shock compression using plate impact experiments.

As mentioned earlier, iron undergoes a martensitic solid-to-solid phase transformation when subjected to normal stresses beyond 13 GPa. Phase transitions

provide a unique opportunity to study strength behavior as they play a crucial role in enhanced material properties and expand the material design space for various load-bearing applications. Thus, in Chapter 2, the role of shock-induced phase transformation on the dynamic strength of iron is explored. This is done experimentally using sandwich configuration pressure-shear plate impact (PSPI) experiments coupled with photonic Doppler velocimetry (PDV) measurements. In addition, finite element simulations are conducted to understand the effect of strain, temperature, and pressure on the evolution of the yield surface of iron.

In Chapter 3, the underlying microstructural reasons for the anisotropy of Hugoniot elastic limit (HEL) and, the governing plastic deformation mechanisms at the Hugoniot (steady) shock state and during release are explored for single crystal molybdenum. This is done using normal plate impact experiments coupled with *in-situ* Laue x-ray diffraction conducted at Dynamic Compression Sector [56] at the Advanced Photon Source [64]. To extract the lattice strains and stresses from the experimental images, a forward simulation methodology is developed. Using these results, the role of dislocation slip and deformation twinning in BCC metals is explored.

Lastly, in Chapter 4, concluding remarks are presented and future works is discussed.

References

[1] W. Zhang and J. Xu, "Advanced lightweight materials for Automobiles: A review," Materials & Design **221**, 110994 (2022).

[2] D. Sandstrom, "Armor/Anti-Armor Materials by Design," Los Alamos Science Summer **17**, 36–50 (1989).

[3] V. Madhu, K. Ramanjaneyulu, T. Balakrishna Bhat, and N. Gupta, "An experimental study of penetration resistance of ceramic armour subjected to projectile impact," International Journal of Impact Engineering **32**, 337–350 (2005).

[4] M. Itoh, M. Katayama, and R. Rainsberger, "Computer simulation of a boeing 747 passenger jet crashing into a reinforced concrete wall," Materials Science Forum **465-466**, 73–78 (2004).

[5] G. A. Graham, A. T. Kearsley, I. P. Wright, M. J. Burchell, and E. A. Taylor, "Observations on hypervelocity impact damage sustained by multi-layered insulation foils exposed in low earth orbit and simulated in the

laboratory," International Journal of Impact Engineering **29**, 307–316 (2003).

[6] R. F. Smith, D. E. Fratanduono, D. G. Braun, T. S. Duffy, J. K. Wicks, P. M. Celliers, S. J. Ali, A. Fernandez-Pañella, R. G. Kraus, D. C. Swift, and et al., "Equation of state of iron under core conditions of large rocky exoplanets," Nature Astronomy **2**, 452–458 (2018).

[7] R. W. Armstrong and S. M. Walley, "High strain rate properties of metals and alloys," International Materials Reviews **53**, 105–128 (2008).

[8] M. A. Meyers, *Dynamic behavior of materials* (John Wiley & Sons, 1994).

[9] K. Bhattacharya, *Microstructure of martensite: why it forms and how it gives rise to the shape-memory effect?* (Oxford University Press, 2012).

[10] S. Harjo, N. Tsuchida, J. Abe, and W. Gong, "Martensite phase stress and the strengthening mechanism in TRIP steel by neutron diffraction," Scientific Reports **7**, 15149 (2017).

[11] A. V. Jain and M. E. Lipschutz, "Implications of shock effects in iron meteorites," Nature **220**, 139–143 (1968).

[12] D. Batani, A. Morelli, M. Tomasini, A. Benuzzi-Mounaix, F. Philippe, M. Koenig, B. Marchet, I. Masclet, M. Rabec, C. Reverdin, R. Cauble, P. Celliers, G. Collins, L. Da Silva, T. Hall, M. Moret, B. Sacchi, P. Baclet, and B. Cathala, "Equation of state data for iron at pressures beyond 10 mbar," Physical Review Letters **88**, 235502 (2002).

[13] J. Wadsworth, T. G. Nieh, and J. J. Stephens, "Recent advances in aerospace refractory metal alloys," International Materials Reviews **33**, 131–150 (1988).

[14] J. A. Shields and P. Lipetzky, "Molybdenum applications in the electronics market," JOM **52**, 37–39 (2000).

[15] P. Lipetzky, "Refractory metals: A primer," JOM **54**, 47–49 (2002).

[16] D. Bancroft, E. L. Peterson, and S. Minshall, "Polymorphism of iron at high pressure," Journal of Applied Physics **27**, 291–298 (1956).

[17] L. M. Barker and R. E. Hollenbach, "Shock wave study of the $\alpha \rightleftharpoons \epsilon$ phase transition in iron," Journal of Applied Physics **45**, 4872–4887 (1974).

[18] J. C. Jamieson and A. W. Lawson, "X-ray diffraction studies in the 100 kilobar pressure range," Journal of Applied Physics **33**, 776–780 (1962).

[19] B. J. Jensen, G. T. Gray, and R. S. Hixson, "Direct measurements of the α-ϵ transition stress and kinetics for shocked iron," Journal of Applied Physics **105**, 103502 (2009).

[20] K. J. Caspersen, A. Lew, M. Ortiz, and E. A. Carter, "Importance of shear in the bcc-to-hcp transformation in iron," Physical Review Letters **93**, 115501 (2004).

[21] A. Lew, K. Caspersen, E. Carter, and M. Ortiz, "Quantum mechanics based multiscale modeling of stress-induced phase transformations in iron," Journal of the Mechanics and Physics of Solids **54**, 1276–1303 (2006).

[22] S. J. Wang, M. L. Sui, Y. T. Chen, Q. H. Lu, E. Ma, X. Y. Pei, Q. Z. Li, and H. B. Hu, "Microstructural fingerprints of phase transitions in shock-loaded iron," Scientific Reports **3**, 1–6 (2013).

[23] G. I. Kanel, S. V. Razorenov, A. V. Utkin, V. E. Fortov, K. Baumung, H. U. Karow, D. Rusch, and V. Licht, "Spall strength of molybdenum single crystals," Journal of Applied Physics **74**, 7162–7165 (1993).

[24] A. Mandal and Y. M. Gupta, "Elastic-plastic deformation of molybdenum single crystals shocked along [100]," Journal of Applied Physics **121**, 045903 (2017).

[25] A. Mandal and Y. M. Gupta, "Elastic-plastic deformation of molybdenum single crystals shocked to 12.5 GPa: Crystal anisotropy effects," Journal of Applied Physics **125**, 055903 (2019).

[26] J. N. Johnson, R. S. Hixson, D. L. Tonks, and G. T. Gray, "Shock compression and quasielastic release in tantalum," AIP Conference Proceedings **309**, 1095–1098 (1994).

[27] T. Oniyama, Y. M. Gupta, and G. Ravichandran, "Shock compression of molybdenum single crystals to 110 GPa: elastic–plastic deformation and crystal anisotropy," Journal of Applied Physics **127**, 205902 (2020).

[28] T. Oniyama, Y. M. Gupta, and G. Ravichandran, "Peak states of molybdenum single crystals shock compressed to high stresses," Journal of Applied Physics **129**, 245906 (2021).

[29] J. L. Brown, D. P. Adams, C. S. Alexander, J. L. Wise, and M. B. Prime, "Estimates of Ta strength at ultrahigh pressures and strain rates using thin-film graded-density impactors," Physical Review B **99**, 214105 (2019).

[30] M. B. Prime, A. Arsenlis, R. A. Austin, N. R. Barton, C. C. Battaile, J. L. Brown, L. Burakovsky, W. T. Buttler, S.-R. Chen, D. M. Dattelbaum, S. J. Fensin, D. G. Flicker, G. T. Gray, C. Greeff, D. R. Jones, J. M. D. Lane, H. Lim, D. Luscher, T. R. Mattsson, J. M. McNaney, H.-S. Park, P. D. Powell, S. T. Prisbrey, B. A. Remington, R. E. Rudd, S. K. Sjue, and D. C. Swift, "A broad study of tantalum strength from ambient to extreme conditions," Acta Materialia **231**, 117875 (2022).

[31] J. L. Brown, C. S. Alexander, J. R. Asay, T. J. Vogler, D. H. Dolan, and J. L. Belof, "Flow strength of tantalum under ramp compression to 250 GPa," Journal of Applied Physics **115**, 043530 (2014).

[32] M. B. Prime, W. T. Buttler, S. J. Fensin, D. R. Jones, J. L. Brown, R. S. King, R. Manzanares, D. T. Martinez, J. I. Martinez, J. R. Payton, and D. W. Schmidt, "Tantalum strength at extreme strain rates from impact-driven Richtmyer-Meshkov instabilities," Physical Review E **100**, 053002 (2019).

[33] J. L. Brown, M. B. Prime, N. R. Barton, D. J. Luscher, L. Burakovsky, and D. Orlikowski, "Experimental evaluation of shear modulus scaling of dynamic strength at extreme pressures," Journal of Applied Physics **128**, 045901 (2020).

[34] R. S. Hixson and J. N. Fritz, "Shock compression of tungsten and molybdenum," Journal of Applied Physics **71**, 1721–1728 (1992).

[35] D. P. Dandekar, "Loss of shear strength in polycrystalline tungsten under shock compression," Journal of Applied Physics **47**, 4703–4705 (1976).

[36] J. R. Asay, L. C. Chhabildas, and D. P. Dandekar, "Shear strength of shock-loaded polycrystalline tungsten," Journal of Applied Physics **51**, 4774–4783 (1980).

[37] K. T. Ramesh, "High rates and impact experiments," in *Springer handbook of experimental solid mechanics*, edited by W. N. Sharpe (Springer US, Boston, MA, 2008), pp. 929–960.

[38] T. Nicholas, *Dynamic Tensile Testing of Structural Materials Using a Split Hopkinson Bar Apparatus*, tech. rep. ADA092832 (Materials Laboratory, Air Force Wright Aeronatical Laboratories, Wright-Patterson Air Force Base, OH, 1980).

[39] J. Duffy, J. D. Campbell, and R. H. Hawley, "On the use of a torsional split hopkinson bar to study rate effects in 1100-0 aluminum," Journal of Applied Mechanics **38**, 83–91 (1971).

[40] A. Sreedhar S, S. Ravindran, G. Shankar, S. Suwas, and R. Narasimhan, "Fracture mechanism and toughness of a rolled magnesium alloy under dynamic loading," Acta Materialia **202**, 350–365 (2021).

[41] V. Deshpande and N. Fleck, "Isotropic constitutive models for metallic foams," Journal of the Mechanics and Physics of Solids **48**, 1253–1283 (2000).

[42] D. Rittel, G. Ravichandran, and A. Venkert, "The mechanical response of pure iron at high strain rates under dominant shear," Materials Science and Engineering: A **432**, 191–201 (2006).

[43] L. Barker and R. Hollenbach, "Laser interferometer for measuring high velocities of any reflecting surface," Journal of Applied Physics **43**, 4669–4675 (1972).

[44] Z. Sternberger, "Determining strength of materials under dynamic loading conditions using hydrodynamic instabilities," PhD thesis (California Institute of Technology, 2017).

[45] Y. Ping, F. Coppari, D. G. Hicks, B. Yaakobi, D. E. Fratanduono, S. Hamel, J. H. Eggert, J. R. Rygg, R. F. Smith, D. C. Swift, D. G. Braun, T. R. Boehly, and G. W. Collins, "Solid iron compressed up to 560 gpa," Physical Review Letters **111**, 065501 (2013).

[46] S. J. Turneaure, S. M. Sharma, and Y. M. Gupta, "Crystal structure and melting of Fe shock compressed to 273 gpa: In situ x-ray diffraction," Physical Review Letters **125**, 215702 (2020).

[47] A. S. Abou-Sayed, R. J. Clifton, and L. Hermann, "The oblique-plate impact experiment," Experimental Mechanics **16**, 127–132 (1976).

[48] O. T. Strand, D. R. Goosman, C. Martinez, T. L. Whitworth, and W. W. Kuhlow, "Compact system for high-speed velocimetry using heterodyne techniques," Review of Scientific Instruments **77**, 083108 (2006).

[49] C. Kettenbeil, Z. Lovinger, S. Ravindran, M. Mello, and G. Ravichandran, "Pressure-shear plate impact experiments at high pressures," Journal of Dynamic Behavior of Materials, 489–501 (2020).

[50] A. Joshi, S. Ravindran, V. Gandhi, and G. Ravichandran, "Probing the properties and mechanisms of failure waves in soda-lime glass," Journal of Applied Physics **129**, 185902 (2021),

[51] D. Dandekar, *Spall strength of tungsten carbide*, tech. rep. ARL-TR-3335 (U.S. Army Research Laboratory, Aberdeen Proving Ground, MD, 2004).

[52] T. J. Volz and Y. M. Gupta, "Elastic moduli of hexagonal diamond and cubic diamond formed under shock compression," Physical Review B **103**, L100101 (2021).

[53] L. M. Barker and R. E. Hollenbach, "Shock-wave studies of pmma, fused silica, and sapphire," Journal of Applied Physics **41**, 4208–4226 (1970).

[54] D. Bloomquist and S. Sheffield, "Optically recording interferometer for velocity measurements with subnanosecond resolution," Journal of Applied Physics **54**, 1717–1722 (1983).

[55] S. Ravindran, V. Gandhi, A. Joshi, and G. Ravichandran, "Three-dimensional full-field velocity measurements in shock compression experiments using stereo digital image correlation," Review of Scientific Instruments **94**, 025107 (2023).

[56] Y. M. Gupta, S. J. Turneaure, K. Perkins, K. Zimmerman, N. Arganbright, G. Shen, and P. Chow, "Real-time, high-resolution x-ray diffraction measurements on shocked crystals at a synchrotron facility," Review of Scientific Instruments **83**, 123905 (2012).

[57] J. A. Hawreliak and S. J. Turneaure, "Probing the lattice structure of dynamically compressed and released single crystal iron through the alpha to epsilon phase transition," Journal of Applied Physics **129**, 135901 (2021).

[58] S. J. Tracy, S. J. Turneaure, and T. S. Duffy, "In situ x-ray diffraction of shock-compressed fused silica," Physical Review Letters **120**, 135702 (2018).

[59] S. J. Tracy, S. J. Turneaure, and T. S. Duffy, "Structural response of α-quartz under plate-impact shock compression," Science Advances **6**, eabb3913 (2020).

[60] R. Clifton and R. Klopp, "Pressure shear plate impact testing," in, Vol. 8 (Metals Handbook, 1985), pp. 230–239.

[61] S. Grunschel, "Pressure-shear plate impact experiments on high-purity aluminum at temperatures approaching melt," PhD thesis (Brown University, 2009).

[62] C. Kettenbeil, M. Mello, M. Bischann, and G. Ravichandran, "Heterodyne transverse velocimetry for pressure-shear plate impact experiments," Journal of Applied Physics **123**, 125902 (2018).

[63] S. Ravindran, V. Gandhi, Z. Lovinger, M. Mello, and G. Ravichandran, "Dynamic strength of copper at high pressures using pressure shear plate experiments," Dynamic Behavior of Materials, 248–261 (2021).

[64] *The Advanced Photon Source: a U.S. Department of Energy Office of Science User Facility*, https://www.aps.anl.gov/.

Chapter 2

DYNAMIC STRENGTH AND PLASTICITY OF IRON

V. Gandhi, S. Ravindran, and G. Ravichandran, "Dynamic strength of iron at high pressures and strain rates," Physical Review Letters **128**, 015705 (2022)

Contributions: V.G. performed the experiments, prepared the experimental data, performed the numerical simulations, and wrote the manuscript.

Abstract

Accurate modeling of meteorite impacts, and deformation of planetary cores require characterization of the flow strength and in-elasticity of iron in its different phases. In this letter, we investigate the flow strength of both the ambient α-phase and high-pressure ϵ-phase of iron at strain-rates of 1×10^5 s^{-1} and pressures up to 42 GPa using high pressure–pressure shear plate impact experiments. We report the strength of the ϵ-iron to be significantly higher than α-phase but consequently one order smaller than the previously reported dynamic strength at high pressures. The complete stress-strain response of the ϵ-phase is reported for the first time.

2.1 Introduction

Iron has many geological and planetary implications as it is the primary constituent in the inner core of outer planets such as Uranus and Neptune [1], rocky exoplanets, and the inner rocky planets including earth where core pressures exceed 330 GPa [2]. Understanding the dynamic inelastic behavior of iron at high pressures is critical for many applications. These include modeling the physics of hyper-velocity impacts of iron-rich meteorites [3], the formation of craters on earth and moon [4], and planetary impact such as the giant-impact hypothesis on the formation of the earth-moon system [5–7]. Plasticity behavior of iron is also important for describing deformation mechanisms of the inner cores of rocky planets [8], for example due to seismic waves generated

from earthquakes. However, modeling iron at these high pressures is difficult because it undergoes a martensitic phase transformation [9] from the body centered cubic (BCC) α-phase to hexagonal closed-pack (HCP) ϵ-phase [10, 11] when subjected to 13 GPa of pressure.

Martensitic phase transformations, provide a unique opportunity to study strength behavior as they play a crucial role in enhanced material properties and expands the material design space for various applications. An illustrative and important example of this are iron alloys. Martensitic steels formed by rapid quenching yield high strength, high fatigue-resistant materials [12], whereas transformation induced plastic (TRIP) steels partially transform to martensite upon deformation thus resulting in improved strength and ductility [13]. This further motivates the study of plasticity behavior of ϵ-phase iron as it can help novel materials for load bearing applications.

While, the shocked equation of state [7, 14], the picosecond to nanosecond range of characteristic transition times [15], and even the importance of shear on the initiation of the BCC-HCP transformation [16] have provided considerable insight regarding the material behavior of the ϵ-phase, the strength and plasticity behavior of this martensite under dynamic conditions is still not fully explored. Iron completely reverts to its α-phase upon release of pressure hence this unstable nature of ϵ-iron has severely limited the possibility of developing a material model to describe its inelastic behavior.

Diamond anvil compression (DAC) experiments coupled with XRD have provided initial insight regarding the low strain-rate strength of iron at core pressures. Hemley et al. [17] observed pressure hardening of ϵ-iron and deduced a shear stress of $\tau \approx 10$ GPa at $200-300$ GPa of pressure. This significantly differs from more recent DAC experiments [8, 18] which suggest half the strength and indicate a linear relationship between shear strength and pressure. While the static data is promising, the limitations include the determination of only a single data point for strength measurements at a constant pressure and the indirect nature of XRD yields high uncertainties.

Despite the importance, dynamic strength characterization of ϵ-iron has been limited. Extended x-ray absorption fine structure (EXAFS) measurements on laser shocked polycrystalline iron by Ping et al. [19] provide preliminary, and indirect dynamic strength characterizations on ϵ-iron under quasi-isentropic conditions. The authors interpolate plastic work contribution to the tempera-

ture measurements to estimate the strength of ϵ-iron up to 560 GPa of pressure. However, this measurement involves very high uncertainties on the order of 50%. A more recent study by Huntington et al. [20] utilizes Rayleigh-Taylor instability experiments to observe the ripple growth of iron, laser shocked to 100 GPa, to extract the material strength. The authors obtained yield strengths of 40 GPa at these pressures which are comparable to Ping et al. [19], but are on cusp of theoretical strength limits.

In this letter, we report the measurement of the pressure dependent dynamic strength behavior of α- and ϵ-iron under quasi-isentropic loading conditions, using the recently developed sandwiched high pressure - pressure shear plate impact [21] (HP-PSPI) technique. Experiments are conducted on iron at pressures ranging from 10 to 42 GPa and a constant compressive and shearing strain-rate of 10^5 s^{-1}. Additionally, simulations are conducted to model the equation of state and plasticity of both phases of iron. By varying parameters within the plasticity model, the simulated normal and transverse free surface velocities are matched with experimentally determined quantities to determine the first ever complete shear stress-strain behavior of iron.

2.2 Materials and methods

In PSPI experiments [22], the oblique impact generates both longitudinal and shear waves in the front anvil, which first compresses and then shears the sample at a constant pressure. The HP-PSPI experiments were performed on annealed Armco iron (purity 99.8%) with an average grain size 70 μm using a slotted barrel powder gun. A 150 μm thin iron sample was sandwiched between tungsten carbide (WC) anvils to ensure the sample equilibrates to a constant pressure before it is sheared. The sandwich is assembled by placing the iron sample between the anvils such that the iron-WC interfaces are directly in contact with one another and friction between the materials transmits the shear wave. Both normal and transverse free surface velocity measurements [23] were conducted using photon doppler velocimetry (PDV) [24]. Figure 2.1a illustrates the experimental setup.

2.2.1 Iron Material

The chemical composition of the iron is displayed in Table 2.1. The stock material was first stress relief annealed at 700 °C to achieve an average grain

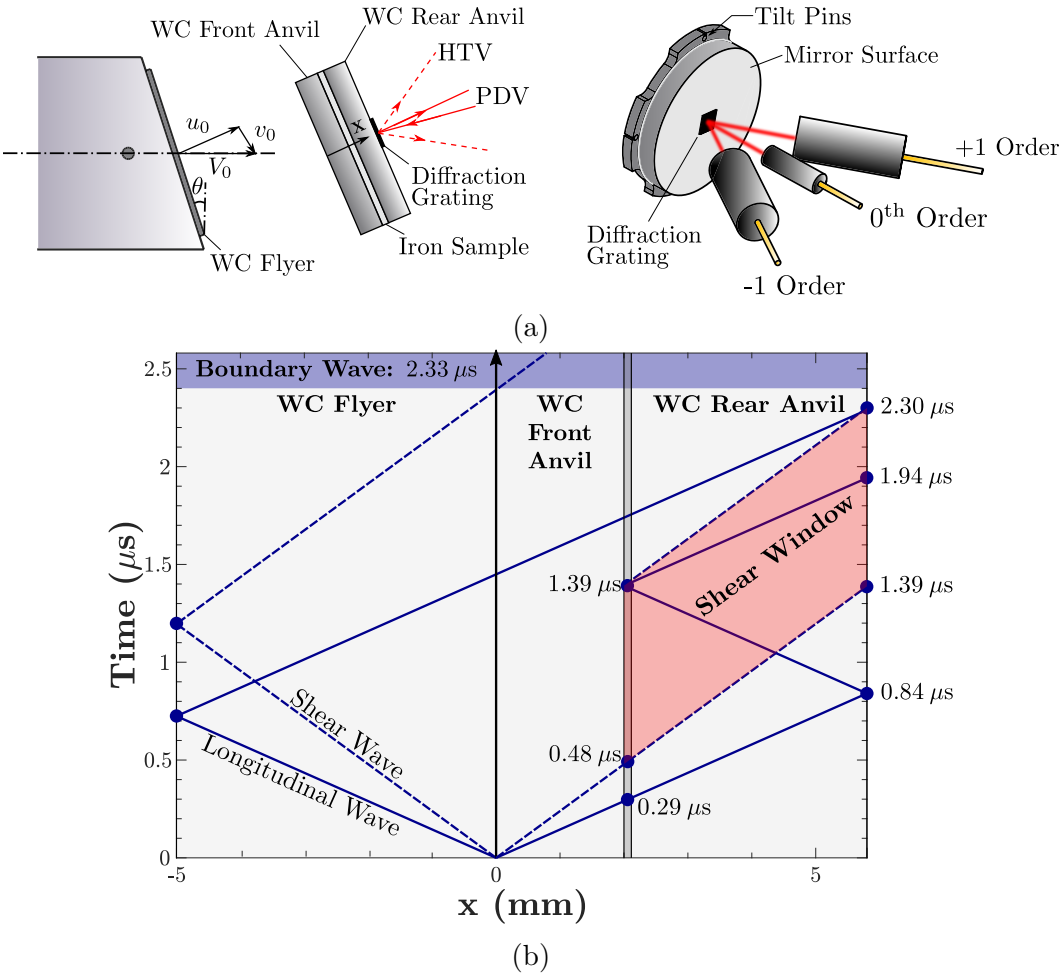

Figure 2.1: Experimental configuration used to characterize the dynamic strength of iron. (a) Schematic of the pressure shear plate impact setup in sandwich configuration. (b) Distance-time ($x-t$) diagram for tungsten carbide-iron sandwich assuming elastic wave propagation.

size of 70 μm as shown in Figure 2.2. Next, a 30 mm diameter with 2 mm thickness disk was extracted from this annealed material and lapped flat down to $150-160$ μm thickness with $1-2$ μm parallelism.

2.2.2 Sample Preparation

PSPI experiments in a sandwich configuration require a flyer plate, front and rear anvils, and a sample, iron. Here due to their high impedance and strength, BC-00 grade tungsten carbide (WC) material, sourced from Basic Carbide Corporation (Lowber, PA), was used for the anvils. Additionally, to ensure symmetric conditions upon impact, WC was also used as the flyer material.

Table 2.1: Composition of Armco iron [25]

Element	**wt.%**
Fe	99.8
C	0.006
Si	0.021
Mn	0.058
P	0.003
S	0.002
Cr	0.023
Ni	0.027
Mo	0.003
V	<0.0002
Wu	<0.0007
Co	0.0041
Cu	0.01
Sn	0.004
Al	0.003
Ti	0.0004
Pb	0.0002
B	0.0001
Nb	<0.0004
N	0.005

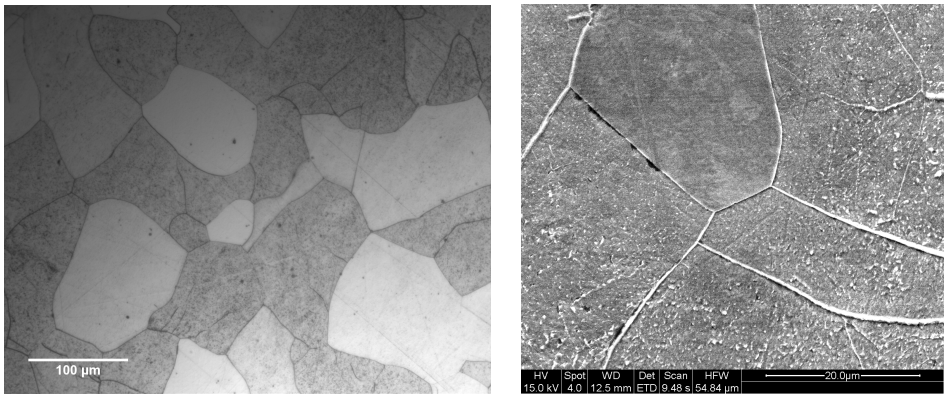

(a) (b)

Figure 2.2: Microstructure of Armco Iron obtained using (a) optical microscope (OM) and (b) scanning electron microscope (SEM).

The density and sound speeds of iron (measured) and WC (from literature [26]) are summarized in Table 2.2.

Due to the stringent requirements in a PSPI experiment, tremendous precision went into sample preparation. Thus, all anvil, and flyer plates were first lapped flat and parallel to within 10 μm. Since the iron is very thin, the material was sourced out to Production Lapping Co. (Monrovia, CA) for lapping to ensure parallelism within 2 μm. The lapping roughens the surface of the material giving the tungsten carbide a roughness of $Rq = 200$ nm and iron of $Rq = 150$ nm as seen in the atomic force microscopy (AFM) data in Figure 2.3. The flatness was inspected using an optical flat and 550 nm monochromatic light where two or less circular Fizeau fringes were deemed acceptable for the current experiments. This corresponds to a flatness variation on the order of 0.5 μm across the plate surface. Once the plates satisfy the required criteria, the flyer is glued onto the projectile and the rear anvil is mirror polished on one side. Here, a 400 lines/mm diffraction grating is deposited onto the center using e-beam lithography. With the anvils and iron sample prepared, the sandwiched target is assembled next.

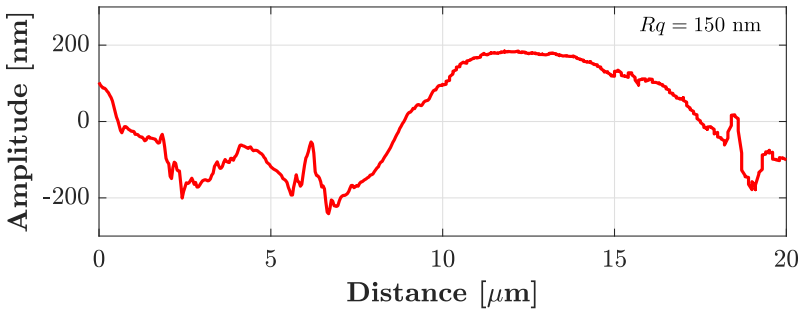

Figure 2.3: Surface roughness of iron probed along a line from AFM data. The average roughness across the entire area was measured to be $Rq = 150$ nm.

For the sandwich, the front anvil is first placed on a granite flat. The lapped iron sample is placed directly on top of the front anvil such that the two materials are directly in contact with each other. The rear anvil is similarly placed on top of the iron sample with the diffraction grating facing out. A series of weights are then placed on the sandwich to ensure the material interfaces are directly in contact with one another and no air gaps are present. Epoxy is next applied to the sides of the sandwich circumferentially. Once the epoxy cures after 24 hours, the weights are removed and the total thickness of the sandwich is measured once again to ensure no air gaps or epoxy are present at

the interfaces. Since the interfaces have perfect contact, the friction between the sample and the anvils transmit the shear wave in the target. The static coefficient between the iron sample and the WC anvils was measured to be 0.53 ± 0.01.

2.2.3 Experimental Procedures

As stated earlier, high pressure–pressure shear plate impact (HP-PSPI) experiments were conducted on high purity (99.8%) Armco iron in a powder gun with a 3 meter long and 38.7 mm bore diameter slotted barrel. In a PSPI experiment, the projectile is skewed with respect to its direction of travel. Due to the obliqueness of the projectile, both longitudinal and shear waves propagate within the flyer-target assembly. As discussed earlier, we employed a sandwich configuration PSPI experiment where the thin iron plate was sandwiched between two tungsten carbide (WC) anvils. The front anvil thickness is designed such that upon impact, the faster longitudinal wave pressurizes the iron sample to an equilibrium state before the arrival of the shear wave. This is illustrated in Figure 2.1b. The longitudinal wave continues to propagate through the iron and into the rear anvil. Once it reaches the rear surface it reflects back as a tensile unloading wave. The time at which the shear wave arrives at the iron-front anvil interface to the time at which the unloading wave reaches the iron-rear anvil interface is regarded as the shear window. During this time, the friction between iron and the loading plates transmits shear stress through the sample. The shear window is projected to the free surface of the rear anvil. For a valid experiment, the end of the shear window must reach the center of the free surface, where diagnostics are conducted, before the arrival of boundary waves at this point. These lateral relief waves are generated from the circular boundary of the front anvil and travel diagonally into the sample at the longitudinal wave speed. Therefore, the rear anvil thickness is designed to maximize this shear window before the arrival of the lateral relief wave at the center of the free surface.

To ensure a maximized shear window, the front anvil had a diameter of 34 mm and a thickness of 2 mm, the rear anvil had a diameter of 30 mm and a thickness of 3.8 mm, and the flyer material had a 34 mm diameter and a 5 mm thickness. The exact dimensions of the plates for each experiment are summarized in Table 2.3. It is important to mention that since the grain size

of the iron sample is approximately 70 μm and the thickness ranges from 150 − 160 μm, this implies there are only two grains along thickness direction and thus, the sample cannot represent the representative volume element (RVE) of the material. However, it was previously observed experimentally by laser shocking single crystal iron samples that were 200-270 μm thick [27] and using x-ray diffraction, that when the compression wave passes through the material, the BCC to HCP transformation generates a nanocrystalline grain structure with grain sizes of 2-15 nm within the material. In our experiments, the material behavior due to the shear wave is observed after the material has phase transformed. At first, in the direction of the applied shear, the total number of grains are already significant. Once the phase transformation has occurred, the nanocrystalline structure of iron ensures enough grains in the thickness direction to represent an RVE. Thus, the response observed in our experiments is assumed to be an average response rather than single crystal behavior.

In these experiments, the out-of-plane velocity measurements were conducted at the free surface of the rear anvil. This was done using photonic Doppler velocimetry (PDV) and heterodyne transverse velocimtery (HTV) [28] with a 1550 nm wavelength laser. Once this laser hits the grating, it diffracts 0^{th} and ± 1 order beams. The 0^{th} order beam is interfered with a reference laser to extract the normal free surface velocity measurement. The diffracted +1 order beam is frequency shifted through an acousto-optical driver and interfered with the diffracted -1 order beam to extract the transverse free velocity measurements.

Table 2.2: Material properties

Material	$\boldsymbol{\rho}$ **(kg/m^3)**	$\mathbf{C_L}$ **(m/s)**	$\mathbf{C_s}$ **(m/s)**
Tungsten Carbide [26]	15600	6921±97	4324±50
Armco Iron	7870±11	5969±54	3253±16

2.3 Experimental results

Five HP-PSPI experiments were conducted on iron ranging from the α-phase (10 GPa) to ε-phase (42 GPa). A detailed summary of the experiments including impact velocities, pressures, and impact angles is shown in Table 2.4.

Table 2.3: Dimensions of flyer, anvils, and sample

Experiment	Flyer [mm]	Front Anvil [mm]	Sample [mm]	Rear Anvil [mm]
Fe-WC-1	4.969±0.002	1.969±0.002	0.159±0.001	3.774±0.002
Fe-WC-2	4.972±0.003	1.991±0.002	0.152±0.001	3.769±0.003
Fe-WC-3	4.986±0.003	1.988±0.003	0.150±0.001	3.748±0.002
Fe-WC-4	4.996±0.001	2.005±0.003	0.165±0.000	3.761±0.002
Fe-WC-5	4.949±0.005	1.994±0.002	0.156±0.001	3.835±0.003

**WC flyer and front anvil plates were 34 mm in diameter
**Iron sample and WC rear anvil plates were 30 mm in diameter

Additionally, the experimentally determined free surface velocities are plotted in Figure 2.4.

Table 2.4: Summary of performed experiments.

Experiment	Pressure [GPa]	θ	u_0 [m/s]	v_0 [m/s]	u_{fs} [m/s]	v_{fs} [m/s]	Tilt [mrad]	$\tau_{10\%}$ [GPa]	$\dot{\gamma}$ [s^{-1}]
Fe-WC-1	10.0±0.01	18°	203.83±0.02	66.22±0.01	196.66±0.18	19.13±0.14	0.7	0.60±0.03	2.5×10^5
Fe-WC-2	15.8±0.02	18°	344.83±0.01	112.04±0.00	327.37±0.42	53.06±0.19	2.0	1.46±0.07	3.2×10^5
Fe-WC-3	21.5±0.02	12.5°	473.17±0.02	104.89±0.01	454.74±0.37	54.05±0.25	0.2	1.80±0.09	2.4×10^5
Fe-WC-4	30.2±0.06	9°	676.47±0.03	107.14±0.01	649.23±1.34	56.42±0.46	1.3	1.96±0.10	1.5×10^5
Fe-WC-5	42.0±0.01	6°	930.72±0.08	97.82±0.01	898.92±0.09	48.26±0.38	0.6	2.15±0.11	1.5×10^5

**θ corresponds to the skew angle of the projectile
**u_0 is the normal component of the impact velocity and also the measured velocity
**u_{fs} and v_{fs} are measured peak normal and transverse free surface velocities

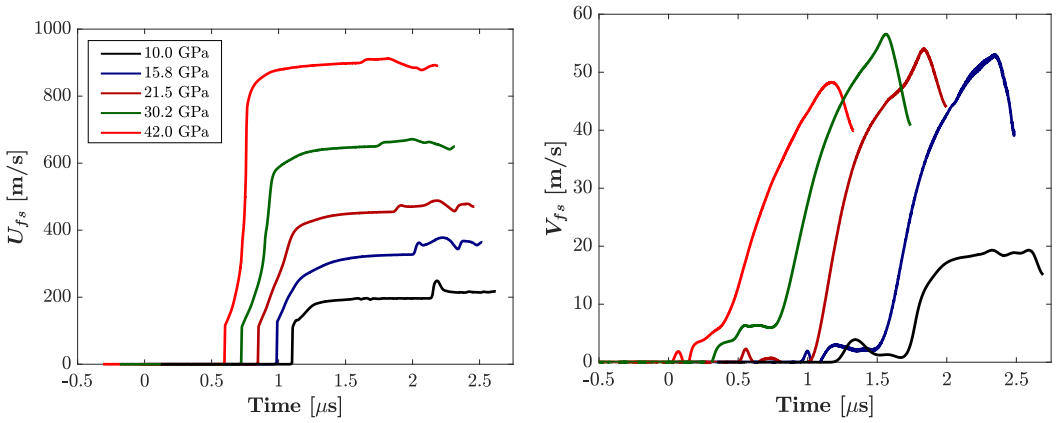

(a) (b)

Figure 2.4: Experimental (a) normal and (b) transverse free surface velocities. The profiles are shifted in time for visual purposes.

Due to plasticity within our WC anvils and the thickness of our iron sample, no phase transformation wave is observed in the normal profile. Additionally, the very thin sample does not affect the normal profile in terms of Hugoniot elastic limit (HEL) and peak free-surface velocity. This is because the peak velocity due to the arrival of the elastic wave ($\sim$ 113 m/s) corresponds to the

elastic limit of the tungsten carbide anvils. However, due to the impedance mismatch between iron and WC, pressure reverberations upon the arrival of the initial longitudinal wave slightly affect the rise times of the shock wave. This further validates the quasi-isentropic loading condition in the sandwiched sample. Additionally, as shown in Table 2.4, the initial condition on transverse velocity (v_0) is consistent throughout the experiments. Regardless, looking at the transverse free surface velocity profiles, the peak velocities are much lower than the imposed. This indicates the dispersion of the shear wave due to plasticity from the sample and the anvils. Nonetheless, the elastic solutions cannot be used here and thus, simulations are conducted. Prior to the discussion on simulation methodology, a question then arises on the uncertainty of the experimental velocity measurements.

The uncertainties within the measured velocity profiles are primarily due to identifying peak frequencies in its power spectrum [23] and the impact tilt. The quantification of the frequency uncertainty of the velocities was conducted using Dolan's [29] approach. The velocity uncertainty can be expressed as:

$$\Delta \dot{u}_i = \mathcal{S}_i \sqrt{\frac{6}{f_{sa}}} \frac{\sigma}{\pi} \tau^{-3/2}, \qquad i = 1, 2. \tag{2.1}$$

Here, $\Delta \dot{u}_1$ corresponds to the normal velocity error and $\Delta \dot{u}_2$ corresponds to the transverse velocity error. Additionally, the terms $\mathcal{S}_i$ correspond to the interferometer sensitivities, $f_{sa} = 20$ GSa/s is the sampling frequency, σ is the signal noise fraction and τ is the hamming window. The interferometer sensitivities are $\mathcal{S}_1 = \lambda/2$ for normal and $\mathcal{S}_2 = d/2$ for shear where $d = 1/400$ mm is the grating pitch. Based on Eq. 2.1, a smaller hamming window results in a higher uncertainty in velocity. However, to capture the sharp rise times associated with the elastic and plastic waves in the normal profile, a hamming window of 40 ns was implemented resulting in uncertainties up to 1.4 m/s. For the transverse velocity profile, the rise times are relatively high, especially at higher pressures, thus a larger hamming window of 100 ns was used resulting in uncertainties up to 0.5 m/s. From this analysis itself the uncertainties in the transverse velocity profiles are on the order of 0.5%. We next consider the effect of tilt on the transverse velocity profiles. Tilt affects the loss of coupling efficiencies of the transverse probes. However, it was shown in [23] that uncertainties caused by these small angle variations for transverse velocity

due to tilt > 0.5 mrad is below 0.08%. Overall, the uncertainties in velocity measurements are relatively low $< 1\%$.

For the uncertainties associated with the strength calculations, there are also numerical errors from the simulations which will be discussed in future sections.

2.4 Simulation methodology

Due to plasticity within the anvil material above its Hugoniot elastic limit (HEL), conventional elastic analysis of extracting strength from transverse velocity profiles is not feasible. For this reason, we conduct finite element simulations via ABAQUS Explicit [30] and match simulated velocities with the experimental quantities [21, 26] to extract a material model for the iron sample. In particular, the peak transverse velocity is directly related to the strength and flow behavior of iron and thus we determine simulation parameters to match peak velocities of the experimental data. This sandwich configuration and plastically deforming anvil analysis methodology has been successfully validated using various anvil materials on copper [26]. Thus, the key results in this letter represent the physics of iron and are not from an unknown error in the experimental or analysis method. For a known tungsten carbide material model [26], the only unknowns required to match our experimental velocity profiles are equation of state and strength parameters for iron. For α-iron, a Johnson-Cook strain and strain-rate hardening model with temperature softening from Sadjadpour et al. [31] was implemented. For ϵ-iron, we employ the Johnson-Cook hardening law with temperature dependence and a Steinberg-Cochran-Guinan (SCG) [32] pressure dependence on yield strength as follows:

$$Y = (Y_0 + B\epsilon^n)\left(1 - T^{*m}\right)\left(1 + \left(\frac{Y_p'}{Y_0}\right)\frac{P}{\eta^{1/3}} - \left(\frac{\mu_T'}{\mu_0}\right)(T - 300\text{ K})\right) \tag{2.2}$$

where $\mu_0 = 83$ GPa [8] is the shear modulus at ambient conditions, $T^* = \frac{T - T_r}{T_m - T_r}$ with T corresponding to the temperature, $T_r = 300$ K the reference temperature, $T_m = 1811$ K [31] the melting temperature, and $\eta = \frac{\rho}{\rho_0}$ the compression ratio with ρ being the density, and $\rho_0 = 7870$ kg/m^3 [31] the reference density. From Equation 2.2, the initial yield Y_0, the strain hardening terms, B and n, and the temperature softening exponent, m were varied in simulations

to match experimental velocities whereas the other parameters were obtained from previous literature. The strain-rate dependence in the Johnson-Cook model was neglected as all experiments were conducted at a nominally constant strain-rate, 10^5 s^{-1}. Within our simulations, the temperature contributions include both plastic work from high strain-rate deformations (assuming Taylor-Quinney factor of $\beta = 1$ [25, 31]) and shock heating due to high pressure jumps which was modeled using an equation of state (EOS). The EOS of iron for all experiments was modeled using a well calibrated Helmholtz potential by Boettger and Wallace [14] in conjunction with a continuum time-dependent phase transformation numerical scheme by Hayes [33] and Andrews [34]. This was implemented to accurately capture the two-phase region, specifically for the 15.8 GPa experiment.

When considering the yield strength scaling with respect to pressure, the SCG model approximates a one-to-one relationship between the pressure dependence behavior of shear modulus and yield strength $\left(\frac{1}{Y_0}\frac{\partial Y}{\partial P} = \frac{1}{\mu_0}\frac{\partial \mu}{\partial P}\right)$. However, recent experiments on Tantalum [35] and Copper [26] have shown the yield strength scaling to be 2 and 2.6 times that of shear modulus, respectively. This was based on the decrease of dislocation mobility at higher pressures and the shear modulus scaling of work required to move the dislocations [36]. In the present study, a one-to-one scaling of shear modulus and yield strength with respect to pressure was sufficient to simultaneously match both normal and transverse velocities for ϵ-iron. We adapt the ϵ-iron shear modulus data from static experiments [8]: $\frac{1}{\mu_0}\frac{\partial \mu}{\partial P} = 0.0246$ GPa^{-1} and $\frac{1}{\mu_0}\frac{\partial \mu}{\partial T} = 1.08$ kK^{-1}. The plot of the shear modulus as a function of pressure can be found in Mao et al. [37]. This governs the chosen parameters for the pressure hardening and temperature softening law. The other parameters in the Johnson-Cook model were fit to match the free surface velocity profiles of the four experiments. Specifically, we match the peak transverse velocities as they are directly related to material strength and the flow behavior.

Detailed description of the EOS, the numerical scheme, and the methodology for determining the strength parameters are presented next.

2.4.1 Helmholtz Free Energy

This multiphase equation of state (EOS) was implemented primarily to resolve the transition region of iron where both α- and ϵ-phases coexist. The model

followed the numerical scheme proposed by Andrews [34] and Hayes [33] using a known Helmholtz free energy as a function of specific volume and temperature from the work of Boettger and Wallace [14]. The functional form of the free energy is as follows:

$$F(V,T) = \Phi_0(V) + F_H(V,T) + F_A(V,T) + F_E(V,T) \tag{2.3}$$

where, $\Phi_0(V)$ is the static lattice potential, $F_H(V,T)$ corresponds to the quasi-harmonic phonon free energy, $F_A(V,T)$ is the anharmonic contribution, and $F_E(V,T)$ is the thermal excitation of electrons from their ground state. Note that the anharmonic contribution of the free energy is assumed to be of the order of experimental error and therefore assumed negligible [14].

The static lattice potential term corresponds to the cold energy term and is a modification of the Vinet-Ferrante-Rose-Smith (VFRS) universal form:

$$\begin{aligned} \Phi_0(V) &= \Phi^* + \tfrac{4V^*B^*}{\left(B_1^*-1\right)^2}\left[1-(1+\eta)e^{-\eta}\right] \\ \eta &= \tfrac{3}{2}\left(B_1^*-1\right)\left(\tfrac{V}{V^*}-1\right) \end{aligned} \tag{2.4}$$

where, V^* is the volume at which $\Phi_0(V)$ is minimum, Φ^* is the value of $\Phi_0(V)$ at V^*, B^* is the bulk modulus at V^*, and B_1^* is the derivative of bulk modulus with pressure at V^*.

The quasiharmonic phonon energy term is utilized at high temperatures and is expressed as follows:

$$F_H(V,T) = 3NkT\left[-\ln\left(\frac{T}{\theta_0(V)}\right) + \frac{1}{40}\left(\frac{\theta_2(V)}{T}\right)^2\right] \tag{2.5}$$

where, N is the Avogadro Number, k is the Boltzmann constant, θ_0 is the zeroth order Debye temperature, and θ_2 is the second order Debye temperature. The Debye temperatures satisfy $\gamma_{0,2} = dln\theta_{0,2}/d\ln V$. We assume that $\gamma_0 = \gamma_2$ [14] hence we obtain that the debye temperatures follow:

$$\theta_{0,2} = \hat{\theta}_{0,2}\left(\frac{V}{V_{300}}\right)^{-\gamma_{0,2}}. \tag{2.6}$$

The last term in the free energy is thermal excitation. This term can be decomposed into two different contributions. The first contribution occurs due

to normal conduction free energy and the second via magnetic free energy. The conduction free energy is expressed as

$$F_{cond}(V,T) = -\frac{1}{2}\beta_0 \left(\frac{V}{V_{300}}\right)^{\kappa} T^2 \qquad \kappa = \mathrm{d}\ln\Gamma/\mathrm{d}\ln V \tag{2.7}$$

where, β_0 is the coefficient of linear aspect of the electronic specific heat, Γ is the electronic Grüneisen parameter, and V_{300} is the specific volume at $T = 300$ K, and $P = 1$ Bar.

Additionally the magnetic term is the following,

$$F_{mag}(T) = a^3 b \left[\left(1 - \frac{T}{a^2}\right)\ln\left(\frac{1+\sqrt{T/a^2}}{1-\sqrt{T/a^2}}\right) - 2\sqrt{\frac{T}{a^2}} + \frac{4}{3}\left(\frac{T}{a^2}\right)^{3/2}\right] \tag{2.8}$$

where, $a^3 b$ and a^2 are both fitting parameters. Note that the magnetic contribution only occurs until the Curie temperature ($T_c = 1043$ K). This temperature has no pressure dependence, hence the magnetic contribution is volume independent. It is important to note that only the α-phase is magnetic and not the ϵ-phase, hence the magnetic contribution only occurs in the low pressure phase.

The constants used in computing the free energy were obtained from experimental results of previous literature and some fitting parameters were obtained via matching experimental results from Barker and Hollenbach [14]. These constants are shown in Table 2.5 below.

2.4.2 Continuum EOS Model

With the formulation of the thermodynamic variables, the continuum model for the multiphase equation of state is developed next. We employ the Andrews [34]/ Hayes [33] algorithm to formulate an explicit method.

We define the volume fraction of each phase, denoted λ with $0 \leq \lambda \leq 1$, such that $\lambda = 0$ is the α-phase and $\lambda = 1$ corresponds to the ϵ-phase. Note due to the intensive nature of pressure (P) and temperature (T), the two quantities in both of the phases of iron are the same at all times. Additionally, the subscripts α and ϵ for each thermodynamic property are defined such that they correspond to the thermodynamic variable of that respective phase. The

Table 2.5: Parameters for the free energy of the two different phases (α, ϵ) of iron.

Parameter	$\boldsymbol{\alpha}$	$\boldsymbol{\epsilon}$
V_{300} (m^3/kg)	127.0123 x 10^{-6}	120.512 x 10^{-6}
θ_0 (K)	301	264
θ_2 (K)	420	364
γ_0	1.82	2.8
β_0 (J/kg K^2)	44.767 x 10^{-3}	44.767 x 10^{-3}
$d\ \ln\Gamma/d\ \ln V$	1.3	1.3
a^2 (K)	1135	-
$a^3 b$ (J/kg)	83.803 x 10^3	-
V^* (m^3/kg)	125.431 x 10^{-6}	118.155 x 10^{-6}
B^* (GPa)	176.64	181.5
B_1^*	4.7041	5.74
Φ^* (J/kg)	0	99.0778 x 10^3

total specific volume and total specific internal energy as a function of pressure, temperature, and volume fraction are

$$V(P,T,\lambda) = (1-\lambda)V_\alpha(P,T) + \lambda V_\epsilon(P,T) \tag{2.9a}$$

$$U(P,T,\lambda) = (1-\lambda)U_\alpha(P,T) + \lambda U_\epsilon(P,T). \tag{2.9b}$$

Taking the differential of the total specific volume and specific internal energy:

$$\begin{aligned} dV &= (1-\lambda)\, dV_\alpha + \lambda dV_\epsilon + (V_\epsilon - V_\alpha)\, d\lambda \\ &= \left(\frac{\partial V}{\partial p}\right)_{T,\lambda} dp + \left(\frac{\partial V}{\partial T}\right)_{p,\lambda} dT + \left(\frac{\partial V}{\partial \lambda}\right)_{p,T} d\lambda \end{aligned} \tag{2.10}$$

$$\begin{aligned} dU &= (1-\lambda)\, dU_\alpha + \lambda dU_\epsilon + (U_\epsilon - U_\alpha)\, d\lambda \\ &= \left(\frac{\partial U}{\partial p}\right)_{T,\lambda} dp + \left(\frac{\partial U}{\partial T}\right)_{p,\lambda} dT + \left(\frac{\partial U}{\partial \lambda}\right)_{p,T} d\lambda. \end{aligned} \tag{2.11}$$

Assume for now that dV, dU, and the partials are known. The only unknowns in equations 2.10 and 2.11 are the differentials dp, dT, and $d\lambda$ but this indicates that there are 2 equations and 3 unknowns. Fortunately, the intersection of the Gibbs free energy in the pressure-temperature surface of the two phases at the point of phase transformation provides the third equation. This third equation is called the Clausius-Clapeyron relation and is expressed as:

$$d\left(G_\epsilon - G_\alpha\right) = \left(V_\epsilon - V_\alpha\right) dp - \left(S_\epsilon - S_\alpha\right) dT \tag{2.12}$$

where, G and S are the Gibbs free energy and Entropy, respectively.

Under the condition that $d\left(G_\epsilon - G_\alpha\right) = 0$ means that the mixed phases are in equilibrium. However, this equation does not help explain the metastable region that iron follows or describe the hysteresis experienced upon release of pressure. An alternate approach (Hayes formulation [33]) can be used with an assumption that $d\lambda$ is known. Rearranging equations 2.10 and 2.11 while recalling that $\left(\frac{\partial V}{\partial \lambda}\right)_{p,T} = \left(V_\epsilon - V_\alpha\right)$ (from Equation 2.9a) and similar for energy,

$$dV_\lambda = dV - \left(V_\epsilon - V_\alpha\right) d\lambda = \left(\frac{\partial V}{\partial p}\right)_{T,\lambda} dp + \left(\frac{\partial V}{\partial T}\right)_{p,\lambda} dT \tag{2.13a}$$

$$dU_\lambda = dU - \left(U_\epsilon - U_\alpha\right) d\lambda = \left(\frac{\partial U}{\partial p}\right)_{T,\lambda} dp + \left(\frac{\partial U}{\partial T}\right)_{p,\lambda} dT. \tag{2.13b}$$

This new problem can be rearragned into a linear system of equations and can be expressed as:

$$\begin{bmatrix} dV_\lambda \\ dU_\lambda \end{bmatrix} = \begin{bmatrix} \left(\frac{\partial V}{\partial p}\right)_{T,\lambda} & \left(\frac{\partial V}{\partial T}\right)_{p,\lambda} \\ \left(\frac{\partial U}{\partial p}\right)_{T,\lambda} & \left(\frac{\partial U}{\partial T}\right)_{p,\lambda} \end{bmatrix} \begin{bmatrix} dp \\ dT \end{bmatrix}. \tag{2.14}$$

Inverting the matrix to solve for dp, and dT,

$$\begin{bmatrix} dp \\ dT \end{bmatrix} = \frac{1}{J} \begin{bmatrix} \left(\frac{\partial U}{\partial T}\right)_{p,\lambda} & -\left(\frac{\partial V}{\partial T}\right)_{p,\lambda} \\ -\left(\frac{\partial U}{\partial p}\right)_{T,\lambda} & \left(\frac{\partial V}{\partial p}\right)_{T,\lambda} \end{bmatrix} \begin{bmatrix} dV_\lambda \\ dU_\lambda \end{bmatrix}. \tag{2.15}$$

Here, $J = \left(\frac{\partial V}{\partial p}\right)_{T,\lambda} \left(\frac{\partial U}{\partial T}\right)_{p,\lambda} - \left(\frac{\partial V}{\partial T}\right)_{p,\lambda} \left(\frac{\partial U}{\partial p}\right)_{T,\lambda}$ is the determinant and the partials are defined as

$$\left(\frac{\partial V}{\partial p}\right)_{T,\lambda} = (1-\lambda)\left(\frac{\partial V_\alpha}{\partial p}\right)_T + \lambda\left(\frac{\partial V_\epsilon}{\partial p}\right)_T \tag{2.16a}$$

$$\left(\frac{\partial V}{\partial T}\right)_{p,\lambda} = (1-\lambda)\left(\frac{\partial V_\alpha}{\partial T}\right)_p + \lambda\left(\frac{\partial V_\epsilon}{\partial T}\right)_p \tag{2.16b}$$

$$\left(\frac{\partial U}{\partial p}\right)_{T,\lambda} = (1-\lambda)\left(\frac{\partial U_\alpha}{\partial p}\right)_T + \lambda\left(\frac{\partial U_\epsilon}{\partial p}\right)_T \tag{2.16c}$$

$$\left(\frac{\partial U}{\partial T}\right)_{p,\lambda} = (1-\lambda)\left(\frac{\partial U_\alpha}{\partial T}\right)_p + \lambda\left(\frac{\partial U_\epsilon}{\partial T}\right)_p. \tag{2.16d}$$

Additionally, after simple manipulation of thermodynamic expressions, Maxwell relations, and reciprocity relations, one can obtain the following expressions:

$$\left(\frac{\partial V_i}{\partial p}\right)_T = -V_i/K_{Ti} \tag{2.17a}$$

$$\left(\frac{\partial V_i}{\partial T}\right)_p = V_i\alpha_i \tag{2.17b}$$

$$\left(\frac{\partial U_i}{\partial p}\right)_T = pV_i/K_{Ti} - TV_i\alpha_i \tag{2.17c}$$

$$\left(\frac{\partial U_i}{\partial T}\right)_p = -pV_i\alpha_i + C_{pi} \tag{2.17d}$$

where $i = \alpha, \epsilon$ the two different phases.

Using these relations, the exact expression for the determinant in Equation 2.15 becomes

$$\begin{aligned} J = &-(1-\lambda)^2\frac{C_{p\alpha}V_\alpha}{K_{S\alpha}} - \lambda^2\frac{C_{p\epsilon}V_\epsilon}{K_{S\epsilon}} \\ &+ \lambda(1-\lambda)\left(2TV_\alpha V_\epsilon\alpha_\alpha\alpha_\epsilon - \frac{C_{p\epsilon}V_\alpha}{K_{T\alpha}} - \frac{C_{p\alpha}V_\epsilon}{K_{T\epsilon}}\right). \end{aligned} \tag{2.18}$$

From this entire formulation, all the variables required to solve the system of equation except for the volume fraction differential $d\lambda$ are known. Using the work of Hayes [33], the differential is assumed to take the form:

$$\begin{cases} d\lambda = \frac{(G_\epsilon - G_\alpha)(1-\lambda)}{T}\frac{dt}{\tau} & dV < 0 \\ d\lambda = \frac{\lambda(G_\epsilon - G_\alpha)}{T}\frac{dt}{\tau} & dV \geq 0 \end{cases}$$

where, dt and τ are the time increment and the phase transition time, respectively.

The last bit of information required are the initial conditions, and the increment in dV and dU. Regarding the initial conditions, the pressure, specific volume, and temperature are assumed to be at $P_0 = 0$ GPa, $V_0 = 127.0123 \times 10^{-6}$ m^3/kg, and $T_0 = 300$ K, respectively. Given the Helmholtz free energy expressions in Equation 2.3 and the parameters in Table 2.5, the necessary Legendre transformations can be conducted to obtain the initial specific internal energy, and Gibbs free energy. Additionally, other necessary variables such as the specific heats can also be extracted from the Helmholtz free energy. Now that the initial conditions have been established, consider the increment in specific volume and internal energy.

The increment in specific volume is obtained from the strain increment given by ABAQUS/Explicit [30] where the volumetric strain is defined as $\Delta V/V_0 = \text{tr}(\boldsymbol{\varepsilon})$. The increment in energy must also account for irreversible work from plastic deformation and is given as [38]:

$$dU = -PdV + V_0 \bar{\tau} d\bar{\gamma}_p, \qquad \bar{\tau} = \sqrt{\frac{1}{2} S_{ij} S_{ij}}, \qquad d\bar{\gamma}_p = \sqrt{2 d\varepsilon^p_{ij} \varepsilon^p_{ij}}. \tag{2.19}$$

2.4.3 Iron parameters

To obtain the Johnson-Cook parameters, Y_0, B, n, and m, a sensitivity study was conducted. The initial values for each parameter were determined manually and assumed to be $Y_0 = 1.6$ GPa, $B = 3.4$ GPa, $n = 0.4$, and $m = 0.65$ as they provided a sufficient first-order match between simulated and experimental velocity profiles. For a more accurate calibration, a series of simulations were conducted to assess the sensitivity of peak transverse velocity to each variable. This was done by varying one variable while keeping the others constant at the manually determined initial values. The results of these simulations are displayed in Figures 2.5-2.8.

The peak velocities from these simulations were stored for each variable and compared to the experimental peak velocities as shown in Figure 2.9. By inspection, the variation of the peak velocity with respect to each variable is approximately linear within the current range thus, a linear fit is obtained between peak velocity and each individual parameter at each pressures. Next,

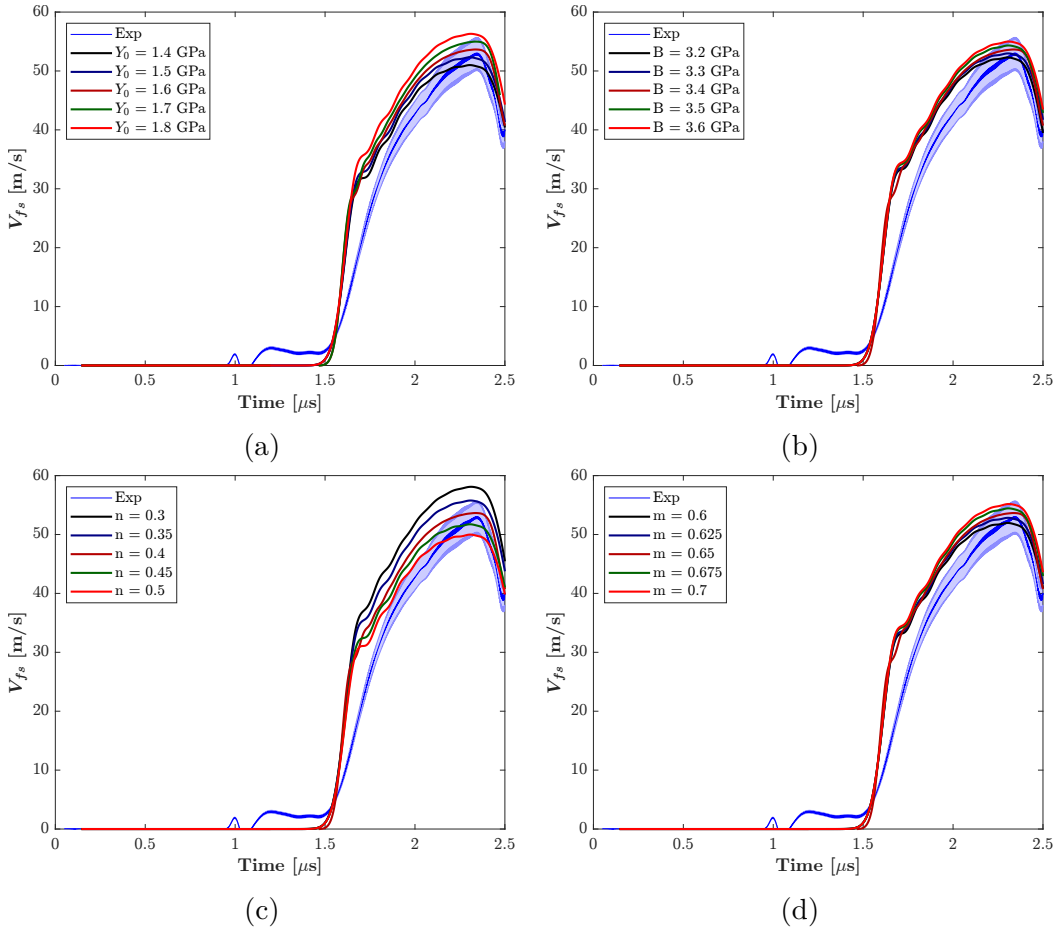

Figure 2.5: Transverse velocity from the sensitivity study for 15.8 GPa experiment for varying (a) Y_0, (b) B, (c) n, and (d) m. The shading within the experimental curve corresponds to the 5% uncertainty envelope.

the respective derivatives are evaluated and the sensitivities of peak velocity to each variable at each respective pressure were determined. This provides a matrix of derivatives that will be used to solve a minimization problem.

$$\underline{\underline{A}} = \begin{bmatrix} \frac{\Delta V}{\Delta Y_0}\Big|_{P=15} & \frac{\Delta V}{\Delta B}\Big|_{P=15} & \frac{\Delta V}{\Delta n}\Big|_{P=15} & \frac{\Delta V}{\Delta m}\Big|_{P=15} \\ \frac{\Delta V}{\Delta Y_0}\Big|_{P=21} & \frac{\Delta V}{\Delta B}\Big|_{P=21} & \frac{\Delta V}{\Delta n}\Big|_{P=21} & \frac{\Delta V}{\Delta m}\Big|_{P=21} \\ \frac{\Delta V}{\Delta Y_0}\Big|_{P=30} & \frac{\Delta V}{\Delta B}\Big|_{P=30} & \frac{\Delta V}{\Delta n}\Big|_{P=30} & \frac{\Delta V}{\Delta m}\Big|_{P=30} \\ \frac{\Delta V}{\Delta Y_0}\Big|_{P=42} & \frac{\Delta V}{\Delta B}\Big|_{P=42} & \frac{\Delta V}{\Delta n}\Big|_{P=42} & \frac{\Delta V}{\Delta m}\Big|_{P=42} \end{bmatrix} \tag{2.20}$$

Using the initial values for Y_0, B, n, and m, the values for the simulated peak velocities are known. Therefore, taking the difference between these initial peak velocities and experimental peak velocities, we define the vector

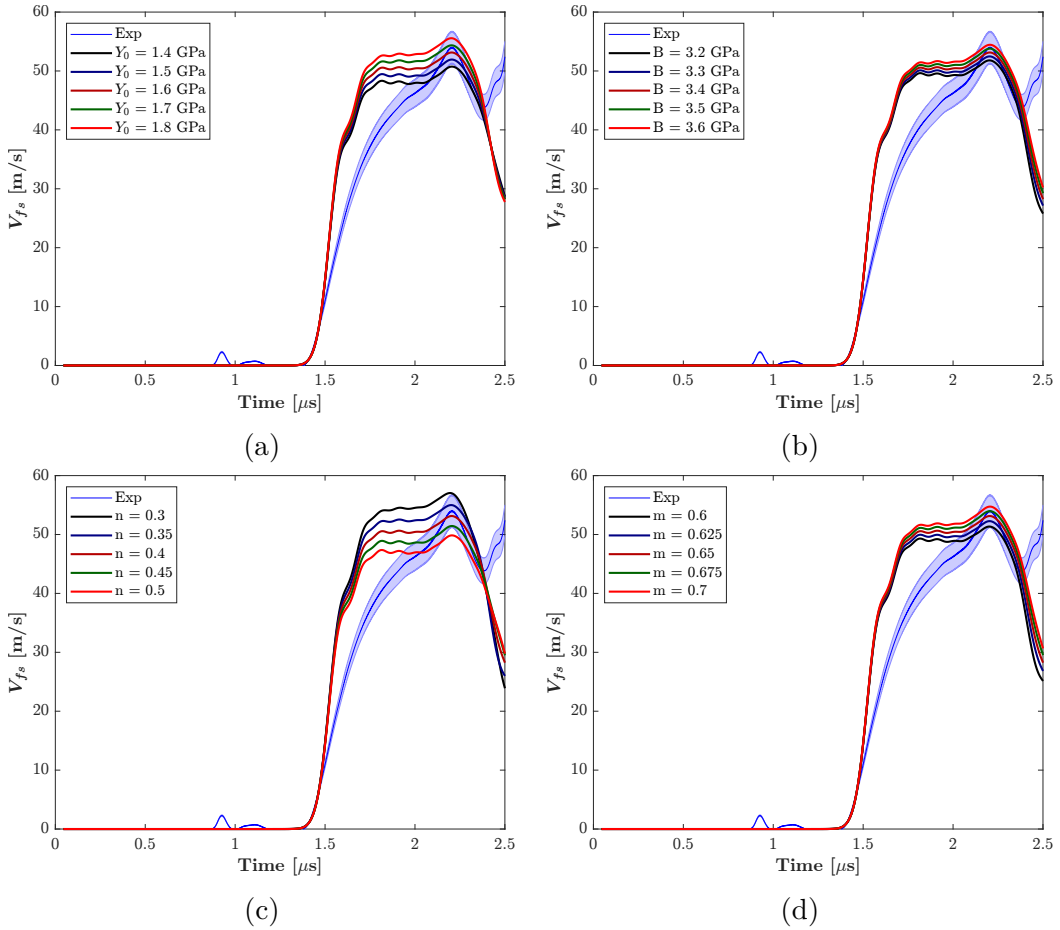

Figure 2.6: Transverse velocity from the sensitivity study for 21.5 GPa experiment for varying (a) Y_0, (b) B, (c) n, and (d) m. The shading within the experimental curve corresponds to the 5% uncertainty envelope.

$$\underline{\Delta V_t} = \begin{bmatrix} \Delta V_{15} \\ \Delta V_{21} \\ \Delta V_{30} \\ \Delta V_{42} \end{bmatrix}. \tag{2.21}$$

This vector corresponds to the desirable total change in velocity by varying the JC parameters. Therefore, the goal is to determine the change in these JC parameters which will allow us to obtain this velocity change from initial values. This can be formulated as a linear system

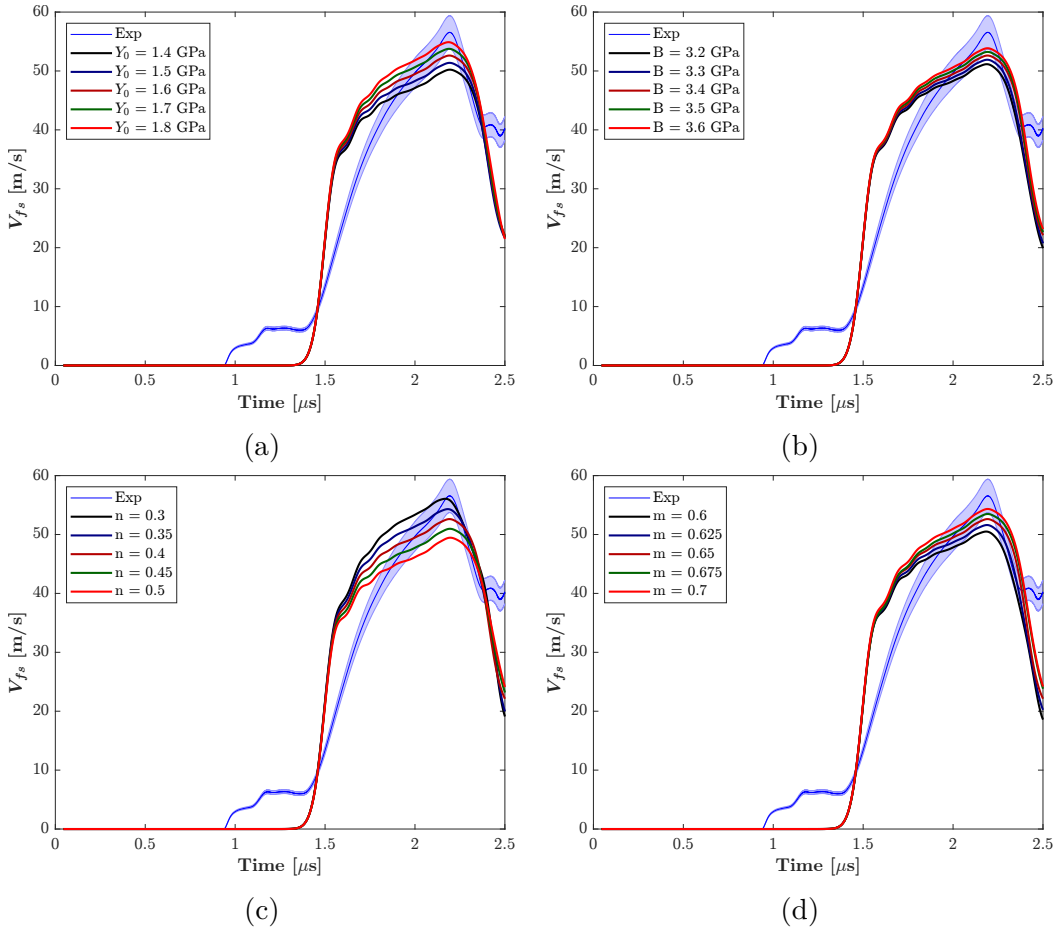

Figure 2.7: Transverse velocity from the sensitivity study for 30.2 GPa experiment for varying (a) Y_0, (b) B, (c) n, and (d) m. The shading within the experimental curve corresponds to the 5% uncertainty envelope.

$$\underline{\underline{A}} \cdot \underline{\Delta x} = \underline{\Delta V_t}, \qquad \text{where } \underline{\Delta x} = \begin{bmatrix} \Delta Y_0 \\ \Delta B \\ \Delta n \\ \Delta m \end{bmatrix}. \tag{2.22}$$

Since A is an invertible matrix and has full rank, there is an optimal solution for this linear system however it leads to nonphysical JC parameters and constraints need to be imposed. Therefore, this can be converted to a linear least squares problem with the objective

$$f = \min_{\Delta x} \left\| \underline{\underline{A}} \cdot \underline{\Delta x} - \underline{\Delta V_t} \right\|_{L2}^2 \tag{2.23}$$

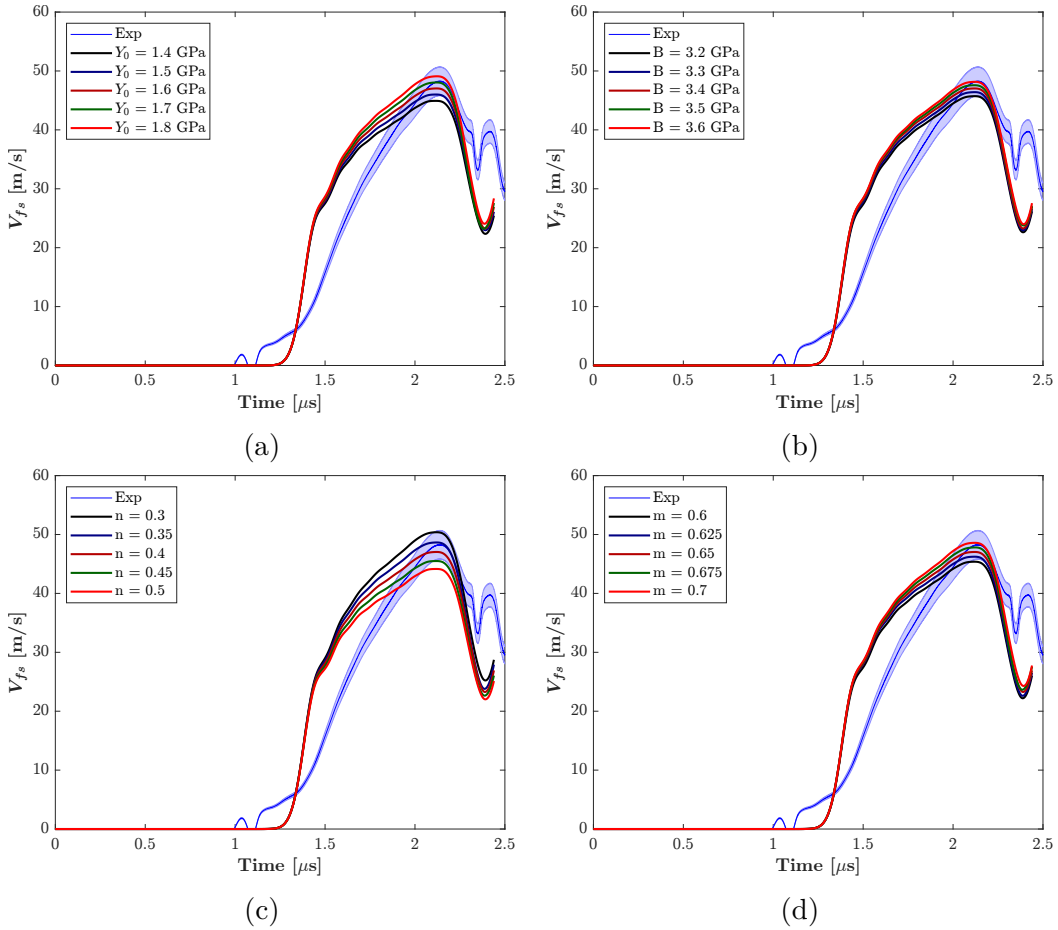

Figure 2.8: Transverse velocity from the sensitivity study for 42 GPa experiment for varying (a) Y_0, (b) B, (c) n, and (d) m. The shading within the experimental curve corresponds to the 5% uncertainty envelope.

subjected to the constraints

$$\begin{cases} 0.5 \text{ GPa} \leq Y_0 \leq 2 \text{ GPa} \\ 2.4 \text{ GPa} \leq B \leq 5 \text{ GPa} \\ 0 \leq n \leq 1 \\ 0.1 \leq m \leq 1.5 \end{cases}.$$

The optimal parameters for the ϵ-iron hardening model that satisfy the imposed constraints are

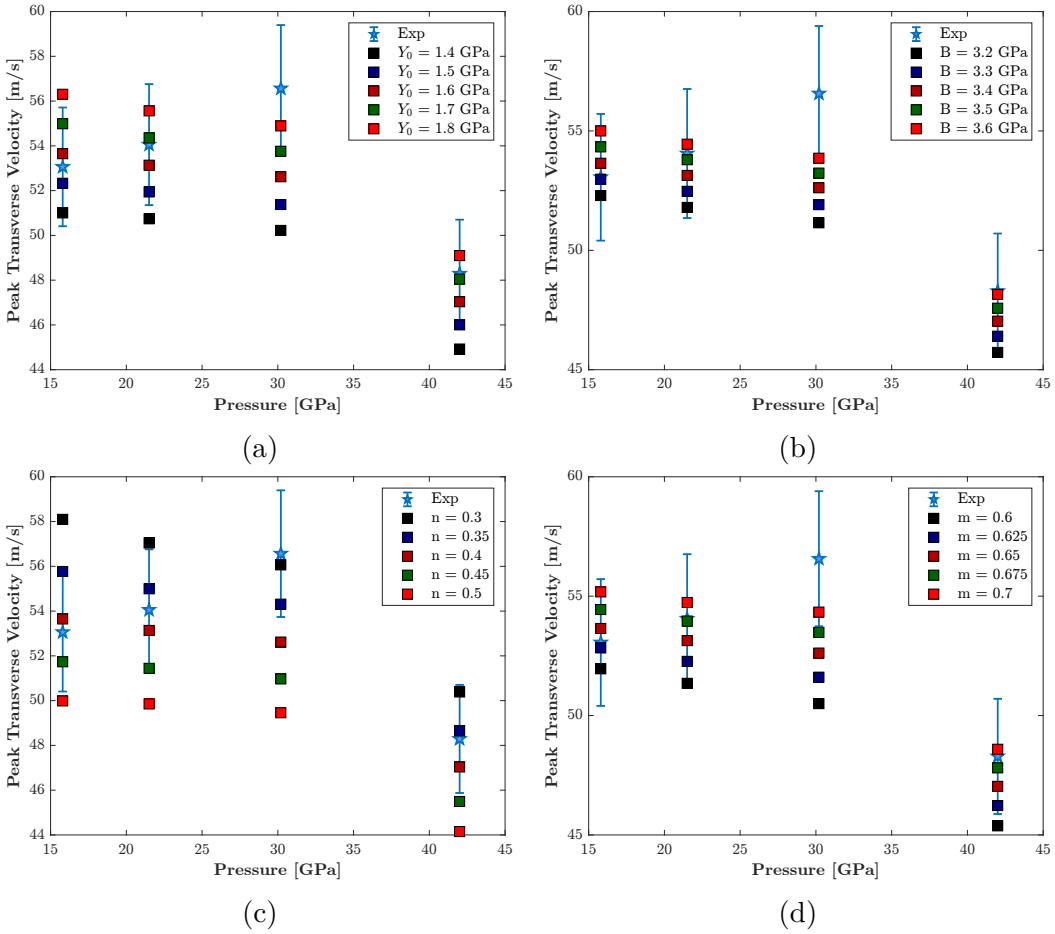

Figure 2.9: Comparison of peak transverse velocities and their sensitivities to (a) Y_0, (b) B, (c) n, and (d) m. The error bars on the experimental data corresponds to the 5% uncertainty envelope.

Fitted Parameters				Literature [8]	
$\mathbf{Y_0}$ [GPa]	$\mathbf{B}$ [GPa]	$\mathbf{n}$	$\mathbf{m}$	$\frac{\mathbf{Y'_P}}{\mathbf{Y_0}}$ [GPa^{-1}]	$\frac{\mathbf{G'_T}}{\mathbf{G_0}}$ [kK^{-1}]
2.0	2.4	0.73	1.08	0.0246	1.08

Figure 2.10 compares the peak velocity from the final simulations with experimental data.

To close the discussion on simulation methodology, the numerical errors need to be considered. Simulations were conducted on elements that were 10 μm along the normal shock propagation direction and the time steps were $\Delta t = 10$

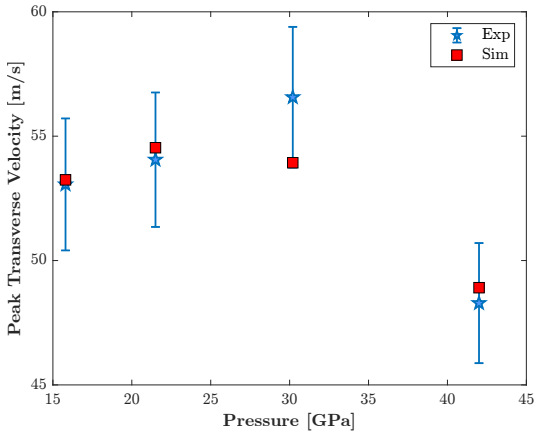

Figure 2.10: Final experimental and simulated peak transverse velocities plotted against pressure. The error bars correspond to the 5% uncertainty envelope.

ps. It was shown in [39] that spatial resolution below 20 μm element thickness did not offer any improvement in accuracy. Therefore, the numerical error associated with our simulations are assumed to be negligible. At last, we compare the final simulated velocity profiles with the experimental velocity. Since, four experiments were conducted and four parameters were fit, there is a unique solution to this linear system. The solution to the linear system should identically have no error. However, this would lead to nonphysical optimal parameters. Therefore, constraints were imposed on the parameters Y_0 and others. A linear least squares solution with constraints was solved to minimize the L2 norm of the true velocity and obtained peak velocity from simulations. The peaks of the resulting velocity profiles with these optimized yield function parameters were within 5% uncertainty range from the experimental measurements. This is shown in Figure 2.10 where the error bars on the experimental data corresponds to the 5% uncertainty regime. Thus, we claim the strength measurements obtained from simulations are within 5% uncertainty.

2.5 Discussion

The experimentally measured normal and transverse velocity profiles along with the simulated profiles at each corresponding pressure are displayed in Figure 2.11. Unlike the normal velocity profile, the transverse profiles primarily depict the strength behavior of iron. We note the imposed transverse velocities in these experiments ranged from 100-110 m/s to ensure a shear strain-rate on the order of 10^5 s^{-1} within the iron sample. The measured

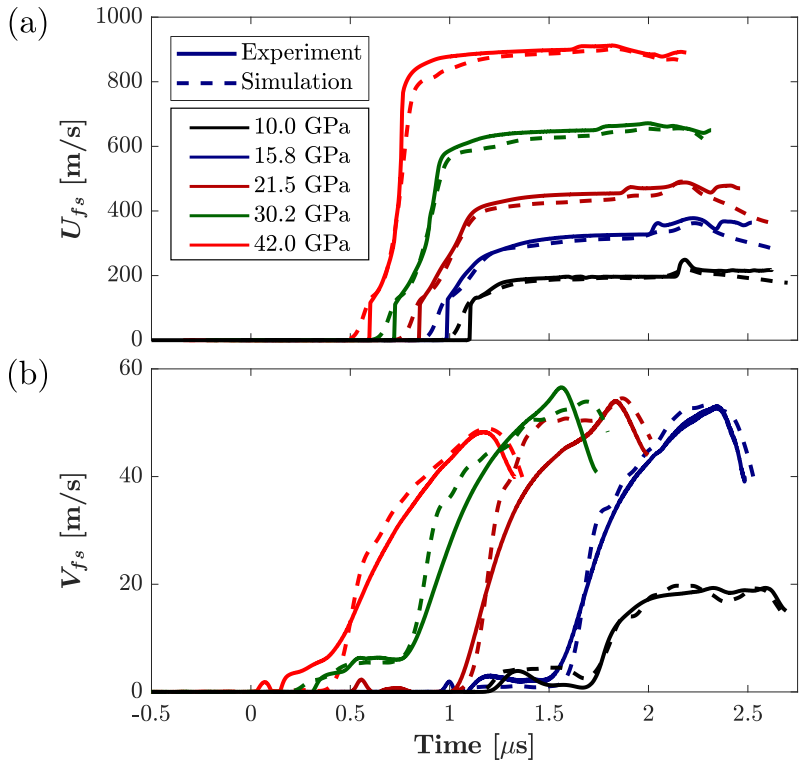

Figure 2.11: Plot of (a) normal and (b) transverse free surface velocity profiles at varying pressures for pure iron. The solid lines correspond to experimental records and the dashed curves correspond to simulated profiles. Both the normal and transverse velocity profiles (except for the 15 GPa curves) have been shifted for clarity in visualizing the results.

transverse velocities are below the imposed velocity at the impactor/target interface indicating dispersion of the shear wave due to plasticity in the iron sample. As the longitudinal wave traverses through the sample, at high pressures, the material yields. Therefore, the shear wave traversing through this yielded material will disperse [21]. For anvil materials stronger than iron, e.g. tungsten carbide, the maximum dissipation of the shear wave occurs within the sandwiched sample. We employ the von Mises yield criterion where the yield condition for shear-normal coupling is $\frac{3}{4}s_{xx}^2 + \tau_{xy}^2 = \frac{1}{3}Y^2$ [21] with Y as the yield stress, τ_{xy} as the shear stress and s_{xx} as the normal component of the deviatoric stress tensor. Although the longitudinal wave is sufficient to yield the material, the arrival of the shear wave increases τ_{xy} while decreasing s_{xx} to ensure the material stays on the yield surface. If the shear wave arrives at an amplitude of $\tau_{xy} = Y/\sqrt{3}$, the deviatoric stress vanishes and the shear stress provides a direct measurement of the yield behavior of the material. Therefore, the transverse velocity profiles correlate to the strength of the iron

in its respective phase.

From initial inspection, we observe a significant increase in transverse velocity at 15.8 GPa compared to 10 GPa. This indicates ϵ-iron having a much higher strength than the ambient α-iron. However, we cannot discern strength directly from the transverse velocity profile as the peak velocity at higher pressures are similar to the peak at 15.8 GPa. The primary reason for this phenomenon is due to increased plasticity in anvils at higher pressures resulting in larger shear wave dispersion at the rear anvil. Therefore, the transverse velocities themselves are insufficient to conclude strength behavior of iron at high pressures highlighting the importance of forward modeling to extract the stress-strain behavior. The dashed curves in Figure 2.11 corresponds to the simulated velocity profiles.

By constraining the shear strain-rate at $\sim 10^5$ s^{-1} through varying impact angles, the complete pressure dependent strength and flow behavior of ϵ-iron was extracted from the simulations for a full range of shear strains, Figure 2.12a. From our data we make two main conclusions, (1) the strength of iron in its ϵ-phase is more than double that of the α-phase, and (2) the dynamic strength of ϵ-iron is an order of magnitude lower than previously observed.

The yield strength ($Y = \sqrt{3}\tau$) at $\gamma = 0.1$ of iron at 15.8 GPa of pressure ($\sim$ 78% ϵ-phase based of the EOS model [14]) is 2.69$\pm$0.13 GPa. In contrast, at 10 GPa of pressure, the yield strength of α-iron is 1.04$\pm$0.05 GPa which is within reasonable limits when compared to strength data observed from Kolsky bar experiments [25, 31] further validating our experimental technique. A reason for the increased strength lies within the partially higher yield strength scaling due to pressure dependent shear modulus in the ϵ-phase ($\frac{1}{G_0}\frac{\partial G}{\partial P} = 0.0246$ GPa^{-1}) compared to α-phase ($\frac{1}{G_0}\frac{\partial G}{\partial P} = 0.0221$ GPa^{-1}) [40]. The ϵ-phase also exists at higher pressures so the scaling would result in higher strength in the HCP phase. While BCC materials generally show higher strength at these strain-rates than HCP materials [41, 42], the strength increase may be explained by the transformation strain required to change the crystal structure from BCC to HCP [12, 42] and also the microstructural evolution during this phase transition. At approximately 13 GPa of pressure, iron does not entirely transform into its ϵ-phase but rather a mixed phase region is said to exist between 13-22 GPa [14, 31]. According to recent experimental observations [43] and molecular dynamics simulations [44], the evolution

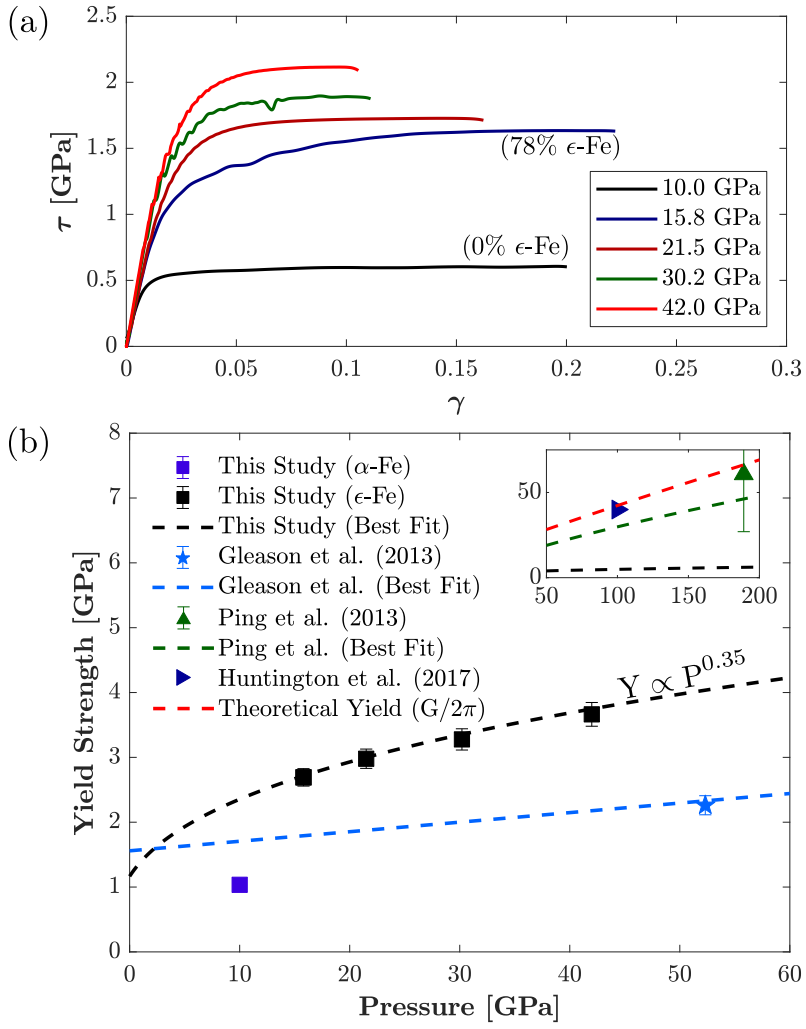

Figure 2.12: Plots of (a) shear stress vs shear strain of ϵ-iron for varying pressures and (b) comparison of von Mises yield strength at 10% shear strain with data from literature. The best fit curve (black dashed line) follows a power law relation ($Y \propto P^{0.35}$) compared to the linear relation obtained from static experiments by Gleason and Mao [8]. The main plot compares our data with other static experiments and the inset contains data from other dynamic experimental studies alongside our best fit curve. The dashed red curve corresponds to the theoretical yield strength (G/2π) obtained from shear modulus data from [8].

of the ϵ-phase begins at grain boundaries and these HCP clusters evolve into needle like colonies which act as sub-grains within the original grains. Shock experiments on single crystal iron [45] also indicate the formation of these nanocrystalline structures based on the symmetry-related variants of the new HCP phase from the parent BCC phase. In addition to these nanocrystals, twins form within the material to ensure kinematic compatibility between the two phases [46], but also due to the longitudinal wave during phase transformation [47] and the shear loading [25]. Given our loading conditions, it is possible that deformation twinning due to the transverse wave persists within our sample since the HCP phase favors twinning over slip as a deformation mechanism. Ultimately, the formation of HCP clusters and twins tend to occur during the transition in addition to the nucleation of screw dislocations, dislocation loops, stacking faults, and vacancies [44]. These twin boundaries and nanocrystalline grain boundaries, through the dynamic Hall-Petch effect, act as obstacles for dislocation motion therefore increasing dislocation pileup and inherently increasing the yield strength.

The strength of ϵ-iron, at 10% shear strain, determined in the current study differs significantly from the previously reported values, Figure 2.12b. Ping et al. [19] have indirectly determined the yield strength of ϵ-iron up to pressures of 560 GPa from temperature measurements via laser shock experiments coupled with EXAFS data. The authors extrapolate their data and claim a yield strength of $\sim$20 GPa and $\sim$30 GPa at pressures of 50 GPa and 100 GPa, respectively. Huntington et al. [20] arrived at a similar conclusion as Ping et al. and observed a flow strength of $\sim$40 GPa at 100 GPa of pressure by observing the growth of Rayleigh-Taylor instabilities. These strength reportings seem rather unexpected as they are on the cusp of the theoretical yield limit assuming the limit is a function of the pressure dependent shear modulus and given by $Y \propto G(P,T)/2\pi$. By extrapolating our data to higher pressures we claim these reporting to be an order of magnitude higher than the 4.3 and 5.1 GPa yield strength we observe at pressures of 50 GPa and 100 GPa, respectively. While this variability can be attributed to different grain sizes, strain-rates, and heat treatment, these are not sufficient to explain a discrepancy of this magnitude. For example, recent MD simulations on nano-crystalline iron at strain-rates of 10^9 s^{-1} shows a shear stress of 2.5 GPa (yield stress of 4.3 GPa) at 30 GPa of pressure [44]. Additionally, Prime et al. [48] recently conducted high strain-rate Richtmyer-Meshkov instability (RMI) experiments on

tantalum and compared their results with Z-machine data [49]. The authors concluded pressure effects on strength are more significant than strain-rate effects in these extreme conditions. Hence, the main difference occurs due to experimental technique and the interpretation of the measurements. PSPI experiments are designed to probe the stress versus strain behavior and hence the strength of a material whereas the laser shock experiments by Ping et al. [19] were designed to understand density, and temperature of compressed iron. This indirect determination of strength from temperature explains the high strength, on the order of theoretical yield strength (G/2π), and large uncertainties in their results. Smith et al. [2] note the strength data from static experiments [8, 17] in pressure regimes below 300 GPa were required to match the 300 K isotherm when converting their $\sigma_{xx} - \rho$ data to an isentropic $P - \rho$ curve. The reported strength from static experiments is on the same order as our results. However, our data does indicate an increased strength compared to Gleason and Mao [8] because of strain-rate dependence of ϵ-iron. Diamond anvil cell experiments are typically conducted at compressive strain-rates of $\sim 10^{-5}$ s^{-1} which is far lower than our experiments conducted at compressive strain-rates of $\sim 10^{5}$ s^{-1}.

2.6 Conclusion

In summary, PSPI experiments were conducted to characterize the pressure dependent plasticity and strength behavior of iron in its high pressure HCP ϵ-phase. From free surface velocity measurements coupled with modeling, we extract the complete stress-strain curve for ϵ-iron for the first time and observe a substantial increase in the yield strength of the phase transformed material compared to its ambient α-phase. Additionally, we find the dynamic strength of ϵ-iron to be an order of magnitude lower than previous literature. Current work relies on static literature data for shear modulus scaling with pressure however, future experiments are planned to dynamically characterize pressure dependent material properties for accurate construction of EOS and flow strength scaling. These strength and material parameters will be used to develop a sophisticated kinetics-based model for the phase transformation of iron. Our experiments on ϵ-iron offer the potential to significantly extend our knowledge of the deformation behavior of earth's inner core and construct a realistic model of the inner cores of rocky planets and meteorite impacts.

References

[1] W. B. Hubbard, W. J. Nellis, A. C. Mitchell, N. C. Holmes, S. S. Limaye, and P. C. McCandless, "Interior structure of Neptune: Comparison with Uranus," Science **253**, 648–651 (1991).

[2] R. F. Smith, D. E. Fratanduono, D. G. Braun, T. S. Duffy, J. K. Wicks, P. M. Celliers, S. J. Ali, A. Fernandez-Pañella, R. G. Kraus, D. C. Swift, and et al., "Equation of state of iron under core conditions of large rocky exoplanets," Nature Astronomy **2**, 452–458 (2018).

[3] A. V. Jain and M. E. Lipschutz, "Implications of shock effects in iron meteorites," Nature **220**, 139–143 (1968).

[4] K. Terada, T. Morota, and M. Kato, "Asteroid shower on the Earth-Moon system immediately before the cryogenian period revealed by KAGUYA," Nature Communications **11**, 3453 (2020).

[5] A. Cameron, "The origin of the Moon and the single impact hypothesis V," Icarus **126**, 126–137 (1997).

[6] N. Hosono, S.-I. Karato, J. Makino, and T. R. Saitoh, "Terrestrial magma ocean origin of the Moon," Nature Geoscience **12**, 418–423 (2019).

[7] D. Batani, A. Morelli, M. Tomasini, A. Benuzzi-Mounaix, F. Philippe, M. Koenig, B. Marchet, I. Masclet, M. Rabec, C. Reverdin, R. Cauble, P. Celliers, G. Collins, L. Da Silva, T. Hall, M. Moret, B. Sacchi, P. Baclet, and B. Cathala, "Equation of state data for iron at pressures beyond 10 mbar," Physical Review Letters **88**, 235502 (2002).

[8] A. E. Gleason and W. L. Mao, "Strength of iron at core pressures and evidence for a weak Earth's inner core," Nature Geoscience **6**, 571–574 (2013).

[9] D. Bancroft, E. L. Peterson, and S. Minshall, "Polymorphism of iron at high pressure," Journal of Applied Physics **27**, 291–298 (1956).

[10] J. C. Jamieson and A. W. Lawson, "X-ray diffraction studies in the 100 kilobar pressure range," Journal of Applied Physics **33**, 776–780 (1962).

[11] D. H. Kalantar, J. F. Belak, G. W. Collins, J. D. Colvin, H. M. Davies, J. H. Eggert, T. C. Germann, J. Hawreliak, B. L. Holian, K. Kadau, P. S. Lomdahl, H. E. Lorenzana, M. A. Meyers, K. Rosolankova, M. S. Schneider, J. Sheppard, J. S. Stölken, and J. S. Wark, "Direct observation of the $\alpha-\epsilon$ transition in shock-compressed iron via nanosecond x-ray diffraction," Physical Review Letters **95**, 075502 (2005).

[12] G. Krauss, "Martensite in steel: strength and structure," Materials Science and Engineering: A **273-275**, 40–57 (1999).

[13] S. Harjo, N. Tsuchida, J. Abe, and W. Gong, "Martensite phase stress and the strengthening mechanism in TRIP steel by neutron diffraction," Scientific Reports **7**, 15149 (2017).

[14] J. C. Boettger and D. C. Wallace, "Metastability and dynamics of the shock-induced phase transition in iron," Physical Review B **55**, 2840–2849 (1997).

[15] B. Yaakobi, T. R. Boehly, D. D. Meyerhofer, T. J. B. Collins, B. A. Remington, P. G. Allen, S. M. Pollaine, H. E. Lorenzana, and J. H. Eggert, "Exafs measurement of iron bcc-to-hcp phase transformation in nanosecond-laser shocks," Physical Review Letters **95**, 075501 (2005).

[16] K. J. Caspersen, A. Lew, M. Ortiz, and E. A. Carter, "Importance of shear in the bcc-to-hcp transformation in iron," Physical Review Letters **93**, 115501 (2004).

[17] R. J. Hemley, H. K. Mao, G. Shen, J. Badro, M. Hanfland, and D. Hausermann, "X-ray imaging of stress and strain of diamond, iron, and tungsten at megabar pressures," Science **276**, 1242–1245 (1997).

[18] A. Singh, A. Jain, H. Liermann, and S. Saxena, "Strength of iron under pressure up to 55gpa from x-ray diffraction line-width analysis," Journal of Physics and Chemistry of Solids **67**, 2197–2202 (2006).

[19] Y. Ping, F. Coppari, D. G. Hicks, B. Yaakobi, D. E. Fratanduono, S. Hamel, J. H. Eggert, J. R. Rygg, R. F. Smith, D. C. Swift, D. G. Braun, T. R. Boehly, and G. W. Collins, "Solid iron compressed up to 560 gpa," Physical Review Letters **111**, 065501 (2013).

[20] C. M. Huntington, J. L. Belof, K. J. M. Blobaum, R. M. Cavallo, N. B. Kostinski, B. R. Maddox, H.-S. Park, C. Plechaty, S. T. Prisbrey, R. Rudd, and et al., "Investigating iron material strength up to 1 mbar using rayleigh-taylor growth measurements," AIP Conference Proceedings, 10.1063/1.4971670 (2017).

[21] C. Kettenbeil, Z. Lovinger, S. Ravindran, M. Mello, and G. Ravichandran, "Pressure-shear plate impact experiments at high pressures," Journal of Dynamic Behavior of Materials, 489–501 (2020).

[22] R. Clifton and R. Klopp, "Pressure shear plate impact testing," in, Vol. 8 (Metals Handbook, 1985), pp. 230–239.

[23] C. Kettenbeil, M. Mello, M. Bischann, and G. Ravichandran, "Heterodyne transverse velocimetry for pressure-shear plate impact experiments," Journal of Applied Physics **123**, 125902 (2018).

[24] O. T. Strand, D. R. Goosman, C. Martinez, T. L. Whitworth, and W. W. Kuhlow, "Compact system for high-speed velocimetry using heterodyne techniques," Review of Scientific Instruments **77**, 083108 (2006).

[25] D. Rittel, G. Ravichandran, and A. Venkert, "The mechanical response of pure iron at high strain rates under dominant shear," Materials Science and Engineering: A **432**, 191–201 (2006).

[26] S. Ravindran, V. Gandhi, Z. Lovinger, M. Mello, and G. Ravichandran, "Dynamic strength of copper at high pressures using pressure shear plate experiments," Dynamic Behavior of Materials, 248–261 (2021).

[27] J. A. Hawreliak, B. El-Dasher, H. Lorenzana, G. Kimminau, A. Higginbotham, B. Nagler, S. M. Vinko, W. J. Murphy, T. Whitcher, J. S. Wark, S. Rothman, and N. Park, "In situ x-ray diffraction measurements of the c/a ratio in the high-pressure ϵ phase of shock-compressed polycrystalline iron," Physical Review B **83**, 144114 (2011).

[28] C. Kettenbeil, "Dynamic strength of silica glasses at high pressures and strain rates," PhD thesis (California Institute of Technology, 2019).

[29] D. Dolan, "Accuracy and precision in photonic doppler velocimetry," Review of Scientific Instruments, 053905 (2010).

[30] Hibbitt, Karlsson, and Sorenson, *Abaqus/explicit: user's manual, version 6.2* (Hibbitt, Karlsson and Sorenson Inc., United States, 2001).

[31] A. Sadjadpour, D. Rittel, G. Ravichandran, and K. Bhattacharya, "A model coupling plasticity and phase transformation with application to dynamic shear deformation of iron," Mechanics of Materials **80**, 255–263 (2015).

[32] D. J. Steinberg, S. G. Cochran, and M. W. Guinan, "A constitutive model for metals applicable at high-strain rate," Journal of Applied Physics **51**, 1498–1504 (1980).

[33] D. B. Hayes, "Wave propagation in a condensed medium with n transforming phases: application to solid-i-solid-ii-liquid bismuth," Journal of Applied Physics **46**, 3438–3443 (1975).

[34] D. Andrews, "Calculation of mixed phases in continuum mechanics," Journal of Computational Physics **7**, 310–326 (1971).

[35] J. L. Brown, M. B. Prime, N. R. Barton, D. J. Luscher, L. Burakovsky, and D. Orlikowski, "Experimental evaluation of shear modulus scaling of dynamic strength at extreme pressures," Journal of Applied Physics **128**, 045901 (2020).

[36] J. Jung, "A note on the influence of hydrostatic pressure on dislocations," Philosophical Magazine A **43**, 1057–1061 (1981).

[37] H.-K. Mao, J. Shu, G. Shen, R. J. Hemley, B. Li, and A. K. Singh, "Elasticity and rheology of iron above 220 gpa and the nature of the earth's inner core," Nature **396**, 741–743 (1998).

[38] S. Grunschel, "Pressure-shear plate impact experiments on high-purity aluminum at temperatures approaching melt," PhD thesis (Brown University, 2009).

[39] M. B. Rauls and G. Ravichandran, "Structure of shock waves in particulate composites," Journal of Applied Physics **127**, 065902 (2020).

[40] M. Guinan and D. Steinberg, "Pressure and temperature derivatives of the isotropic polycrystalline shear modulus for 65 elements," Journal of Physics and Chemistry of Solids **35**, 1501–1512 (1974).

[41] R. W. Armstrong and S. M. Walley, "High strain rate properties of metals and alloys," International Materials Reviews **53**, 105–128 (2008).

[42] G. T. (Rusty) Gray, "High-strain-rate deformation: mechanical behavior and deformation substructures induced," Annual Review of Materials Research **42**, 285–303 (2012).

[43] S. J. Wang, M. L. Sui, Y. T. Chen, Q. H. Lu, E. Ma, X. Y. Pei, Q. Z. Li, and H. B. Hu, "Microstructural fingerprints of phase transitions in shock-loaded iron," Scientific Reports **3**, 1–6 (2013).

[44] H.-T. Luu, R. J. Ravelo, M. Rudolph, E. M. Bringa, T. C. Germann, D. Rafaja, and N. Gunkelmann, "Shock-induced plasticity in nanocrystalline iron: large-scale molecular dynamics simulations," Physical Review B **102**, 020102 (2020).

[45] J. A. Hawreliak, D. H. Kalantar, J. S. Stölken, B. A. Remington, H. E. Lorenzana, and J. S. Wark, "High-pressure nanocrystalline structure of a shock-compressed single crystal of iron," Physical Review B **78**, 220101 (2008).

[46] K. Bhattacharya, *Microstructure of martensite: why it forms and how it gives rise to the shape-memory effect?* (Oxford University Press, 2012).

[47] N. Gunkelmann, D. R. Tramontina, E. M. Bringa, and H. M. Urbassek, "Morphological changes in polycrystalline fe after compression and release," Journal of Applied Physics **117**, 085901 (2015).

[48] M. B. Prime, W. T. Buttler, S. J. Fensin, D. R. Jones, J. L. Brown, R. S. King, R. Manzanares, D. T. Martinez, J. I. Martinez, J. R. Payton, and D. W. Schmidt, "Tantalum strength at extreme strain rates from impact-driven Richtmyer-Meshkov instabilities," Physical Review E **100**, 053002 (2019).

[49] J. L. Brown, C. S. Alexander, J. R. Asay, T. J. Vogler, D. H. Dolan, and J. L. Belof, "Flow strength of tantalum under ramp compression to 250 GPa," Journal of Applied Physics **115**, 043530 (2014).

Chapter 3

REAL-TIME CHARACTERIZATION OF DISLOCATION SLIP AND TWINNING OF SHOCK COMPRESSED MOLYBDENUM SINGLE CRYSTALS

V. Gandhi, S. Ravindran, A. Joshi, and G. Ravichandran, "Real-time characterization of dislocation slip and twinning of shock compressed molybdenum single crystals," (Under Review) (2023)

Contributions: V.G. performed the experiments, prepared the experimental data, developed the simulation methodology, and wrote the manuscript.

Abstract

Characterizing the fundamental micromechanisms activated during plastic deformation is critical to explain the macroscopic shock response of materials and develop accurate material models. In this letter, we investigate the orientation dependence, and the mediated slip and twin systems on [1 0 0] and [1 1 1] BCC molybdenum single crystals shock compressed up to 18 GPa with real-time Laue x-ray diffraction measurements. We report that dislocation slip along the $\{1\,1\,0\}\langle 1\,1\,1\rangle$ and $\{1\,1\,2\}\langle 1\,1\,1\rangle$ systems are the governing deformation mechanism during compression with negligible anisotropy observed at the Hugoniot state. For the first time, we provide real-time evidence that molybdenum undergoes deformation twinning along $\{1\,1\,\overline{2}\}\langle 1\,1\,1\rangle$ during shock release.

3.1 Introduction

When a metal undergoes shock compression beyond its Hugoniot elastic limit (HEL), the plastic deformation is typically governed by generation and motion of dislocations [1]. Generally, establishing the active atomistic mechanisms during inelastic loading is difficult but is critical to explain the macroscopic response of materials for shock applications involving high velocity impacts

such as planetary impacts [2], aircraft collisions [3], spacecraft shielding [4], and even armor and anti-armor applications [5]. The high strain-rates, temperatures, and pressures experienced under shock compression may activate different slip or twin systems than under quasi-static loading and thus, requires real time characterization of the atomistics. However, most studies to date focus on post-mortem analysis of recovered sample which may not reflect the material behavior during the passage of the shock wave. To that end, recent efforts at the Dynamic Compression Sector (DCS) at the Advanced Photon Source (APS) [6] has enabled real-time x-ray diffraction (XRD) measurements in shock compression experiments and has been critical in understanding phenomena such as phase transformations [7, 8], and equations of state (EOS) [9–11].

Because of its high temperature specific strength, creep resistance, and ductility [12], body-centered cubic (BCC) refractory metals, such as molybdenum (Mo), and their alloys have significant technological implications motivating studying their high-strain rate material response. Plasticity in BCC metals is governed by dislocation slip along the [1 1 1] direction [13] and is mediated by various factors such as interactions of defects with grain boundaries, the influence of pre-existing defects, and crystal structure [14]. Here, we focus on molybdenum single crystals as a representative refractory BCC metal since single crystals help preclude the effect of grain boundaries on the deformation response and provide key insights concerning the role of crystal orientation.

Considerable work has been conducted to understand the fundamental deformation mechanisms of molybdenum in the quasi-static regime and it has been shown that its deformation is governed by the mobility of screw dislocations along the $\{1\,1\,0\}\langle 1\,1\,1\rangle$ and $\{1\,1\,2\}\langle 1\,1\,1\rangle$ slip systems. At low temperatures, the deformation of molybdenum is governed by thermally activated kink pairs and kink pair migration of screw dislocations along $\{1\,1\,0\}$ slip planes [15–17] while at higher temperatures, the deformation is governed by cross slip along $\{1\,1\,2\}$ planes [15]. Molybdenum also displays slip and yield tension-compression asymmetry due to the different Peirels stress in the twinning and anti-twinning [16, 18–21] direction, where the twinning is more prevalent at lower temperatures [18, 22]. In addition to slip, deformation twinning in the $\{1\,1\,2\}$ planes along the $\langle 1\,1\,1\rangle$ direction [23, 24] has been observed from post-mortem analysis of molybdenum undergoing shock compression (high strain-

rate) or low temperature deformation. It was shown that the volume fraction of twinning increases with pressure [24] while homogeneous distribution of initial dislocations from pre-straining prior to shock compression suppressed twin formation [23]. Regardless, further experiments are required to understand these deformation mechanisms.

Polycrystalline Mo has been studied over a wide range of high pressures (up to 1 TPa) using diamond anvil cell (DAC) [25], plate impact [26, 27], and laser ramp compression [28] experiments. However, limited plate impact experimental studies have been performed on Mo single crystals [29–33]. Studies by Mandal et al. [30, 31] at low normal stresses (12.5 GPa) and Oniyama et al. [32] at higher pressures (up to 110 GPa) both report strong orientation dependence on the Hugoniot elastic limit (HEL) [30–32]. The [1 1 1] orientation was shown to exhibit the highest elastic amplitude which increases proportionally to the impact stress [32] while the behavior along [1 0 0] and [1 1 0] were comparable. Additionally, the authors observed attenuation of the elastic precursor as a function of time and propagation distance hypothesizing a change in active slip systems during this transition [31]. To explore the fundamental mechanisms governing this observed anisotropy, Mandal et al. [30, 31] performed complimentary crystal plasticity simulations but suggested *in-situ* experiments to be performed.

In this letter, we explore the underlying microstructural reasons for the anisotropy of HEL, and the governing plastic deformation mechanisms at the Hugoniot (steady) shock state and during release using plate impact experiments coupled with dynamic *in-situ* x-ray diffraction (XRD). The experimental observations are quantified using complimentary XRD simulations for extracting the lattice strains and stresses using which the active slip and twin deformation mechanisms are characterized.

3.2 Experimental methods

Plate impact experiments were conducted on high purity (99.99%) molybdenum single crystals oriented along the [1 0 0] and [1 1 1] directions at DCS. The ambient properties of the single crystals are displayed in Table 3.1. The material was procured from Accumet Materials Co. (Ossining, New York) as a 20 mm diameter cylindrical stock and powder diffraction was conducted at Caltech to quantify the misalignment of the crystallographic orientation. If the

misalignment exceeded 2°, the stock was cut into cylindrical discs at an angle to correct the misorientation. The Mo stock was cut to discs after which they were lapped flat and polished on one surface for *in-situ* XRD measurements.

A front surface impact configuration using polycarbonate window and reflection geometry XRD, was implemented for the plate impact experiments at DCS (Figure 3.1a). Here, a $2.5 - 4$ mm thick Molybdenum single crystal is impacted onto a ~ 1.5 mm polycarbonate window target at velocities ranging from $1800 - 2800$ m/s corresponding to elastic normal stresses of $8 - 19$ GPa. The polycarbonate window limits the achievable stresses in the experiment to below 22 GPa due to the x-ray transparency issues at higher pressures. Regardless, this configuration was implemented rather than using the molybdenum as a target with a window attached to its rear because the high impedance of molybdenum requires a high impedance window such as c-cut sapphire. In addition, the thickness of the sapphire window required to hold the pressure would result in x-rays being fully absorbed by the window at the experimental incidence angle.

Table 3.1: Material properties of single crystal molybdenum [32]

Orientation	ρ [**kg/m**^{3}]	C_L [**m/s**]	C_s [**m/s**]	a_0 [Å]	V_c [Å^3]
[1 0 0]		6836 ± 44	3300 ± 14		
[1 1 0]	10220 ± 60	6432 ± 3	3264 ± 4	3.147	31.1616
[1 1 1]		6319 ± 8	3666 ± 5		

The experiments were conducted using the powder and two-stage light gas guns in Sector 35-Hutch E of the DCS using the 24 bunch mode and reflection geometry *in-situ* x-ray diffraction (XRD) measurements. The white x-ray beam was generated using a U17.2 undulator and focused to a beam size of 100×800 μm. The reflection geometry was conducted at an x-ray-to-gun angle of $\theta_g = 10 - 11$ degrees using a 120 mm scintillation screen. The x-ray parameter details are displayed in Table 3.2 and the spectral scan of the x-rays of the 24-Bunch mode for the different APS cycles are displayed in Figure 3.2. Notice the x-ray spectrum is polychromatic, and varies depending on the APS cycle. The polychromatic spectrum is necessary since the dynamic experiments were conducted at a constant inclination angle (θ_g), thus, to obtain diffraction spots for varying d-spacings, the wavelength must vary according to Bragg's law.

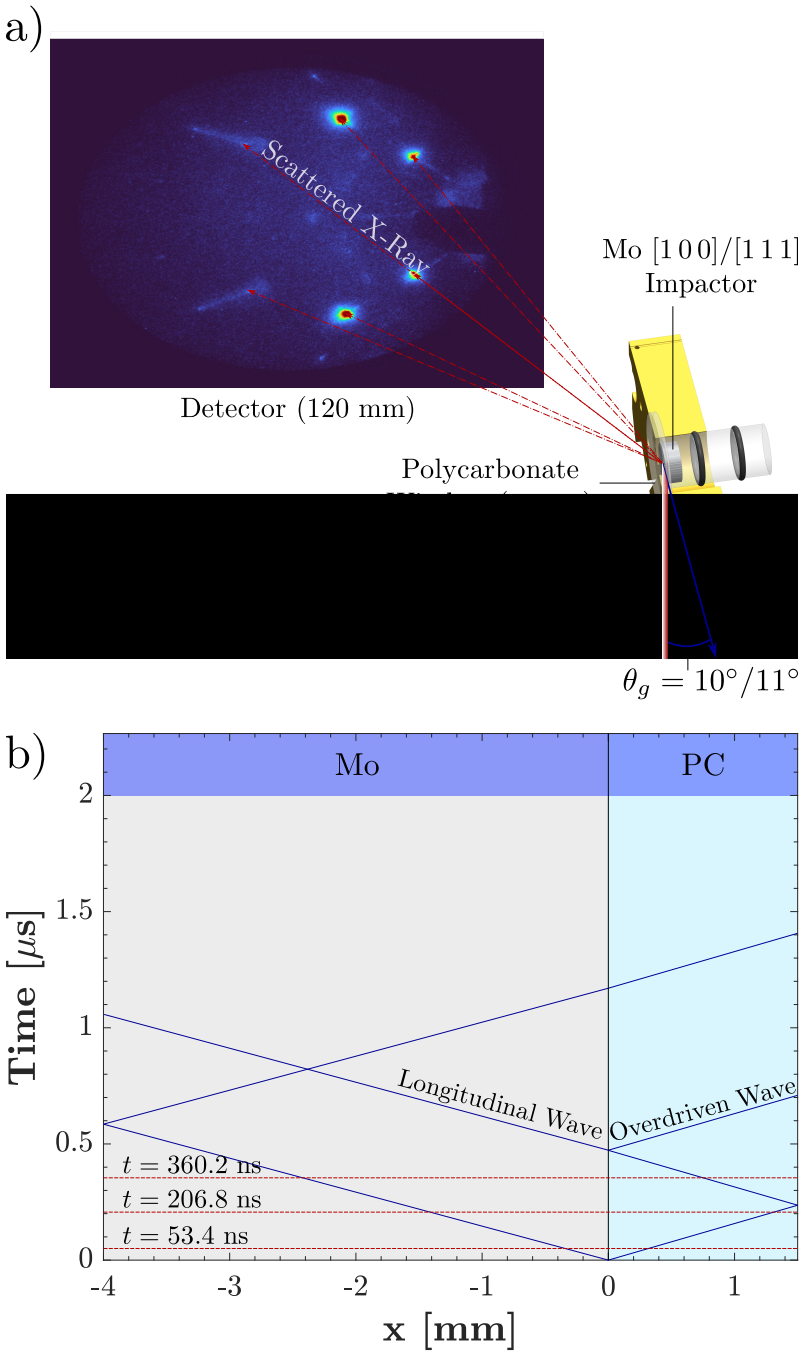

Figure 3.1: Experimental configuration at the Dynamic Compression Sector. (a) Schematic of the front surface plate impact and reflection geometry XRD configuration and (b) distance-time ($x - t$) diagram indicating the designed XRD frame capture times. Here, time $t = 0$ corresponds to the impact time and the first XRD frame, not illustrated, is designed to be obtained prior to impact at $t = -100$ ns.

Table 3.2: Details of the x-ray diffraction experimental configuration.

Undulator	Scintillator Size	Diffraction Geometry	Beam Size (Horizontal × Vertical)
U17.2 (24 KeV, 1^{st} harmonic)	120 mm	Reflection	100 μm ×800 μm

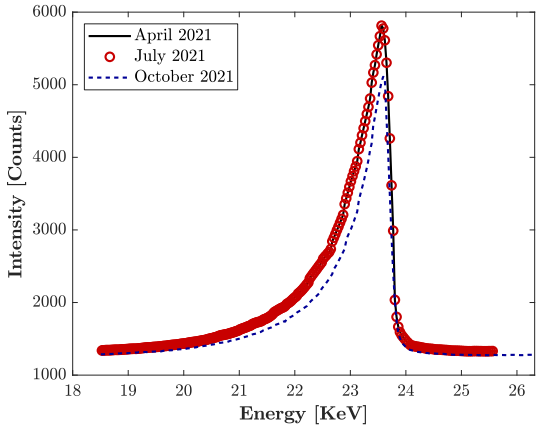

Figure 3.2: X-ray spectral scan for the 24-Bunch mode for various runs at APS.

Four XRD frames were obtained in each experiment spaced 153.4 ns apart. The front surface impact experiments were designed such that the first frame was obtained before impact ($t = -100$ ns) to calibrate the Laue diffraction spots due to potential rotation of the projectile as it traverses the barrel. The last three frames are obtained at the Hugoniot state to understand the time dependent response of the material from the movement of diffraction spots. At the pressures of interest ($8 - 19$ GPa), an overdriven wave traverses the polycarbonate sample and thus, with the current design for frame capture times, for the higher velocity experiments, only frame 2 and 3 capture the Hugoniot state. The 4th frame captures the release behavior of the molybdenum which provides important information on the elastic unloading behavior of the crystals. Additionally, due to uncertainties in gun powder explosion, the actual impact velocities deviated slightly from the desired values thus, in some experiments, the first frame was captured immediately after impact resulting in the 4th frame capturing the release behavior even for lower pressure experiments. This late impact complicates the analysis of the diffraction spots but this will be discussed in later sections. The experimental design is illustrated in the time distance ($x - t$) diagram in Figure 3.1b. Here, time $t = 0$ corresponds to the impact time and the first XRD frame, not illustrated, is designed to be obtained at $t = -100$ ns. Evolution of the laue spots from the XRD measurements were analyzed by simulating the experimental conditions in MATLAB®

to extract the lattice strains and stresses for both single crystal orientations. This requires knowledge of the detector distances which were obtained using a polycrystalline silicon standard prior to every shot and the diffraction pattern was analyzed using a combination of Dioptas software [34] and in-house polycrystalline XRD simulations. The full details of the silicon calibration is described in Section 3.3.3.

In addition to the x-rays, macroscopic laser interferometry measurements were conducted to relate the microscopic information from the XRD with these continuum measurements. Aluminum was vapor deposited (300 nm thickness) onto half the impact surface of the polycarbonate window. The transparent region of the window is used to extract the impact velocity and the deposited region is used to measure the in-material particle velocity using photonic doppler velocimetry (PDV) [35].

3.3 Simulation

The framework presented below describes the simulation process for *in-situ* x-ray diffraction (XRD) experiments conducted at the Dynamic Compression Sector (DCS) at the Advanced Photon Source (APS). The goal was to extract the lattice strains and obtain the corresponding stresses to elucidate the governing deformation mechanisms during the elastic to plastic transition in molybdenum. This analysis was done using x-ray diffraction (XRD) simulations using an in-house code developed in MATLAB® [36]. Prior to analyzing the *in-situ* diffraction data, powder XRD simulations, also using MATLAB®, were conducted on the silicon calibrant to determine the sample-to-detector distances at the location of impact. Before the silicon simulations can be conducted, the sample and detector coordinate system was established.

3.3.1 Coordinate System

The formulation for the XRD analysis begins with defining the coordinate system shown in Figure 3.3. The coordinates were decomposed into two main frames, global or laboratory ($\boldsymbol{x}_i$) and sample or local ($\hat{\boldsymbol{x}}_i$). The analysis occurs in the sample coordinate system however, for the final plotting of the detector screen, a transformation to the global system is necessary.

Based on the definition, the rotation tensor to transform from sample coordi-

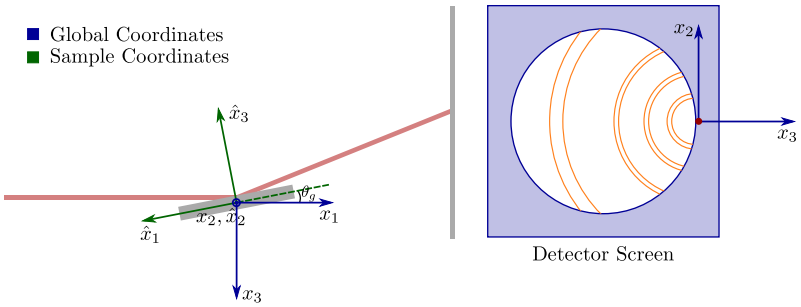

Figure 3.3: Definition of the global ($\boldsymbol{x}_i$) and sample coordinates ($\hat{\boldsymbol{x}}_i$)

nates ($\hat{\boldsymbol{x}}_i$) to global coordinates ($\boldsymbol{x}_i$) is:

$$\boldsymbol{x}_i = \boldsymbol{R}_{gs}\hat{\boldsymbol{x}}_i \tag{3.1}$$

where,

$$\boldsymbol{R}_{gs} = \begin{bmatrix} \cos\hat{\theta} & 0 & \sin\hat{\theta} \\ 0 & 1 & 0 \\ -\sin\hat{\theta} & 0 & \cos\hat{\theta} \end{bmatrix}, \qquad \hat{\theta} = 180^\circ + \theta. \tag{3.2}$$

3.3.2 Detector Geometry

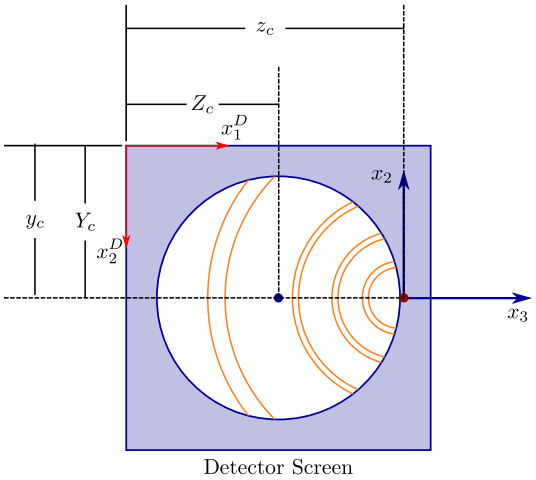

Figure 3.4: Geometry of the detector screen.

Before the diffraction frame work can be discussed, the geometry of the detector must be defined. As seen in Figure 3.4, the coordinates of the detector screen are defined from the top left corner. Next, the center of the circular

detector screen are defined by the points (Z_c, Y_c), and the beam center as (z_c, y_c). The beam center and the detector distance from the sample are determined from the silicon calibration described in later sections. To replicate the images captured during experiments, the screen size is $x_1^D \in [0, 2048]$ and $x_2^D \in [0, 2048]$ where the numerical values are in pixels (px). Additionally, the circular portion of the experimental images correspond to the detector screen which is physically 120 mm in diameter. This indicates that the length per pixel is $lpp = 68.966$ μm/px.

Effectively, when the x-ray unit diffracting vectors are calculated in simulation, they are initially in the sample frame. These vectors are transformed into the global frame using Eq. (3.1). Given the x_2, and x_3, the y- and z-components of the diffracting unit vector, the conversion to the detector frame is:

$$z = z_c + \lceil x_3/lpp \rceil \tag{3.3}$$

$$y = y_c - \lceil x_2/lpp \rceil. \tag{3.4}$$

To close out the discussion of the detector geometry, the feasible range of diffraction (2θ) angles must be considered. This is best visualized in Figure 3.5.

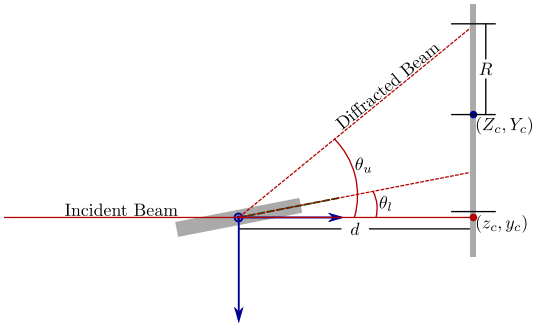

Figure 3.5: Range of diffraction angles.

Using Figure 3.5, the following relation for the limit of 2θ angles of diffraction are:

$$\theta_u = \tan^{-1}[((z_c - Z_c)lpp + R)/d] \tag{3.5}$$

$$\theta_l = max(\tan^{-1}[((z_c - Z_c)lpp - R)/d], \theta). \tag{3.6}$$

3.3.3 Silicon Calibration

Having established the detector geometry, the detector distance, and the x-ray properties, one can now focus on extracting the information using the silicon calibrant. An iterative process was conducted to accurately determine the sample-to-detector distances, the detector center, and beam center. Since the x-ray spectrum is polychromatic, an initial pass using a public domain software Dioptas [34] and the peak wavelength of the spectrum was conducted. Using the parameters obtained from this initial guess, the powder simulations were conducted, which account for the entire wavelength spectrum, by varying the detector distance slightly. The simulated diffraction pattern was compared to the experimental image via azimuthal integration and the finalized detector distance was considered to minimize the distance between the simulated and the experimental peaks. An example of the azimuthally integrated profiles are shown in Figure 3.6.

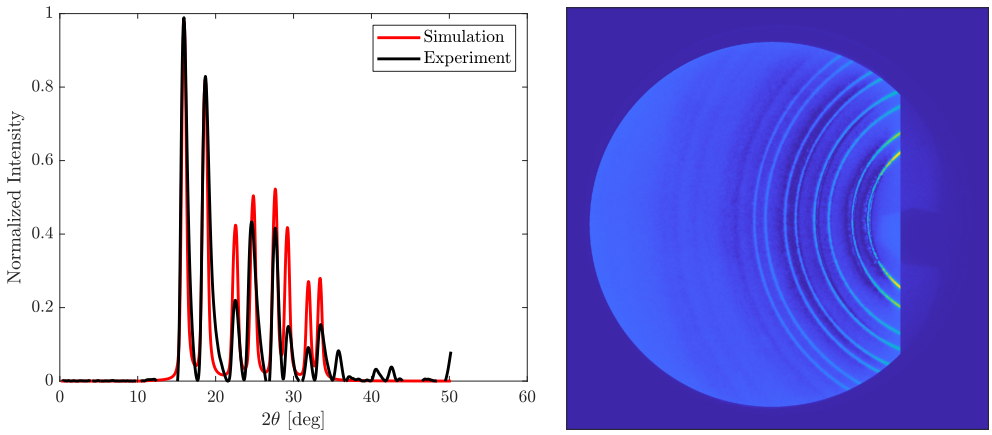

(a) (b)

Figure 3.6: Silicon calibration for Shot 21–05–56 used to determine the geometrical detector parameters for the experiment. (a) Azimuthally integrated silicon pattern and (b) overlay of the simulated pattern on the experimental data. Here, the obtained parameters were as follows: *Detector Distance:* 101.70 mm, *Detector Center:* (998 px, 1053 px), *Beam Center:* (1884 px, 1020 px).

Having established the silicon calibration, the next section focuses on the single crystal Laue simulations for Mo and describes the procedure to extract the strains from the experimental measurements.

3.3.4 Initialization

The formulation for the code used to simulate the diffraction spots observed for the single crystal molybdenum experiments is discussed. The procedure for initializing the information on molybdenum (Mo), which is summarized in Table 3.1, is described below.

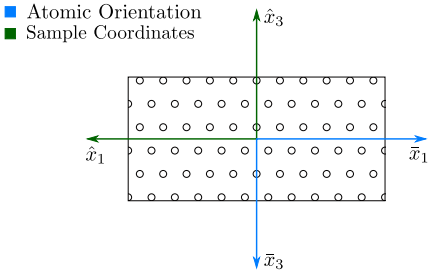

Figure 3.7: Atoms arranged within the single crystal sample.

Consider the arrangement of atoms within the single crystal sample in Figure 3.7. The direction of compression and x-ray imaging occurs along the $\hat{\boldsymbol{x}}_{\boldsymbol{3}}$ direction. Therefore, the orientation of the crystal must be aligned to the axis of compression. This can be done by first defining the orientation vector $\boldsymbol{O}$ (e.g. $\boldsymbol{O} = [1\,1\,1]^T$) and its unit vector as $\hat{\boldsymbol{O}} = \boldsymbol{O}/\|\boldsymbol{O}\|$. Given the sample normal to be $\hat{\boldsymbol{n}} = [0\,0\,1]^T$, the rotation tensor is defined as follows:

$$\boldsymbol{v} = \hat{\boldsymbol{O}} \times \hat{\boldsymbol{n}}. \tag{3.7}$$

The skew symmetric matrix is constructed using the components of $\boldsymbol{v}$:

$$\boldsymbol{W} = \begin{bmatrix} 0 & -v_3 & v_2 \\ v_3 & 0 & -v_1 \\ -v_2 & v_1 & 0 \end{bmatrix}. \tag{3.8}$$

The rotation tensor can then be written as:

$$\boldsymbol{R}_{\mathcal{O}} = \boldsymbol{I} + \boldsymbol{W} + \left(\frac{1 - (\hat{\boldsymbol{n}} \cdot \hat{\boldsymbol{O}})}{\|\boldsymbol{v}\|^2} \right) \boldsymbol{W}^2. \tag{3.9}$$

Once the orientation of the sample has been aligned to the sample coordinate system, an alternate set of rotation tensors need to be constructed to characterize misorientation of the single crystal sample. Figure 3.8 illustrates this concept.

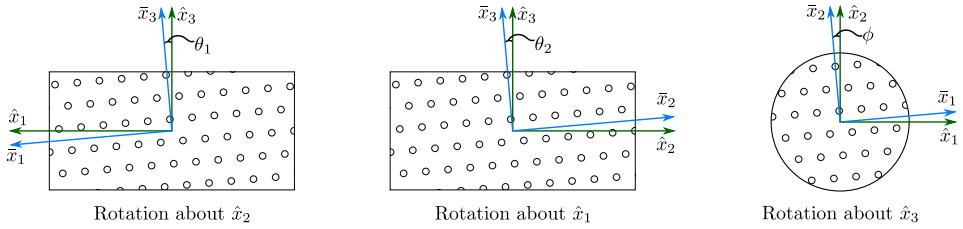

Figure 3.8: Misorientation of the atomic orientation to the sample axis.

Instead of using Euler angles, one can effectively construct a rotation tensor about some vector $\boldsymbol{x}$ and by some angle ϕ in the sample frame to simulate the realistic arrangement of the atoms using the Rodrigues' rotation formula. The rotation tensor can be constructed as follows:

$$\boldsymbol{u} = \boldsymbol{x}/\|\boldsymbol{x}\| \tag{3.10}$$

$$\boldsymbol{W} = \begin{bmatrix} 0 & -u_3 & u_2 \\ u_3 & 0 & -u_1 \\ -u_2 & u_1 & 0 \end{bmatrix} \tag{3.11}$$

$$\boldsymbol{R}_m = \boldsymbol{I} + \boldsymbol{W}\sin\phi + \boldsymbol{W}^2 \cdot 2\sin^2(\phi/2). \tag{3.12}$$

3.3.5 XRD Theory

With the coordinate systems defined, the procedure to model the diffraction spots of single crystal molybdenum can be formulated. This work follows Chapter 6 from the textbook by Fultz [37] and starts by introducing the concept of real and reciprocal space. For real space, consider a crystal lattice with primitive translation vectors $\boldsymbol{a}_1$, $\boldsymbol{a}_2$, and $\boldsymbol{a}_3$. All lattice sites are obtained by the translations $\boldsymbol{r}$ from a reference site at the origin:

$$\boldsymbol{r} = m\boldsymbol{a}_1 + n\boldsymbol{a}_2 + o\boldsymbol{a}_3$$

where m, n, o are independent integers. One can further decompose the locations of the atoms in the crystal into the following parts:

$$\underbrace{\boldsymbol{r}}_{\text{crystal}} = \underbrace{\boldsymbol{r}_g}_{\text{lattice}} + \underbrace{\boldsymbol{r}_k}_{\text{basis}}. \tag{3.13}$$

Here, the defects present in the sample are neglected. For a body-centered cubic (BCC) crystal structure, the crystal structure can be treated as a composite simple cubic structure where one basis starts at the origin of the defined coordinate system (choosing some arbitrary atom) and the second basis is shifted to the center atom in the crystal. Thus, the basis vectors are $\boldsymbol{r}_{k1} = 0\boldsymbol{a}_1 + 0\boldsymbol{a}_2 + 0\boldsymbol{a}_3$ (the origin) and $\boldsymbol{r}_{k2} = \frac{1}{2}\boldsymbol{a}_1 + \frac{1}{2}\boldsymbol{a}_2 + \frac{1}{2}\boldsymbol{a}_3$.

Simultaneously the reciprocal space lattice vectors $\boldsymbol{g}$ are defined with the primitive translation vectors $\boldsymbol{a}_1^*$, $\boldsymbol{a}_2^*$, and $\boldsymbol{a}_3^*$. The primitive vectors are obtained by

$$\boldsymbol{a}_1^* = 2\pi \frac{\boldsymbol{a}_2 \times \boldsymbol{a}_3}{\boldsymbol{a}_1 \cdot \boldsymbol{a}_2 \times \boldsymbol{a}_3} \tag{3.14}$$

$$\boldsymbol{a}_2^* = 2\pi \frac{\boldsymbol{a}_3 \times \boldsymbol{a}_1}{\boldsymbol{a}_2 \cdot \boldsymbol{a}_3 \times \boldsymbol{a}_1} \tag{3.15}$$

$$\boldsymbol{a}_3^* = 2\pi \frac{\boldsymbol{a}_1 \times \boldsymbol{a}_2}{\boldsymbol{a}_3 \cdot \boldsymbol{a}_1 \times \boldsymbol{a}_2}. \tag{3.16}$$

Thus, the reciprocal vector is defined as

$$\boldsymbol{g} = h\boldsymbol{a}_1^* + k\boldsymbol{a}_2^* + l\boldsymbol{a}_3^* \tag{3.17}$$

where h, k, l are integers and define the crystallographic Miller indices. Thus, the scattering vector $\Delta\boldsymbol{k}$ is defined as:

$$\Delta\boldsymbol{k} = \boldsymbol{k} - \boldsymbol{k}_0 \tag{3.18}$$

where $\boldsymbol{k}$ is the diffracted wave vector and $\boldsymbol{k}_0$ is the incident wave vector. For elastic scattering to occur, the magnitude of both the diffracted and incident wave vectors must be the same and therefore, $\|\boldsymbol{k}\| = \|\boldsymbol{k}_0\| = 2\pi/\lambda$. Additionally, it is important to declare that $\|\Delta\boldsymbol{k}\| = \|\boldsymbol{k} - \boldsymbol{k}_0\| = 2\|\boldsymbol{k}\|\sin(\theta) = 4\pi/\lambda \cdot \sin(\theta)$. These quantities will be explicitly defined for the diffraction problem in the subsequent sections.

Since diffraction is a wave interference phenomenon, the diffracted intensity is defined as $I_{\text{scatt}} = \psi^*\psi$. Consider the expression for scattered wave [37]:

$$\psi(\Delta\boldsymbol{k}) = \underbrace{\sum_{\boldsymbol{r}_g} \mathrm{e}^{-\mathrm{i}2\pi\Delta\boldsymbol{k}\cdot\boldsymbol{r}_g}}_{\mathcal{S}(\Delta\boldsymbol{k})} \underbrace{\sum_{\boldsymbol{r}_k} f_{at}(\boldsymbol{r}_k)\mathrm{e}^{-\mathrm{i}2\pi\Delta\boldsymbol{k}\cdot\boldsymbol{r}_k}}_{\mathcal{F}(\Delta\boldsymbol{k})} \tag{3.19}$$

here, $\mathcal{S}(\Delta\boldsymbol{k})$ is the shape factor and $\mathcal{F}(\Delta\boldsymbol{k})$ is the structure factor. One can show that diffraction occurs when the Laue condition, $\Delta\boldsymbol{k} = \boldsymbol{g}$, is satisfied. For this case, since the system is considered as a composite simple cubic (SC), it turns out that $\mathcal{S}_{SC}(\Delta\boldsymbol{k}) = N$. If there is any deviation from an ideal lattice, one must account for the deviation vector which complicates the determination of the shape factor. This discussion is neglected and the reader is directed to the textbook by Fultz [37]. Here, the shape factor is neglected and considered that the scattering intensity scales as $I_{\text{scatt}} \propto |\mathcal{F}(\Delta\boldsymbol{k})|^2$.

The structure factor must now be determined to close this discussion. For a BCC lattice, there are two basis vectors. Thus, the two terms in the expression defined in Eq. (3.19) is summed and the Laue condition $\Delta\boldsymbol{k} = \boldsymbol{g}$ is employed. This yields

$$\mathcal{F}_{\text{bcc}}(\Delta\boldsymbol{k}) = f_{\text{at}}(0)\mathrm{e}^0 + f_{\text{at}}\left(\frac{1}{2},\frac{1}{2},\frac{1}{2}\right)\mathrm{e}^{-\mathrm{i}2\pi\left(h\frac{1}{2}+k\frac{1}{2}+l\frac{1}{2}\right)}. \tag{3.20}$$

For a pure metal such as molybdenum, the atomic form factor at both of the basis vectors will be the same since the atoms at these locations are the same. Therefore, Eq. (3.20) reduces to the expected:

$$\mathcal{F}_{\text{bcc}}(\Delta\boldsymbol{k}) = 2f_{\text{at}}, \qquad h+k+l = \text{ even number}. \tag{3.21}$$

Here, the atomic scattering factor, f_{at}, is tabulated for most materials as a function of $s = \|\Delta\boldsymbol{k}/4\pi\| = \sin(\theta)/\lambda$. Since x-ray spectrum is polychromatic, the atomic scattering factors must be determined for each wavelength.

3.3.6 XRD Simulation

With the fundamentals established, the formulation is specialized for the specific experimental configuration at the Dynamic Compression Sector (DCS). Consider the coordinate system in Figure 3.3. In the global coordinate system, incident wave vector is defined as a function of wavelength λ_i to be $\boldsymbol{k}_0 = 2\pi/\lambda_i\boldsymbol{x}_1 + 0\boldsymbol{x}_2 + 0\boldsymbol{x}_3$. Working in the sample coordinate system is convenient thus, a rotation using $\boldsymbol{R}_{gs}^T$ (Eq. (3.1)) and a gun angle of $\theta_g = 11^\circ$ is conducted to obtain,

$$\boldsymbol{k}_{0i} = 2\pi/\lambda_i\left[-\cos(11^\circ)\hat{\boldsymbol{x}}_1 + 0\hat{\boldsymbol{x}}_2 + \sin(11^\circ)\hat{\boldsymbol{x}}_3\right]. \tag{3.22}$$

In addition to the incident wave vector, the known scattering wave vector is defined:

$$\Delta \boldsymbol{k}_i^a = h_i \boldsymbol{a}_1^* + k_i \boldsymbol{a}_2^* + l_i \boldsymbol{a}_3^*, \qquad h,k,l = -5,-4,...,5 \text{ and } i = 1,...,1331. \tag{3.23}$$

For simplicity, it is assumed that the lattice in the reciprocal space only spans the first 5 Miller indices. This defines the crystal in the reciprocal space and one can use structure factor calculations (Eq. (3.20)) to reduce the indices to only the ones that satisfy the diffraction rules for BCC structure. Next, these scattering vectors must be rotated to account for the orientation of the crystal, Eq. (3.9), based on the experimental configuration. Simultaneously, any misorientation of the crystal through rotation along the sample coordinate ($\hat{\boldsymbol{x}}_i$) system is accounted for using Eq. (3.12). Thus,

$$\Delta \boldsymbol{k}_i = \frac{2\pi}{a_0} \boldsymbol{R}_z(\phi) \boldsymbol{R}_x(\theta_2) \boldsymbol{R}_y(\theta_1) \boldsymbol{R}_{\mathcal{O}} \Delta \boldsymbol{k}_i^a \tag{3.24}$$

where a_0 corresponds to the initial lattice parameter and θ_1, θ_2, ϕ, correspond to the misorientation angles along $\hat{\boldsymbol{x}}_2$, $\hat{\boldsymbol{x}}_1$, $\hat{\boldsymbol{x}}_3$, respectively. Using the scattering vector, the atomic structure factor is obtained by first evaluating the d-spacing, $d_{hkl} = 2\pi / \|\Delta \boldsymbol{k}_i\|$, followed by calculating $s = 1/(2d_{hkl})$ from which the atomic scattering factor, f_{at}, is determined. As an aside, note the diffraction angle (2θ) can be determined using the expression $\lambda_i/(4\pi) \cdot \|\Delta \boldsymbol{k}_i\| = \lambda_i/(2d_{hkl}) = \sin(2\theta)$.

The detector essentially displays the diffracted wave vectors, $\boldsymbol{k}$. Thus, by rearranging Eq. (3.18),

$$\boldsymbol{k}_i = \Delta \boldsymbol{k}_i + \boldsymbol{k}_{0i}, \qquad i = 1,...,1331. \tag{3.25}$$

Here, the determined diffracted wave vectors are in the sample frame. Also, as mentioned earlier, XRD deals with elastic scattering and thus the L2-norm of these vectors must equal $\|\boldsymbol{k}_i\| = 2\pi/\lambda_i$ similar to the incident wave vector $\boldsymbol{k}_{0i}$. Based on Eq. (3.25), it is not guaranteed that all vectors satisfy the constraint for the norm thus, only the diffracted vectors and their corresponding indices that satisfy the criteria $0.999 \leq \|\boldsymbol{k}_i\|/(2\pi/\lambda_i) \leq 1.001$ are considered. This is another way to say the diffraction occurs only when the Ewald condition is satisfied.

The diffracted vectors can now be rotated back onto the global coordinates ($\boldsymbol{x}_i$) and projected onto the detector. However, after applying the appropriate rotation, the vectors must satisfy additional constraints. These constraints are defined due to the physical geometry of the detector and the directionality of the diffracted wave vector. Therefore, the allowable diffracted wave vectors and the respective diffraction angles, θ_i, are

$$\boldsymbol{k}_i, \theta_i \qquad \text{s.t.} \begin{cases} 2\theta_i \leq \theta_u \\ 2\theta_i \geq \theta_l \\ h = k = l \neq 0 \\ \frac{\boldsymbol{k}_i}{\|\boldsymbol{k}_i\|} \cdot \boldsymbol{x}_1 > 0 \\ \sum_i (\boldsymbol{k}_i \cdot \boldsymbol{k}_{0i}) \neq 0 \end{cases} . \tag{3.26}$$

With the allowable vectors determined, a corresponding intensity is assigned to these vectors using

$$I_i = I_{0i}(\lambda_i)|\mathcal{F}(\Delta \boldsymbol{k})|^2 \mathrm{e}^{-[L_{\mathrm{Mo}}/A_{\mathrm{Mo}}(\lambda_i) + L_{\mathrm{PC}}/A_{\mathrm{PC}}(\lambda_i)]} \tag{3.27}$$

where, $I_{0i}(\lambda_i)$ is the intensity of the spectrum corresponding to the x-ray wavelength, L_{Mo} is the x-ray penetration depth in the molybdenum, L_{PC} is the thickness of the polycarbonate window, $A_{\mathrm{Mo}}(\lambda_i)$ is the attenuation coefficient of molybdenum for a given wavelength, and $A_{\mathrm{PC}}(\lambda_i)$ is the attenuation coefficient for polycarbonate. Given the allowable diffracted wave vectors and their corresponding intensities, these quantities are projected onto a virtual detector.

To simulate the detector screen, the diffracted wave vectors were first projected onto the plane of the detector given the detector distance and the location of the beam center. Next, the intersection of the vectors with the detector plane were converted into a pixel coordinate system after which a Gaussian filter with a FWHM was applied to emulate the x-ray broadening from the detector. This was done using Eqs. (3.3) and (3.4) where the input was R_0. It is important to point out that the pixel coordinates of R_0 that exceed the limit of the image and the values outside of the detector circle were neglected.

3.3.7 Lattice Strains

Once the general methodology for simulating the diffraction patterns is established, these simulations are used to extract the lattice strains and rotations for which the procedure is described below. The formulation here was based on the notes by Miller [38].

This discussion begins by assuming that a deformation gradient $\boldsymbol{F}_{ij}$ takes a vector from the undeformed sample coordinate system $\hat{\boldsymbol{x}}_i$ to the deformed sample coordinate system $\hat{\boldsymbol{y}}_i$ through the operation

$$\hat{\boldsymbol{y}}_i = \boldsymbol{F}_{ij}\hat{\boldsymbol{x}}_j. \tag{3.28}$$

Recall that the crystal lattice was defined in the $\boldsymbol{a}_i$ basis and thus, after some applied deformation, the deformed lattice ($\boldsymbol{a}_i^d$) can be expressed as

$$\boldsymbol{a}_i^d = \boldsymbol{F}_{ij}\boldsymbol{a}_j. \tag{3.29}$$

For convenience, the lattice is defined in the reciprocal space. The relation between the deformed crystal lattice in the reciprocal space and the undeformed can be shown by substituting Eq. (3.29) into Eqs. (3.14), (3.15), and (3.16) and invoking vector identities. This relation simplifies to

$$\boldsymbol{a}_i^{d*} = \boldsymbol{F}^{-T}\boldsymbol{a}_i^*. \tag{3.30}$$

Using the expression for the scattering vector, the expression for the diffracted vector is rewritten as follows:

$$\boldsymbol{k}_i = \boldsymbol{F}^{-T}\Delta\boldsymbol{k}_i + \boldsymbol{k}_{0i}. \tag{3.31}$$

With this established, the goal is to determine the deformation gradient that describes the shifting of the Laue diffraction spots observed in the experimental images. This can be done by converting to an optimization problem using the simulations developed for molybdenum here. First, the expression for the diffracted wave vectors is rewritten as a function of wavelength by splitting its magnitude and direction:

$$\boldsymbol{k}_i(\lambda_n) = \hat{\boldsymbol{k}}_i\left\|\boldsymbol{F}^{-T}\Delta\boldsymbol{k}_i + \boldsymbol{k}_{0i}(\lambda_n)\right\| \tag{3.32}$$

where, $\hat{\boldsymbol{k}}_i$ corresponds to the direction of the diffracted wave vector.

The methodology goes as follows. First, a Lorentzian fit is applied to the experimental images to determine the pixel location corresponding to the peak of each diffraction spot, Fig. 3.9. Next, given the known calibration parameters and the pixel coordinates of the spots, the unit diffracted wave vectors (directions) are determined through an inverse mapping from the detector (see Fig. 3.10). Note there is however an inherent uncertainty to this methodology because multiple $\hat{\boldsymbol{k}}_i$ vectors could be mapped to the same pixel on the detector if the variations are very small. Once the diffraction vectors are determined, the goal is to find the deformation gradient that minimizes the following objective function which is essentially a restatement of Eq. (3.31):

$$\mathcal{O} = \min_{\boldsymbol{F}^{-T}} \left(\sum_{i=1}^{M} \sum_{n=1}^{N} \left\| \boldsymbol{F}^{-T} \Delta \boldsymbol{k}^n - \hat{\boldsymbol{k}}^n \right\| \boldsymbol{F}^{-T} \Delta \boldsymbol{k}^n + \boldsymbol{k}_0^n(\lambda_i^n) \right\| + \boldsymbol{k}_0^n(\lambda_i^n) \right\| \right) \tag{3.33}$$

here, N corresponds to the number of diffraction spots and M corresponds to the number of wavelengths in the spectrum. This minimization problem is conducted using the *fmincon* function in MATLAB® [36]. Validation of this technique is presented in the following section.

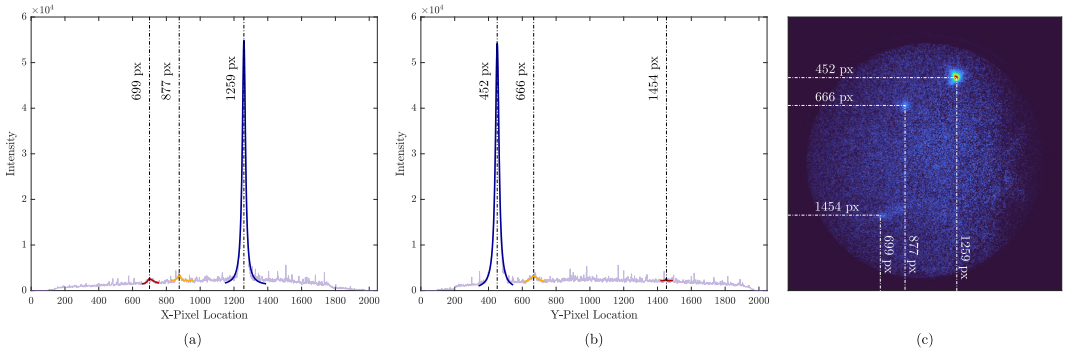

Figure 3.9: The centroid of the diffraction spots along the (a) x-pixel direction and (b) the y-pixel direction are determined using the Lorentzian function fits. (c) These centers are plotted on a representative XRD image from an experiment.

3.3.8 XRD Verification

The verification of this technique using the simulation environment and virtually applied deformations is presented next. For the first test case, no constraints on the deformation gradient are assumed and all nine components of

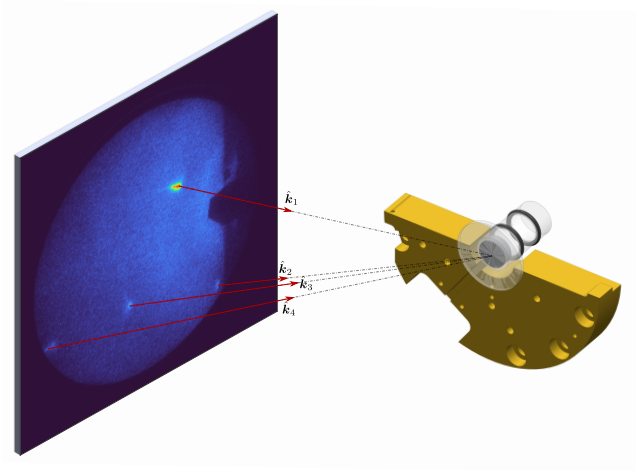

Figure 3.10: Inverse mapping of the unit diffracted wave vectors from the detector images used for the optimization procedure for determining the deformation gradient.

the tensor are determined using 9 diffraction spots. The second validation case assumes that the material undergoes small strains. Thus, using a linear approximation, the 6 components of the symmetric deformation gradient are determined. Lastly, since a typical experiment on molybdenum yields two to four diffraction spots, an additional constraint is applied to simplify the deformation gradient. These will now be discussed in detail.

Table 3.3: Summary of the validation tests for the optimization scheme.

Parameter	**9 Spots**	**6 Spots**	**3 Spots**
Detector Distance	50e3 μm	75e3 μm	100e3 μm
θ_1	0°	0°	0°
θ_2	0°	0°	0°
ϕ	0°	0°	0°
Beam Center	(1883 px, 1022 px)	(1883 px, 1022 px)	(1883 px, 1022 px)
Detector Center	(1000 px, 1051 px)	(1000 px, 1051 px)	(1000 px, 1051 px)
Orientation	[1 0 0]	[1 0 0]	[1 0 0]
Deformation Gradient	$\boldsymbol{F} = \begin{bmatrix} 1 & 0 & 0 \\ 0 & 1 & 0.005 \\ 0 & 0 & 0.95 \end{bmatrix}$	$\boldsymbol{F} = \begin{bmatrix} 1 & 0 & 0 \\ 0 & 1 & 0.005 \\ 0 & 0.005 & 0.95 \end{bmatrix}$	$\boldsymbol{F} = \begin{bmatrix} 1 & 0 & 0 \\ 0 & 1 & 0.005 \\ 0 & 0.005 & 0.95 \end{bmatrix}$

Example: 9 Diffraction Spots

The deformation gradient shown in Table 3.3 is imposed within the simulation. Since the deformation gradient is known, the minimization problem can be solved to recover the same deformation gradient using the methodology

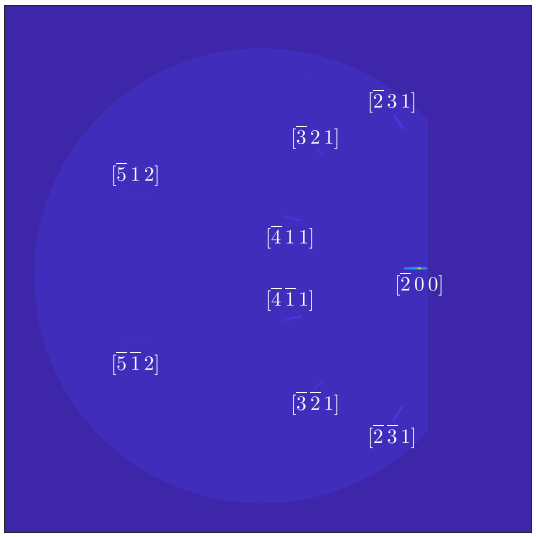

Figure 3.11: Simulated diffraction spots for the 9-spot case.

described above. For this example, no constraints are imposed on the objective function since there are 9 spots and there are 9 components of the deformation gradient. Note for the simulation, the values of the x-ray wavelengths that allow us to minimize the objective are already known. However, for an actual experiment, a series of wavelengths need to be iterated between to obtain the optimal solution to the objective function. This means one must determine both the wavelength and the deformation gradient that minimizes the objective.

For this particular example, the optimal deformation gradient is

$$\boldsymbol{F}_{in} = \begin{bmatrix} 1 & 0 & 0 \\ 0 & 1 & 0.005 \\ 0 & 0 & 0.95 \end{bmatrix}, \qquad \boldsymbol{F}_{out} = \begin{bmatrix} 1.0054 & 0.0008 & -0.0003 \\ 0.0007 & 1.0002 & 0.0042 \\ -0.0002 & -0.0004 & 0.9514 \end{bmatrix}. \quad (3.34)$$

Notice how different the above computed deformation gradient ($\boldsymbol{F}_{out}$) is compared to the imposed ($\boldsymbol{F}_{in}$). As stated earlier, this is because multiple diffracted wave vectors, $\boldsymbol{k}$, can be mapped to the same pixel on the detector. Thus, when projecting the detector spots back to the sample, since each pixel corresponds to 68.966 μm of displacement physically, there is an inherent error in the converged solution.

Example: 6 Diffraction Spots

In a typical experiment, depending on the material and the x-ray beam properties, obtaining 9 diffraction spots may be difficult. Additionally, elastic strains in these shock experiments at low pressures may not be significant and thus, it is convenient to use the linearized approximation for the deformation gradient, $\boldsymbol{F} = \boldsymbol{I} + \boldsymbol{\varepsilon}$. Here, $\boldsymbol{\varepsilon}$ is the infinitesimal strain tensor thus, due to its symmetry, the number of unknowns drop from nine to six. This means an additional constraint must be applied to ensure a symmetric deformation gradient from the converged solution. An example using this assumption and constraint is presented below. For the imposed deformation gradient, the diffraction spots obtained are

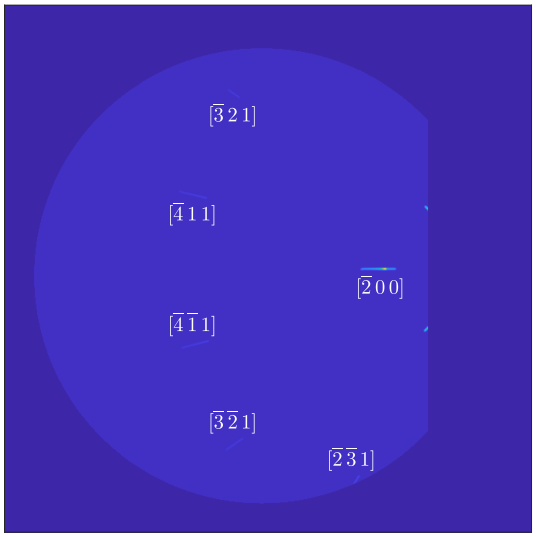

Figure 3.12: Simulated diffraction spots for the 6-spot case.

With this, the output optimized deformation gradient is,

$$\boldsymbol{F}_{in} = \begin{bmatrix} 1 & 0 & 0 \\ 0 & 1 & 0.005 \\ 0 & 0.005 & 0.95 \end{bmatrix}, \quad \boldsymbol{F}_{out} = \begin{bmatrix} 1.0024 & -0.0004 & -0.0009 \\ -0.0004 & 1.0002 & 0.0052 \\ -0.0009 & 0.0052 & 0.9508 \end{bmatrix}. \quad (3.35)$$

Note the deformation gradient from the converged solution to the objective still has an inherent uncertainty to the values but they become lower due to the imposed constraints.

Example: 3 Diffraction Spots

In a typical experiment, the number of diffraction spots that are obtained are on the order of 2-4 depending on how much the impactor rotates as it travels along the barrel. This provides less data for obtaining the deformation gradient and thus an additional constraint is imposed. Since plate impact experiments are typically under uniaxial strain conditions macroscopically, a plane strain constraint is imposed on the system. Thus for this case, the simulated diffraction spots and the calculated deformation gradient are:

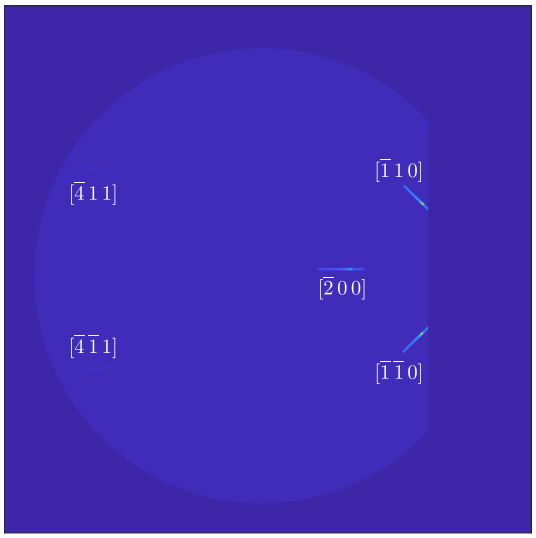

Figure 3.13: Simulated diffraction spots for the 3-spot case.

$$\boldsymbol{F}_{in} = \begin{bmatrix} 1 & 0 & 0 \\ 0 & 1 & 0.005 \\ 0 & 0.005 & 0.95 \end{bmatrix}, \qquad \boldsymbol{F}_{out} = \begin{bmatrix} 1.0000 & 0.0004 & 0.0004 \\ 0.0004 & 1.0003 & 0.0050 \\ 0.0004 & 0.0050 & 0.9504 \end{bmatrix}. \tag{3.36}$$

Notice the output deformation gradient ($\boldsymbol{F}_{out}$) almost perfectly matches the imposed conditions ($\boldsymbol{F}_{in}$). The possible reason for this result is once again due to the symmetry constraints imposed while simultaneously, the components $0.999 \leq \boldsymbol{F}_{11} \leq 1.001$, $-0.0005 \leq \boldsymbol{F}_{12} \leq 0.0005$ and $-0.0005 \leq \boldsymbol{F}_{13} \leq 0.0005$ are constrained due to plane strain conditions. These bounds are simply for numerical reasons. Additionally, since the number of diffraction spots in this test case are less than previous validation simulations and thus, the overall error contribution from the inverse diffracted wave vector mapping is reduced.

3.3.9 Stress Calculations

Using the deformation gradients, the stress tensor can be determined. The Lagrangian elastic strain tensor is defined as:

$$\boldsymbol{E}^e = \frac{1}{2}\left(\boldsymbol{F}_e^T \boldsymbol{F}_e - \boldsymbol{I}\right). \tag{3.37}$$

Using this, the stress tensor is

$$\boldsymbol{\sigma}_{ij} = \boldsymbol{C}_{ijkl}\boldsymbol{E}^e_{kl} \tag{3.38}$$

here, $\boldsymbol{C}_{ijkl}$ is the elasticity moduli tensor of molybdenum and is rotated accordingly depending on which orientation is being loaded in the experiment. The moduli tensor for the [1 0 0] and [1 1 1] orientations, respectively, are (units of GPa):

$$\boldsymbol{C}_{ij}^{[1\,0\,0]} = \begin{bmatrix} 466.1 & 162.6 & 162.6 & 0.0 & 0.0 & 0.0 \\ 162.6 & 466.1 & 162.6 & 0.0 & 0.0 & 0.0 \\ 162.6 & 162.6 & 466.1 & 0.0 & 0.0 & 0.0 \\ 0.0 & 0.0 & 0.0 & 109.5 & 0.0 & 0.0 \\ 0.0 & 0.0 & 0.0 & 0.0 & 109.5 & 0.0 \\ 0.0 & 0.0 & 0.0 & 0.0 & 0.0 & 109.5 \end{bmatrix} \tag{3.39}$$

$$\boldsymbol{C}_{ij}^{[1\,1\,1]} = \begin{bmatrix} 423.8 & 176.7 & 190.8 & -14.1 & 14.1 & 0.0 \\ 176.7 & 423.8 & 190.8 & 14.1 & -14.1 & 0.0 \\ 190.8 & 190.8 & 409.7 & 0.0 & 0.0 & 0.0 \\ -14.1 & 14.1 & 0.0 & 137.7 & 0.0 & -14.1 \\ 14.1 & -14.1 & 0.0 & 0.0 & 137.7 & -14.1 \\ 0.0 & 0.0 & 0.0 & -14.1 & -14.1 & 123.6 \end{bmatrix}. \tag{3.40}$$

The resolved shear stresses (τ_{rss}) are extracted using,

$$\tau_{rss} = \hat{\boldsymbol{n}}_k \cdot \boldsymbol{\sigma}\hat{\boldsymbol{b}}_k \tag{3.41}$$

where, $\hat{\boldsymbol{n}}$ is the twin plane normal, and $\hat{\boldsymbol{b}}$ is the twinning shear direction.

When twinning occurs, a multiplicative decomposition of the deformation gradient ($\boldsymbol{F} = \boldsymbol{F}_e\boldsymbol{F}_t$) is employed where $\boldsymbol{F}_e$ is the elastic deformation gradient and $\boldsymbol{F}_t$ is the twinning deformation gradient. The twinning deformation gradient is expressed using

$$\boldsymbol{F}_t = \boldsymbol{I} + \gamma \hat{\boldsymbol{b}} \otimes \hat{\boldsymbol{n}} \tag{3.42}$$

where, $\boldsymbol{I}$ is the identity tensor, $\gamma = \frac{1}{\sqrt{2}}$ is the twinning shear magnitude for molybdenum [39].

3.4 Results and discussions

Front surface impact experiments were conducted using Molybdenum single crystal impactors and a polycarbonate target which also acts as a window for interferometry. A summary of the results and the window corrected free surface velocities are displayed in Table 3.4 and Figure 3.14, respectively.

Table 3.4: Summary of experimental results for Mo single crystals using both continuum and XRD analysis.

Experiment	Orientation	Sample Thickness [mm]	Window Thickness [mm]	Impact Velocity [m/s]	u_p [m/s]	Normal Stress [GPa]	1st Frame [ns]	σ_{vm} [GPa]
Mo100-10-1	[1 0 0]	2.490 ± 0.001	1.498 ± 0.001	1818.9	1668	9.04	-11.0	—
Mo100-10-2	[1 0 0]	2.490 ± 0.002	1.468 ± 0.004	1762.3	1617	8.63	18.0	$4.6e9 \pm 2.2e9$
Mo100-10-3	[1 0 0]	4.045 ± 0.001	1.508 ± 0.001	1809.6	1658	8.97	27.2	$4.9e9 \pm 2.8e9$
Mo100-15-1	[1 0 0]	2.499 ± 0.001	1.511 ± 0.001	2315.7	2095	13.01	29.0	$6.4e9 \pm 4.3e9$
Mo100-20-1	[1 0 0]	2.525 ± 0.002	1.507 ± 0.003	2994.6	—	—	68.4	—
Mo100-20-2	[1 0 0]	4.066 ± 0.001	1.512 ± 0.002	2849.7	2540	17.85	52.4	$3.9e9 \pm 0.8e9$
Mo111-10-1	[1 1 1]	4.047 ± 0.005	1.526 ± 0.001	1842.2	—	—	-56.0	—
Mo111-10-2	[1 1 1]	4.050 ± 0.002	1.497 ± 0.002	1809.6	1662	9.00	-40.0	$3.1e9 \pm 1.5e9$
Mo111-15-1	[1 1 1]	4.045 ± 0.003	1.469 ± 0.002	2341.3	2114	13.22	-91.0	$3.8e9 \pm 0.9e9$
Mo111-15-2	[1 1 1]	3.966 ± 0.003	1.506 ± 0.001	2338.9	2114	13.20	-33.1	—
Mo111-20-1	[1 1 1]	4.028 ± 0.003	1.514 ± 0.001	2965.9	2637	19.00	14.7	—
Mo111-20-2	[1 1 1]	4.017 ± 0.004	1.481 ± 0.002	2703.2	2421	16.49	-72.9	$5.5e9 \pm 1.3e9$
Mo111-20-3	[1 1 1]	4.055 ± 0.004	1.476 ± 0.001	2852.0	2543	17.88	-15.5	$4.5e9 \pm 2.1e9$

** The samples refer to molybdenum (Mo) impactors
** σ_{vm} corresponds to the von Mises stress obtained from diffraction data

Since the interferometry measurements were conducted through the polycarbonate window, the change in index of refraction of the polycarbonate needs to be accounted for in the velocity analysis. This is done using the standard window analysis by Barker and Hollenbach [40] and using the index of refraction coefficients from Hawreliak et al. [7]. The equations are as follows:

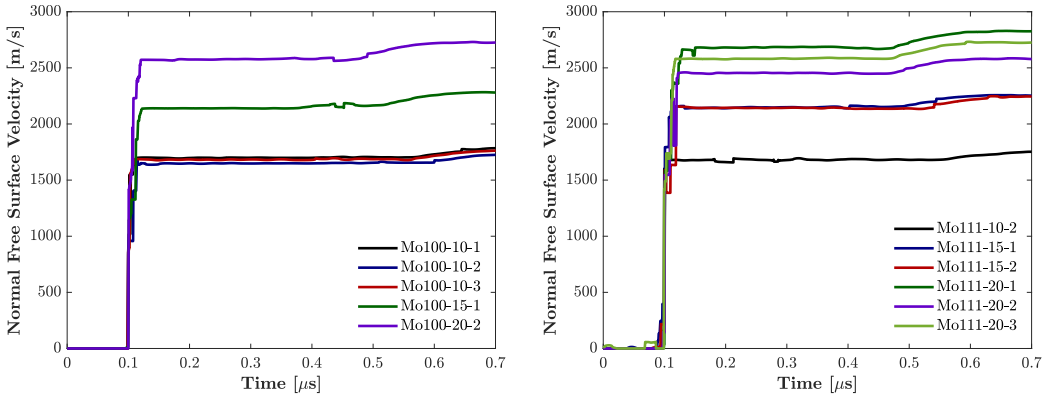

(a) (b)

Figure 3.14: Corrected particle velocity measurements conducted using photonic Doppler velocimetry (PDV) for molybdenum (Mo) along (a) [1 0 0] and (b) [1 1 1] orientations.

$$u(t) = \frac{u_a(t) + U_s(n_1 - n_0)}{n_1}. \tag{3.43}$$

Here, $u(t)$ corresponds to the corrected out-of-plane particle velocity of the sample, $u_a(t)$ is the apparent velocity or the velocity calculated assuming no window is present, U_s is the shock wave velocity in the window material obtained from the wave arrival at the polycarbonate free surface using raw frequency data, n_0 is the ambient index of refraction of polycarbonate, and n_1 is the index of refraction in the compressed region of the window. The index of refraction scales as a function of density, ρ, such that $n = a + b\rho$. From [7], we use $a = 0.9$ and $b = 0.5528$ which are fitted coefficients from calibration experiments. While these are purely continuum results, the more important information from these experiments is the x-ray data.

The representative diffraction spots for molybdenum shocked at $\sim$ 10 GPa and $\sim$ 20 GPa on are shown in Figure 3.15. During the shocked state, since the material undergoes compression, the crystallographic d-spacing tends to decrease resulting in the spots shifting to higher azimuthal angles based on Bragg's law. This is illustrated in the diffraction data in Figure 3.15b. The radial and azimuthal shift of the Laue spots contain information on the elastic lattice strains and rotations in the material. It can be shown that the ambient scattering vector $\boldsymbol{g}_{hkl}$ in the reciprocal space is related to the scattering vector of the deformed lattices, $\boldsymbol{g}^d_{hkl}$, through the deformation gradient ($\boldsymbol{F}$), $\boldsymbol{g}^d_{hkl} = \boldsymbol{F}^{-T}\boldsymbol{g}_{hkl}$ [38]. Since each experiment typically contains two to four

diffraction spots and plate impact experiments are conducted under uniaxial strain conditions, an infinitesimal strain ($\boldsymbol{\varepsilon}$) linearization ($\boldsymbol{F} = \boldsymbol{I} + \boldsymbol{\varepsilon}$) and plane strain assumption was employed to uniquely determine the elastic strain tensor.

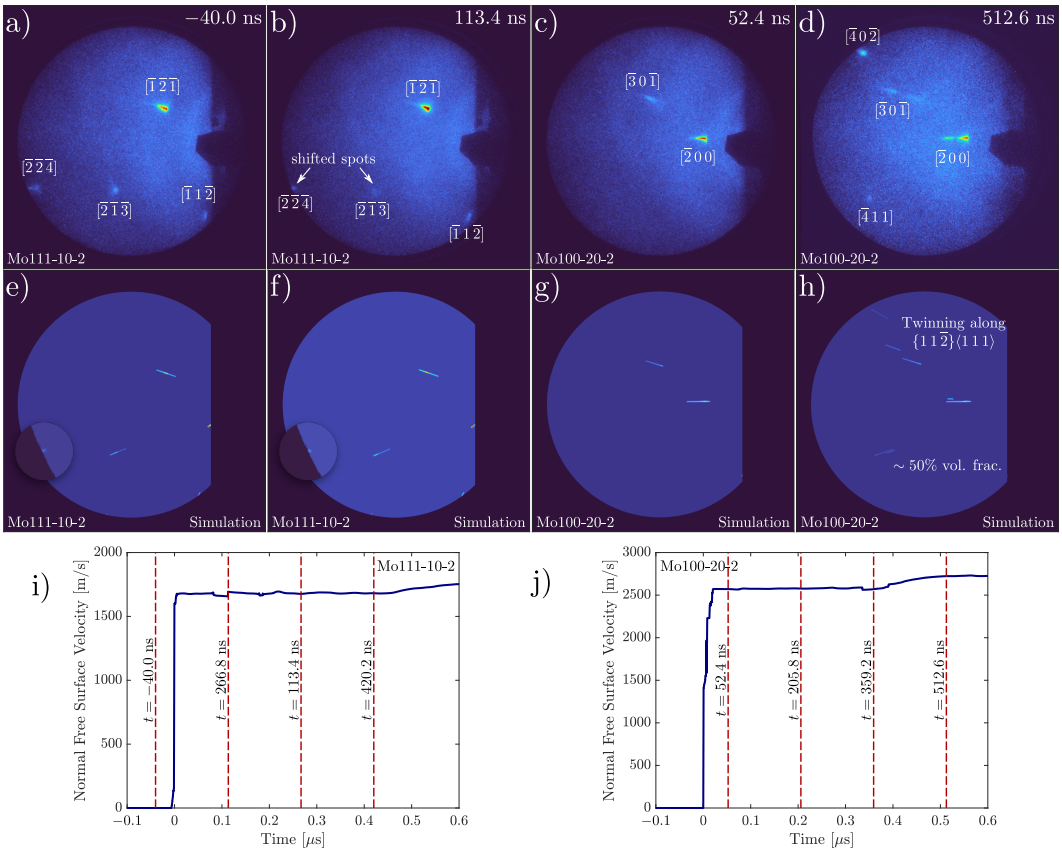

Figure 3.15: Summary of experimental results. (a)-(d) Experimentally obtained XRD frames which show both spots shifting due to compression and deformation twinning at higher pressure during the unloading. The diffraction spots are labeled using (e)-(h) for the respective XRD simulations incorporating both compression and twinning behavior. (i)-(j) The interferometry data is also shown indicating the time instances of XRD frame captures.

XRD simulations were conducted for all experiments from which we conclude that the shock compression behavior of molybdenum single crystals is governed by dislocation slip regardless of crystal orientation and impact stress. To further investigate this observation, the resolved shear stresses along the $\{1\,1\,0\}\langle 1\,1\,1\rangle$ and $\{1\,1\,2\}\langle 1\,1\,1\rangle$ slip systems were calculated and plotted in Figure 3.16. It is apparent that both these systems are active at the Hugoniot state for the two orientations where the $\{1\,1\,0\}\langle 1\,1\,1\rangle$ contributes to slip in the anti-twinning sense and $\{1\,1\,2\}\langle 1\,1\,1\rangle$ in the twinning. Additionally, the resolved

shear stress magnitude are similar for both orientations with the $\{1\,1\,\bar{2}\}\langle 1\,1\,1\rangle$ system being the most active. This explains the consistent peak Hugoniot velocity observed from the continuum measurements for both orientations for the same impact velocity and matches previous work by Oniyama et al. [33]. They reported the shock velocity-particle velocity ($U_s - u_p$) equation of state for the different molybdenum crystal orientations were very similar to within experimental uncertainty similar to previous literature on FCC metals such as copper [41] and aluminum [42]. This implies that while single crystals exhibit orientation dependence at the elastic limit, no anisotropy may be present for the Hugoniot response of cubic crystals.

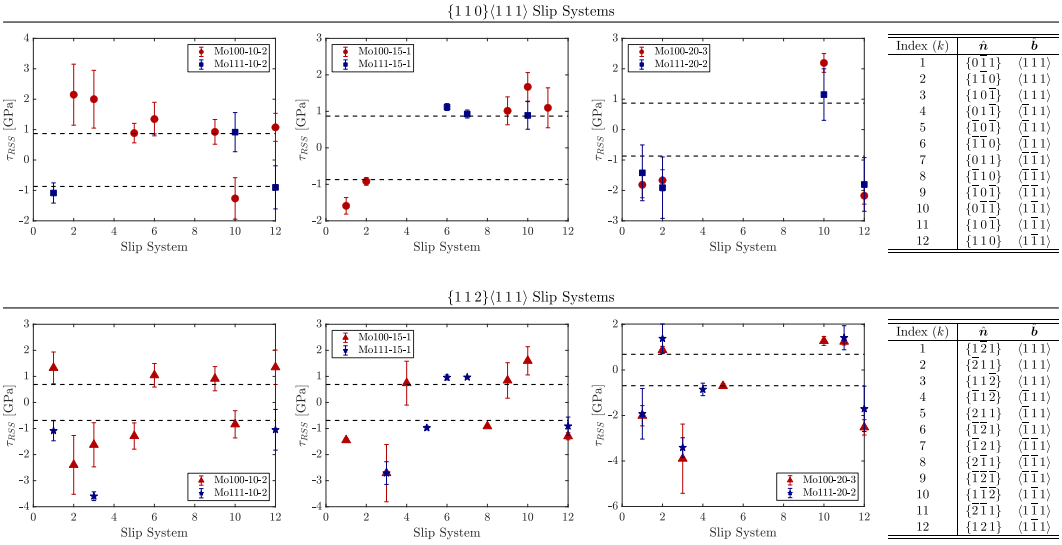

Index (k)	$\hat{n}$	$\hat{b}$
1	$\{0\,\bar{1}\,1\}$	$\langle 1\,1\,1\rangle$
2	$\{1\,\bar{1}\,0\}$	$\langle 1\,1\,1\rangle$
3	$\{1\,0\,\bar{1}\}$	$\langle 1\,1\,1\rangle$
4	$\{0\,1\,\bar{1}\}$	$\langle \bar{1}\,1\,1\rangle$
5	$\{\bar{1}\,0\,1\}$	$\langle \bar{1}\,1\,1\rangle$
6	$\{\bar{1}\,\bar{1}\,0\}$	$\langle \bar{1}\,1\,1\rangle$
7	$\{0\,1\,1\}$	$\langle \bar{1}\,\bar{1}\,1\rangle$
8	$\{\bar{1}\,1\,0\}$	$\langle \bar{1}\,\bar{1}\,1\rangle$
9	$\{\bar{1}\,0\,1\}$	$\langle \bar{1}\,\bar{1}\,1\rangle$
10	$\{0\,\bar{1}\,1\}$	$\langle 1\,\bar{1}\,1\rangle$
11	$\{1\,0\,\bar{1}\}$	$\langle 1\,\bar{1}\,1\rangle$
12	$\{1\,1\,0\}$	$\langle 1\,\bar{1}\,1\rangle$

Index (k)	$\hat{n}$	$\hat{b}$
1	$\{1\,2\,\bar{1}\}$	$\langle 1\,1\,1\rangle$
2	$\{\bar{2}\,1\,1\}$	$\langle 1\,1\,1\rangle$
3	$\{1\,1\,\bar{2}\}$	$\langle 1\,1\,1\rangle$
4	$\{\bar{1}\,1\,2\}$	$\langle \bar{1}\,1\,1\rangle$
5	$\{2\,1\,1\}$	$\langle \bar{1}\,1\,1\rangle$
6	$\{\bar{1}\,2\,1\}$	$\langle \bar{1}\,1\,1\rangle$
7	$\{\bar{1}\,2\,1\}$	$\langle \bar{1}\,\bar{1}\,1\rangle$
8	$\{2\,\bar{1}\,1\}$	$\langle \bar{1}\,\bar{1}\,1\rangle$
9	$\{\bar{1}\,\bar{2}\,1\}$	$\langle \bar{1}\,\bar{1}\,1\rangle$
10	$\{1\,\bar{1}\,2\}$	$\langle 1\,\bar{1}\,1\rangle$
11	$\{\bar{2}\,\bar{1}\,1\}$	$\langle 1\,\bar{1}\,1\rangle$
12	$\{1\,2\,1\}$	$\langle 1\,\bar{1}\,1\rangle$

Figure 3.16: Resolved shear stress (τ_{rss}) along the 12 different $\{1\,1\,0\}\langle 1\,1\,1\rangle$ and $\{1\,1\,2\}\langle 1\,1\,1\rangle$ slip systems of BCC single crystal for orientations, [1 0 0] and [1 1 1] molybdenum crystals at pressures ranging from $10 - 20$ GPa. Only the data above the critical resolved shear stresses (dashed lines) are shown.

While the experiments in this study probed the diffraction spot evolution at the Hugoniot state, using the resolved stresses in Figure 3.16, we anticipate the anisotropy at the elastic limit could stem from the larger number of slip systems activated for [1 0 0] orientation seen for the lowest stress experiment ($\sim$ 9 GPa) which are the closest to the elastic limit of the two orientations. An alternate possibility is related to the cubic symmetry of the stiffness tensor. For example, consider a uniaxial elastic strain of 1% for both the [1 0 0] and [1 1 1] single crystals. The maximum and minimum principal stress for the [1 0 0] is 466 MPa and 163 MPa, respectively, whereas for [1 1 1] it is 410 MPa and 191 MPa. This clearly implies that the shear stresses along the [1 0 0] orientation

will be larger due to the anisotropy in the stiffness tensor and thus, justifies the observed lower elastic limit than for the [1 1 1] orientation. Using this argument, the previous anisotropy in the elastic limit is justified as the lattice strains obtained for these experiments on [1 0 0] and [1 1 1] molybdenum were comparable at similar pressures. Thus, larger shear strains were present for the [1 0 0] crystals than the [1 1 1] and is illustrated in Figure 3.16.

At the highest pressures ($>$ 16 GPa), during unloading, new diffraction spots were observed along with preexisting spots splitting up. An example of this is shown in Figure 3.15d. This indicates that deformation twinning, which has been previously observed for shock compressed molybdenum [23, 24], governs the unloading behavior of Mo single crystals similar to what was observed for magnesium [43]. To determine the relevant twin systems, an additional contribution to the deformation gradient from twinning, $\boldsymbol{F}_t$, was incorporated in the simulations such that $\boldsymbol{F}_t = \boldsymbol{I} + \gamma \hat{\boldsymbol{b}} \otimes \hat{\boldsymbol{n}}$. Here, $\boldsymbol{I}$ is the identity tensor, $\gamma = \frac{1}{\sqrt{2}}$ is the twinning shear magnitude [39], and $\hat{\boldsymbol{n}}$ and $\hat{\boldsymbol{b}}$ are the twin plane normal and the twinning shear direction, respectively. The simulated diffraction with twinning is shown in Figure 3.15h. By iterating through all the possible $\{1\,1\,2\}\langle 1\,1\,1\rangle$ systems from Figure 3.16, it was determined that twinning in both [1 0 0] and [1 1 1] molybdenum always occurred along the $\{1\,1\,\bar{2}\}\langle 1\,1\,1\rangle$ system. This is consistent with the largest resolved shear stress observed along this system for all crystal orientations (Figure 3.16).

Multiple factors contribute to the nucleation and propagation of deformation twinning in BCC crystals such as pressure, strain rate, pre-straining, and grain size. Here, the Mo are single crystals and hence the grain size, d can be assumed to be infinite. Thus, by the Hall-Petch scaling relation $d^{-1/2}$ [14, 39, 44], larger grain sizes correspond to lower twinning shear stress. It was previously determined, using DFT calculations [45, 46], that a shear stress of 1.4 GPa is sufficient to nucleate twins. While the magnitude of resolved shear stress along the $\{1\,1\,\bar{2}\}\langle 1\,1\,1\rangle$ system is beyond this critical value during compression, here, twinning only occurs during shock release. During unloading, the macroscopic normal stress decreases faster than the lateral stresses which results in a reverse yielding. Additionally, during release, the shear stress along the $\{1\,1\,\bar{2}\}\langle 1\,1\,1\rangle$ system reverses in direction. Since twinning is polarized [39] unlike slip, the reversal in direction due to unloading is critical to induce the nucleation of twins.

The passage of the compressive shock wave contributes to pre-straining and produces homogeneous nucleation of dislocations [39, 44]. Earlier work on shock compressed molybdenum and post-mortem TEM analysis by Mahajan et al. [23] demonstrated that homogeneous dislocation field and pre-straining suppresses the formation of twins. However, during unloading, dislocation annihilation tends to occur [14, 44] potentially generating a heterogeneous distribution similar to what Mahajan et al. [23] observed in their shock recovered samples. With regards to pre-straining, Christian et al. [39] claim that the amount of pre-straining required to suppress twinning depends on the strain rate. Since the strain rates during release in our experiments are lower than during compression but still beyond 10^5 s^{-1}, this may be sufficient to reduce the effect of pre-compression due to the shock wave. Additionally, based on the experiments conducted here, both shock and release behavior of molybdenum at lower pressure is primarily governed by dislocation slip, however, the critical pressure describing the slip-to-twin transition [44] occurs around 16 GPa. This is much lower than the transition pressure for [0 0 1] copper [44] possibly due to the higher stacking fault energies in FCC metals. On the contrary, previous work by Wongwiwat et al. [24] and Mahajan et al. [23] observed twinning at lower pressures for polycrystalline Mo based on recovered samples possibly due to higher deviatoric stresses from grain boundary interactions. This is consistent with what is observed for iron single crystal where the critical stress to induce phase transformation was lower for polycrystalline iron due to generally higher deviatoric stresses present than [1 0 0] iron [47].

3.5 Conclusion

In summary, plate impact experiments with real-time x-ray diffraction were conducted for the first time to characterize the deformation mechanisms governing the elastic-plastic compression of molybdenum single crystals. We observe that the shock compression and release behavior is dominated by dislocation slip along $\{1\,1\,0\}\langle 1\,1\,1\rangle$ and $\{1\,1\,2\}\langle 1\,1\,1\rangle$ slip systems for both [1 0 0] and [1 1 1] crystal orientations. However, at normal stresses beyond 16 GPa, $\{1\,1\,\bar{2}\}\langle 1\,1\,1\rangle$ twins are nucleated during unloading. This explains why the loading orientation does not effect the Hugoniot response and the anisotropy only affects the elastic-plastic transition. Future works will aim to explore the shock-and-release behaviors at higher stress, at varying strain rates, and at

varying pulse duration to better characterize the mechanisms contributing to the onset of twinning and understand its role on material strength. Additionally, exploring the role grain boundaries on the elastic-to-plastic transition and the shock-release behavior would be an interesting next step.

References

[1] M. A. Meyers, *Dynamic behavior of materials* (John Wiley & Sons, 1994).

[2] R. F. Smith, D. E. Fratanduono, D. G. Braun, T. S. Duffy, J. K. Wicks, P. M. Celliers, S. J. Ali, A. Fernandez-Pañella, R. G. Kraus, D. C. Swift, and et al., "Equation of state of iron under core conditions of large rocky exoplanets," Nature Astronomy **2**, 452–458 (2018).

[3] M. Itoh, M. Katayama, and R. Rainsberger, "Computer simulation of a boeing 747 passenger jet crashing into a reinforced concrete wall," Materials Science Forum **465-466**, 73–78 (2004).

[4] G. A. Graham, A. T. Kearsley, I. P. Wright, M. J. Burchell, and E. A. Taylor, "Observations on hypervelocity impact damage sustained by multi-layered insulation foils exposed in low earth orbit and simulated in the laboratory," International Journal of Impact Engineering **29**, 307–316 (2003).

[5] D. Sandstrom, "Armor/Anti-Armor Materials by Design," Los Alamos Science Summer **17**, 36–50 (1989).

[6] Y. M. Gupta, S. J. Turneaure, K. Perkins, K. Zimmerman, N. Arganbright, G. Shen, and P. Chow, "Real-time, high-resolution x-ray diffraction measurements on shocked crystals at a synchrotron facility," Review of Scientific Instruments **83**, 123905 (2012).

[7] J. A. Hawreliak and S. J. Turneaure, "Probing the lattice structure of dynamically compressed and released single crystal iron through the alpha to epsilon phase transition," Journal of Applied Physics **129**, 135901 (2021).

[8] S. J. Tracy, S. J. Turneaure, and T. S. Duffy, "In situ x-ray diffraction of shock-compressed fused silica," Physical Review Letters **120**, 135702 (2018).

[9] S. J. Turneaure, S. M. Sharma, and Y. M. Gupta, "Crystal structure and melting of Fe shock compressed to 273 gpa: In situ x-ray diffraction," Physical Review Letters **125**, 215702 (2020).

[10] P. Renganathan, S. J. Turneaure, S. M. Sharma, and Y. M. Gupta, "Structural transformations including melting and recrystallization dur-

ing shock compression and release of germanium up to 45 gpa," Physical Review B **99**, 134101 (2019).

[11] S. J. Turneaure, S. M. Sharma, and Y. M. Gupta, "Nanosecond melting and recrystallization in shock-compressed silicon," Physical Review Letters **121**, 135701 (2018).

[12] J. Wadsworth, T. G. Nieh, and J. J. Stephens, "Recent advances in aerospace refractory metal alloys," International Materials Reviews **33**, 131–150 (1988).

[13] C. R. Weinberger, B. L. Boyce, and C. C. Battaile, "Slip planes in bcc transition metals," International Materials Reviews **58**, 296–314 (2013).

[14] M. Sliwa, D. McGonegle, C. Wehrenberg, C. A. Bolme, P. G. Heighway, A. Higginbotham, A. Lazicki, H. J. Lee, B. Nagler, H. S. Park, R. E. Rudd, M. J. Suggit, D. Swift, F. Tavella, L. Zepeda-Ruiz, B. A. Remington, and J. S. Wark, "Femtosecond x-ray diffraction studies of the reversal of the microstructural effects of plastic deformation during shock release of tantalum," Physical Review Letters **120**, 265502 (2018).

[15] L. Hollang, D. Brunner, and A. Seeger, "Work hardening and flow stress of ultrapure molybdenum single crystals," Materials Science and Engineering: A **319-321**, 233–236 (2001).

[16] S. S. Lau and J. E. Dorn, "Asymmetric slip in mo single crystals," Physica Status Solidi (a) **2**, 825–836 (1970).

[17] S. Lau, S. Ranji, A. Mukherjee, G. Thomas, and J. Dorn, "Dislocation mechanisms in single crystals of tantalum and molybdenum at low temperatures," Acta Metallurgica **15**, 237–244 (1967).

[18] J. Y. Kim and J. R. Greer, "Tensile and compressive behavior of gold and molybdenum single crystals at the nano-scale," Acta Materialia **57**, 5245–5253 (2009).

[19] A. Seeger, "The flow stress of high-purity refractory body-centred cubic metals and its modification by atomic defects," Le Journal de Physique IV **05**, 10.1051/jp4:1995704 (1995).

[20] A. Seeger, "Why anomalous slip in body-centred cubic metals?" Materials Science and Engineering: A **319-321**, 254–260 (2001).

[21] G. J. Irwin, F. Guiu, and P. L. Pratt, "The influence of orientation on slip and strain hardening of molybdenum single crystals," Physica Status Solidi (a) **22**, 685–698 (1974).

[22] A. Seeger and L. Hollang, "The flow-stress asymmetry of ultra-pure molybdenum single crystals," Materials Transactions, JIM **41**, 141–151 (2000).

[23] S. Mahajan and A. Bartlett, "Influence of prior mechanical and thermal treatments on shock-induced substructures in molybdenum," Acta Metallurgica **19**, 1111–1119 (1971).

[24] K. Wongwiwat and L. Murr, "Effect of shock pressure, pulse duration, and grain size on shock-deformation twinning in molybdenum," Materials Science and Engineering **35**, 273–285 (1978).

[25] D. Santamaría-Pérez, M. Ross, D. Errandonea, G. D. Mukherjee, M. Mezouar, and R. Boehler, "X-ray diffraction measurements of mo melting to 119 gpa and the high pressure phase diagram," Journal of Chemical Physics **130**, 124509 (2009).

[26] R. S. Hixson and J. N. Fritz, "Shock compression of tungsten and molybdenum," Journal of Applied Physics **71**, 1721–1728 (1992).

[27] J. H. Nguyen, M. C. Akin, R. Chau, D. E. Fratanduono, W. P. Ambrose, O. V. Fat'yanov, P. D. Asimow, and N. C. Holmes, "Molybdenum sound velocity and shear modulus softening under shock compression," Physical Review B **89**, 174109 (2014).

[28] J. Wang, F. Coppari, R. F. Smith, J. H. Eggert, A. E. Lazicki, D. E. Fratanduono, J. R. Rygg, T. R. Boehly, G. W. Collins, and T. S. Duffy, "X-ray diffraction of molybdenum under ramp compression to 1 tpa," Physical Review B **94**, 104102 (2016).

[29] G. I. Kanel, S. V. Razorenov, A. V. Utkin, V. E. Fortov, K. Baumung, H. U. Karow, D. Rusch, and V. Licht, "Spall strength of molybdenum single crystals," Journal of Applied Physics **74**, 7162–7165 (1993).

[30] A. Mandal and Y. M. Gupta, "Elastic-plastic deformation of molybdenum single crystals shocked along [100]," Journal of Applied Physics **121**, 045903 (2017).

[31] A. Mandal and Y. M. Gupta, "Elastic-plastic deformation of molybdenum single crystals shocked to 12.5 GPa: Crystal anisotropy effects," Journal of Applied Physics **125**, 055903 (2019).

[32] T. Oniyama, Y. M. Gupta, and G. Ravichandran, "Shock compression of molybdenum single crystals to 110 GPa: elastic–plastic deformation and crystal anisotropy," Journal of Applied Physics **127**, 205902 (2020).

[33] T. Oniyama, Y. M. Gupta, and G. Ravichandran, "Peak states of molybdenum single crystals shock compressed to high stresses," Journal of Applied Physics **129**, 245906 (2021).

[34] C. Prescher and V. B. Prakapenka, "Dioptas: a program for reduction of two-dimensional x-ray diffraction data and data exploration," High Pressure Research **35**, 223–230 (2015).

[35] O. T. Strand, D. R. Goosman, C. Martinez, T. L. Whitworth, and W. W. Kuhlow, "Compact system for high-speed velocimetry using heterodyne techniques," Review of Scientific Instruments **77**, 083108 (2006).

[36] *MATLAB version 9.11.0.1769968 (R2021b)* (The Mathworks, Inc., Natick, Massachusetts, 2021).

[37] B. Fultz and J. Howe, *Transmission electron microscopy and diffractometry of materials* (Springer, 2013).

[38] M. Miller, *Polycrystalline Diffraction–A Primer for the 2016 APS NX School*, 2017.

[39] J. Christian and S. Mahajan, "Deformation twinning," Progress in Materials Science **39**, 1–157 (1995).

[40] L. M. Barker and R. E. Hollenbach, "Shock-wave studies of pmma, fused silica, and sapphire," Journal of Applied Physics **41**, 4208–4226 (1970).

[41] R. Chau, J. Stölken, P. Asoka-Kumar, M. Kumar, and N. C. Holmes, "Shock hugoniot of single crystal copper," Journal of Applied Physics **107**, 023506 (2010).

[42] D. Choudhuri and Y. M. Gupta, "Shock compression of aluminum single crystals to 70 gpa: role of crystalline anisotropy," Journal of Applied Physics **114**, 153504 (2013).

[43] S. J. Turneaure, P. Renganathan, J. M. Winey, and Y. M. Gupta, "Twinning and dislocation evolution during shock compression and release of single crystals: real-time x-ray diffraction," Physical Review Letters **120**, 265503 (2018).

[44] M. Meyers, H. Jarmakani, E. Bringa, and B. Remington, *Dislocations in shock compression and release*, edited by J. Hirth and L. Kubin, Vol. 15, Dislocations in Solids (2009), pp. 91–197.

[45] S. Ogata, J. Li, and S. Yip, "Twinning pathway in bcc molybdenum," Europhysics Letters **68**, 405 (2004).

[46] S. Ogata, J. Li, and S. Yip, "Energy landscape of deformation twinning in bcc and fcc metals," Physical Review B **71**, 224102 (2005).

[47] B. J. Jensen, G. T. Gray, and R. S. Hixson, "Direct measurements of the α-ϵ transition stress and kinetics for shocked iron," Journal of Applied Physics **105**, 103502 (2009).

Chapter 4

CONCLUSIONS

4.1 Summary

In this thesis, the governing deformation mechanisms, such as elastic-plastic transition under uniaxial strain conditions and the role of phase transformation on dynamic strength, in shock compressed body-centered cubic crystals is investigated. Iron and molybdenum are chosen as representative BCC metals to study these phenomena due to the well known phase transformation of iron at 13 GPa of pressure and availability of molybdenum single crystals in high purity form to study key mechanisms governing plasticity.

In Chapter 2, the role of phase transformation on the evolution of the yield strength of iron at pressures ranging from 10-42 GPa is explored. This is done using high pressure-pressure shear plate impact experiments where a thin iron sample is sandwiched between two tungsten carbide anvils to decouple the role of compression and shear. Using the measured normal and transverse free surface velocity coupled with finite element simulations, the shear strength of iron in its α- and ϵ-phase was obtained as a function of strain, pressure, and temperature. It was observed the strength of iron in its phase transformed state, 2.53 GPa, was more than twice that of the material in its ambient phase, 1.04 GPa, potentially due to the microstructure evolution during phase transition and the dynamic Hall-Petch effect. Lastly, it was shown that the current strength model for ϵ-iron significantly under-predicted previous dynamic strength models which postulate material strength to the cusp of theoretical limits.

Finally, in Chapter 3, the elastic-to-plastic transition and the Hugoniot behavior of BCC metals, specifically molybdenum, on an atomic scale using real-time Laue x-ray diffraction, is investigated. Molybdenum single crystals oriented along the $[1\,0\,0]$ and $[1\,1\,1]$ directions are impacted onto a polycarbonate window at velocities ranging from 1800 to 2800 m/s corresponding to pressures of $9-19$ GPa. While the elastic limits are affected by the crystal orientation, the Hugoniot steady state behavior is independent of the crystal axis as dislocation slip along $\{1\,1\,0\}\langle 1\,1\,1\rangle$ and $\{1\,1\,2\}\langle 1\,1\,1\rangle$ systems governs shock compression

for all single crystals. Interestingly, deformation twinning is observed for both [1 0 0] and [1 1 1] molybdenum upon shock release beyond a critical Hugoniot stress of 16 GPa possibly due to reversal of shearing direction and dislocation structure evolution. However, it is still unknown what the exact reasons for why twinning only occurs during release and what governs the critical stress.

Based on the investigations undertaken in this thesis, it becomes apparent there are mechanics and physics still unexplored regarding the deformation behavior and phase transformation of BCC crystals. These are outlined in the next section.

4.2 Future work

4.2.1 Pressure Dependent Shear Modulus of Iron

It was previously shown that pressure effects on yield strength are more significant than strain-rate dependence under these condensed matter states [1]. However, it is generally difficult to characterize the pressure dependence on yield strength as inelasticity is associated with deviatoric components of stress. However, elastic wave speeds and thus elastic constants, such as shear modulus, have an inherent pressure dependence which indirectly relate the pressure and yield strength. PSPI experiments shown in Chapter 2 on phase transformed ϵ-iron have shown a significant strength increase compared to its ambient α-phase with a change in the pressure dependent yield strength scaling as a possible key mechanism. To further explore this topic, pressure shear plate impact experiments with window interferometry can be conducted to probe the pressure-dependent longitudinal and shear wave speeds of iron upon phase transformation.

Essentially, a symmetric iron impact with a c-cut sapphire window can be conducted at a low skew angle of approximately 3°. The impedance match with iron, and its low index of refraction sensitivity to density makes c-cut sapphire an ideal optical window. A diffraction grating would be sandwiched between the iron sample and a c-cut sapphire window which enables measurement of in-material normal and transverse particle velocities. The shear wave arrival time at the sample-window interface can be used to extract the shear modulus data at constant pressure. Simultaneously, the arrival time of the normal release wave from the impact surface provides information on the longitudinal

moduli at constant pressure.

Here, the diffraction grating is the most critical element, however, also the most challenging to implement as it is no longer at the free surface and must now withstand the large stresses from the shock wave. Thus, to mitigate damage during the experiment, a metallic grating must be used due to its high strength and stiffness compared to conventional polymer gratings. This introduces additional challenges in manufacturing, i.e., additional steps such as lift-off process using electron-beam lithography and increased attention to detail. Finally, to further protect the grating, specifically during the sandwich process, an Al_2O_3 layer must be deposited which acts as a buffer for the sapphire (Al_2O_3) window.

These experiments provide information on pressure dependent elastic constants and on the forward-reverse transformation under multi-axial states, due to shear, via wave speeds. Ultimately, these data can be used to develop a more robust strength model close to the transition pressure instead of extrapolating parameters from quasi-static experiments conducted at pressures an order of magnitude higher. In addition, these data can aid in developing a more robust EOS and kinetics based phase transformation model.

4.2.2 Shear-Induced Phase Transformation

The role of deviatoric stresses on the solid-solid phase transformations of quasi-static and shock compressed metals has been an unanswered question that has received significant attention in recent years [2–5]. While this provides a fundamental understanding of the phase stability, hysteresis loop, phase transition kinetics, and expands the $P-T$ space into a third shear stress (τ) axis, there have been no experimental quantification on the role of shear on phase transformation. However, this serves as a natural extension to work presented in both Chapter 2 and 3. For example, the questions regarding whether the ϵ-phase can be initiated at a pressure lower than 13 GPa or whether the reverse transition can be delayed are important to understand the high strength and stiffness of this phase. This can be achieved by extending the pressure shear plate impact (PSPI) experiments to thin samples (~ 5 μm) achieved via sputtering or electron beam deposition, and higher inclination angles ($18^\circ - 25^\circ$) using elastic anvils such as sapphire. Experiments would be conducted at impact stresses ranging from 9-12 GPa, which are close to the

initiation pressure, and the evolution of transverse velocity measured (thus shear stress vs. strain curve) at the anvil free surface can be used to predict the phase transition. This requires the anvils to remain elastic such that the shear wave dissipation only occurs while it traverses the sample and the elastic governing equations (Eqs. (1.9)) can be used to accurately determine the shear stress as a function of time.

Using the above methodology, the phase transition is assumed from continuum measurements but a more discrete method would require extending the work in Chapter 3 using dynamic XRD. At The Dynamic Compression Sector at APS, only normal plate impact experiments can be conducted, however, one can use anisotropic crystals to generate a quasi-shear shear wave onto the sample of interest. For example, a polycrystalline iron can be sandwiched between a y-cut quartz front anvil and a c-cut sapphire rear anvil at DCS and transmission geometry would have to be employed to reduce the x-ray attenuation through the quartz and sapphire. Since iron is polycrystalline, the formation and annihilation of diffraction rings at impact stresses ranging from $10 - 20$ GPa can be used to determine the initiation, stability, volume fraction, and evolution of the phase transformation.

These experiments can significantly extend our understanding of the kinetics, strain rate dependence on strength, and the effect of phase transition on strength for more accurate material models involving these phase transformation phenomena.

4.2.3 Shock Recovery Experiments

As shown in Chapter 3, BCC metals may undergo deformation twinning upon release thus altering the microstructure and possibly material properties. Additionally, in Chapter 2, it the iron material at 15 GPa was inferred to be approximately 78% ϵ-phase using models derived from normal impact experiments which could differ since the state of stress was not uniaxial in our experiments. The questions of interest then are, why the molybdenum twins only during shock release and how this formation of twinning alters the mechanical properties of the shocked BCC crystal. Alternatively, the volume fraction of twinning observed for shock recovered iron samples can be used to approximate the volume fraction of phase transformation in the material under these multiaxial stress states. To understand the kinetics for twinning in Mo and the

evolution of the ϵ-phase in iron as a function of pressure, post-moretem analysis is required. This can be done by using a more non-destructive momentum trap to preserve and recover the samples for post-mortem analysis using electron microscopy and mechanical characterization such as nano-indentation. Transition electron microscopy (TEM) can also be used to determine dislocation densities of these shock recovered materials to possibly explain the observed hardening and yield behavior during shock compression and release.

4.2.4 Dynamic strength during shock and release

The focus of experiments conducted in Chapter 3 was to resolve the orientation dependence on elastic-plastic transition in the material and the key microscopic governing mechanisms. While the elastic limit was sensitive to loading orientation, both the Hugoniot steady state and the initial release were independent. To better understand whether the peak state of Mo single crystals are isotropic, sandwich configuration pressure shear plate impact (PSPI) experiments can be conducted at various Mo orientations ([1 0 0], [1 1 0], and [1 1 1]) where the material is first compressed to pressures ranging from $10-42$ GPa and then sheared to probe its strength. The effect of crystal orientation on strength may help shed light on the orientation-independent steady-state response of these material as their deviatoric stresses may differ.

Additionally, based on the XRD frames in Chapter 3, twinning along the same system and of the same volume fraction was observed immediately upon release after a critical pressure irrespective of the crystal orientation. The role of twinning on crystal orientation and material strength can be probed by conducting shock-release PSPI experiments using a layered impactor at pressures above and below the critical value for twinning. Using this method, one can release the pressure in the sample during the shear window potentially initiating twinning while probing the strength to understand the role of microstructural changes on strength.

References

[1] M. B. Prime, W. T. Buttler, S. J. Fensin, D. R. Jones, J. L. Brown, R. S. King, R. Manzanares, D. T. Martinez, J. I. Martinez, J. R. Payton, and D. W. Schmidt, "Tantalum strength at extreme strain rates from impact-

driven Richtmyer-Meshkov instabilities," Physical Review E **100**, 053002 (2019).

[2] N. V. Barge and R. Boehler, "Effect of non-hydrostaticity on the $\alpha - \epsilon$ transition of iron," High Pressure Research **6**, 133–140 (1990).

[3] K. J. Caspersen, A. Lew, M. Ortiz, and E. A. Carter, "Importance of shear in the bcc-to-hcp transformation in iron," Physical Review Letters **93**, 115501 (2004).

[4] A. Lew, K. Caspersen, E. Carter, and M. Ortiz, "Quantum mechanics based multiscale modeling of stress-induced phase transformations in iron," Journal of the Mechanics and Physics of Solids **54**, 1276–1303 (2006).

[5] A. Sadjadpour, D. Rittel, G. Ravichandran, and K. Bhattacharya, "A model coupling plasticity and phase transformation with application to dynamic shear deformation of iron," Mechanics of Materials **80**, 255–263 (2015).